MODELING AND CONTROL APPROACHES FOR MULTI-OUTPUT SWITCHED CONVERTERS

by

Carlos Andres Bruzos

BACHELOR OF SCIENCE IN ELECTRICAL ENGINEERING
TULANE UNIVERSITY, NEW ORLEANS
(1987)

Submitted to the Department of Electrical Engineering and Computer Science
in Partial Fulfillment of the Requirements for the Degree of

MASTER OF SCIENCE IN ELECTRICAL ENGINEERING

at the

MASSACHUSETTS INSTITUTE OF TECHNOLOGY

May, 1989

Signature of Author ____
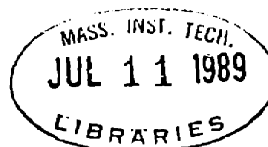
Department of Electrical Engineering and Computer Science
May 11, 1989

Certified by _____

George C. Verghese
Thesis Supervisor

Accepted by _____

Arthur C. Smith
Chairman, Departmental Committee on Graduate Students

Modeling and Control for
Multi-Output Switched Converters

by

Carlos Andres Bruzos

Submitted to the Department of Electrical Engineering and Computer Science on May 9, 1989 in partial fulfillment of the requirements for the degree of Master of Science in Electrical Engineering.

Abstract

This thesis investigates issues concerning modeling and feedback control design for switching power converters. A correction to the usual derivation of state-space averaged models for constant frequency, current mode controllers is given and new results are shown and compared with existent results. Approximate sampled-data models, often written down but seldom exploited, are also highlighted. A two-output two-switch half-bridge converter is presented and modeled. Averaged and sampled-data models are given. It is shown that the multivariable models of the half-bridge converter can be decoupled into two single-input single-output switching converters. The stability robustness of the closed-loop half-bridge converter is examined, and guaranteed stability tests are obtained for the decoupled model.

The Linear Quadratic Regulator state feedback design method is presented and systematically applied via $MATRIX_x$ to each output system of the decoupled half-bridge converter model. The regulation of the full closed-loop half-bridge converter is evaluated through simulations of performance tests and is found to meet stringent closed-loop power supply specifications. Assuming the converter inductor currents are difficult to measure, observer based compensator designs are obtained and analyzed in the same manner. Observer based feedback designs are found to yield equally satisfactory results. A simple hardware implementation for these observer based compensators is suggested. Recommendations for further work are stated.

Thesis Supervisor: Dr. George C. Verghese
          Title: Associate Professor of Electrical Engineering

Acknowledgements

A los mejores padres del mundo, Isabel Alvarado y Pedro Palos.

Contents

List of Figures

9

List of Tables

Chapter 1

Introduction

This thesis deals with modeling and control issues for single and multi-output, multi switch DC-to-DC power converters (regulators). Switching regulation is the technique by which unregulated source power is efficiently converted to regulated load power through the use of controlled power switching devices. The emphasis upon switching techniques, as opposed to linear techniques, relates to efficiency. An ideal switch has no losses because either the voltage or current is zero. Thus, since it is designed to achieve high efficiency energy conversion, a switching power converter is essentially composed of switches and energy storage elements. The nominal steady state operation of a DC-DC converter involves a cyclic operation of the switches to produce a commanded average output voltage or current from a specified DC input source.

The modeling and control of switching power converters is an interesting and challenging research topic for various reasons. Most importantly, DC-DC converters are generally highly nonlinear systems with time-varying topologies. The flow of electrical energy from the source to the load(s) is controlled by turning the converter power switches on and off. Therefore, it is necessary to develop modeling techniques that would simplify the system analysis and control design, but at the same time be robust to modeling errors, at least in the frequency range of interest. Also, being power supplies, DC converters must generally satisfy stringent closed loop design specifica-

tions with respect to output voltage stability, regulation and dynamic performance, hence making the control design a challenge. In addition, the presence of two or more controllable switches clearly makes the feedback control design a multivariable problem.

1.1   Outline and Contributions of Thesis

This thesis document is organized into two main parts. Part I deals with modeling issues for both single and multiple output switching converters, and is divided into two chapters (Chapters 2 and 3). Part II emphasizes control approaches for multiple output switching converters and includes Chapters 4 through 6. A tutorial on a modern systematic approach to control design is presented and applied to a typical half-bridge two-switch two-output converter.

The control system software package *MATRIXX* was used throught the thesis in the analysis and simulation of the switching power circuits presented.

Chapter 2 presents the three basic single output voltage converter circuits: the buck, boost, and buck-boost (up-down) converters. The up-down converter is particularly chosen to illustrate most of the arguments presented, since it exemplarizes many of the nonlinearities and difficulties that could be encountered in analyzing such systems. Typically used modeling approaches for DC power converters, namely averaged and sampled-data modeling, are presented and their trade-offs examined. Approximate sampled-data models, often written down but seldom exploited, are also investigated. The chapter also introduces a commonly used state feedback control method for these converters known as current mode control. The purpose of this is to present a correction to the state-space averaged models for constant frequency, current mode controlled converters usually found in the literature. This correction results in new small signal averaged models for current mode control, though several of the observations can be extended to converters operating under other control laws.

Chapter 3 analyzes issues regarding the modeling of multiple-switch multiple-output voltage converters. In particular, a two-switch two-output half-bridge converter is presented and analyzed. Mathematical models (switched, large and small signal averaged, large and small signal sampled-data) and simulations are shown for the half-bridge converter. Guidelines for small signal analysis of multi-switch multi-output switching converters in both the time and frequency domain are given, with results for the half-bridge converter. The chapter concludes with the examination of stability robustness of the closed-loop half-bridge converter.

Chapter 4 focuses on control design for high frequency switching converters. The Linear Quadratic Regulator (LQR) control design method for general multivariable (and, in particular, single-input single output) dynamic systems is presented and its closed loop properties discussed. An assumption of this design methodology is that all state variables are available for feedback. However, as can be the case in switching power converters, the cost/unavailability of sensing some of the state variables might introduce the need of state estimators or observers in the feedback control loop. This chapter also introduces observer theory and design and gives guidelines for the design of observers/observer-based-compensators for switching converters.

Chapter 5 presents the results of the application of the Linear Quadratic Regulator control design method to the two-output two-switch half-bridge converter. Control design is based on two single-input single-output systems which represent the half bridge converter after an input transformation that effectively decouples the system, as shown in [5] for a two-switch two-output forward converter. Closed-loop performance tests carried out on the System Build utility of *MATRIXX* are summarized. They correspond to tests typically used on the actual closed-loop circuits. The transients that result are presented and the LQR controllers evaluated.

Chapter 6 presents and evaluates observer based compensator designs for the half bridge converter. A reduced order observer design is presented and results/trade-offs

are compared with the full state feedback (LQR) controllers of Chapter 5.

Chapter 7 draws the pertinent conclusions of this research and identifies problems for future research. $MATRIX_x$ software and documentation for this thesis research is presented in [22].

In summary, the main contributions of this thesis are:

1. A correction to the usual derivation of state-space averaged models for constant frequency, current mode controlled converters.

2. Investigation of approximate sampled-data models for modeling switching power converters.

3. Guidelines for the small signal time and frequency domain analysis of multivariable switching power supplies.

4. Treatment of the issues concerning systematic control design and performance analysis of multiple-switch multiple-output switching converters.

Part I

Modeling

Chapter 2

Modeling DC To DC Switching Converters

This chapter presents issues concerning the operation and modeling of switching power converters. A commonly used control method known as current mode control will also be introduced and new results for current mode controlled converters will be presented. Approximate sampled-data models for these systems will be studied.

2.1 Basic Voltage Converters

The purpose of power converter systems is to efficiently supply an output load with a required average voltage from a dc input voltage source. Switching is used in order to achieve efficiency or lossless conversion. Figure 2.1 shows the three basic single output voltage converter circuit topologies. The goal is to switch S1 (NPN transistor) at a fixed frequency f_c and control its 'on' time during each switching period T, so that the desired average output voltage is obtained. Figure 2.2 shows the timing diagram for S1. The term d_k is the duty ratio in the $k - th$ cycle of operation and represents the fraction of the switching period that the transistor is 'on' or conducting, $0 < d_k < 1$. Constant duty ratio results in cyclic steady state operation.

The diode (S2) is introduced to provide a continuous inductor current path when

S1 is 'off'. Note that the power conversion stage only includes ideally lossless elements.

In this work, the circuits are assumed to be operated in such a way that either the transistor or the diode is always conducting (continuous conduction); the inductor current is not allowed to fall to zero. Under this assumption, the system can be characterized by two linear, time invariant (LTI) models corresponding to circuit configurations when the transistor is on ($u=1$) and when it is off ($u=0$). These two LTI models can be combined into a single large-signal model of the form

$$x'(t) = [A_0 + u(A_1 - A_0)]x(t) + [B_0 + u(B_1 - B_0)]V_{in} \qquad (2.1)$$

where A_1, A_0 and B_1, B_0 are the system state and input matrices when the transistor is 'on' or 'off', respectively. The state vector $x(t)$ is normally composed of inductor currents and capacitor voltages. Note that if u is considered an input in (2.1) the resulting description of the system is not only time-varying but nonlinear as well.

In the case of the buck-boost converter of Fig. 2.1, the transistor is turned on in the first part of the cycle, causing the inductor current to ramp up. During this time, the diode is reversed biased so that the capacitor voltage decays into the load. Then, in the second part of the cycle, the transistor is turned off and the diode becomes forward biased so that the inductor current flows through the diode, into the capacitor and the load. Noting that the average voltage across the inductor is zero in steady state, and assuming small ripple,

$$(d)V_{in} + (1 - d)v_{avg} \approx 0 \qquad (2.2)$$

where v_{avg} is the average steady state value of capacitor voltage and d is the nominal or steady state duty ratio or fraction of each cycle that the transistor is on. From (2.2), we obtain

$$v_{avg} = -\frac{d}{1 - d}V_{in} \qquad (2.3)$$

17
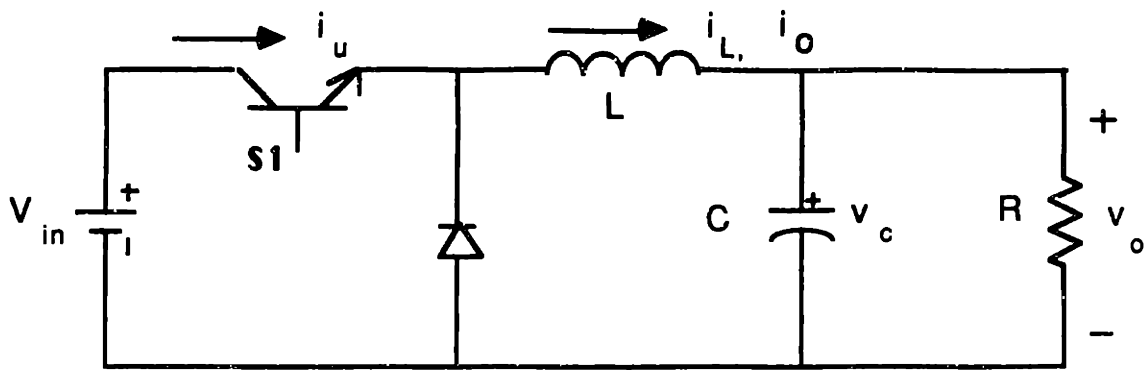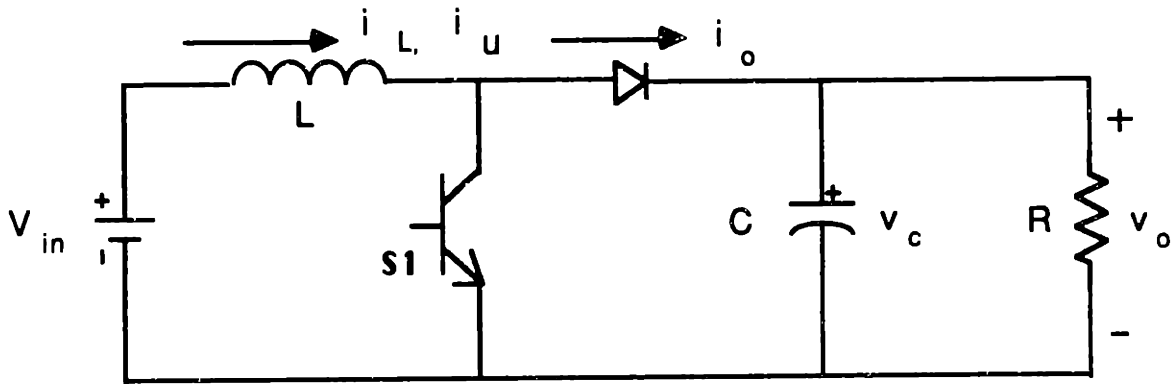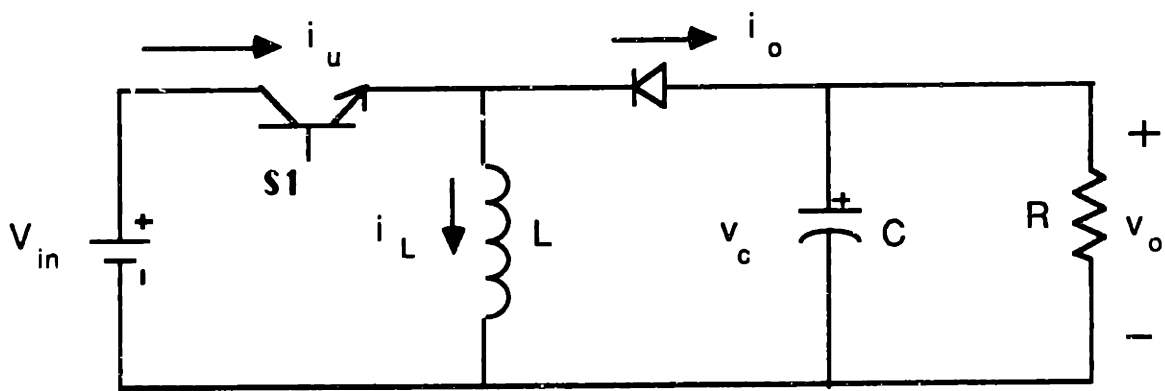
(a) buck

(b) boost

(c) buck-boost

Figure 2.1: The three basic voltage converter circuits. (a) Buck, (b) boost, and (c) buck-boost (up-down).
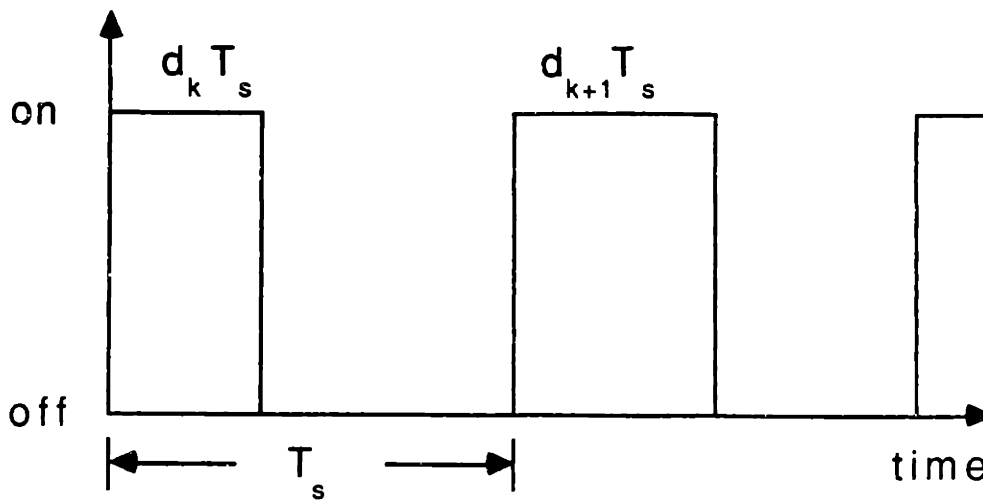
Figure 2.2: Switch S1 timing diagram

We see that the average value of the capacitor voltage in the steady state can be made either larger or smaller in magnitude than the source voltage V_{in} (this is why the circuit is termed a *buck-boost* or *up-down* converter).

Choosing the inductor current and capacitor voltage as state variables ($x(t) = (i_L(t)\ v_c(t))^T$) and making the appropiate substitutions into (2.1), the result for the buck-boost converter is

$$x'(t) = \begin{pmatrix} 0 & \frac{1-u}{L} \\ -\frac{1-u}{C} & -\frac{1}{RC} \end{pmatrix} x(t) + \begin{pmatrix} \frac{u}{L} \\ 0 \end{pmatrix} V_{in} \qquad (2.4)$$

where u takes on the values 0 and 1. Typical inductor current and capacitor voltage waveforms for the buck-boost converter are shown in Fig. 2.3. These nonlinear simulations were performed on $MATRIX_x$ as shown in [5]. The buck-boost parameter values used in these and subsequent simulations and comparisons are:

$$
\begin{array}{rcl}
V_{in} & = & 200V \\
L & = & 1.25mH \\
C & = & 100\mu F \\
R & = & 10\Omega \\
T & = & 50\mu sec \\
D & = & 0.4
\end{array}
$$

where D is the nominal duty ratio.

Time in seconds

Time in seconds
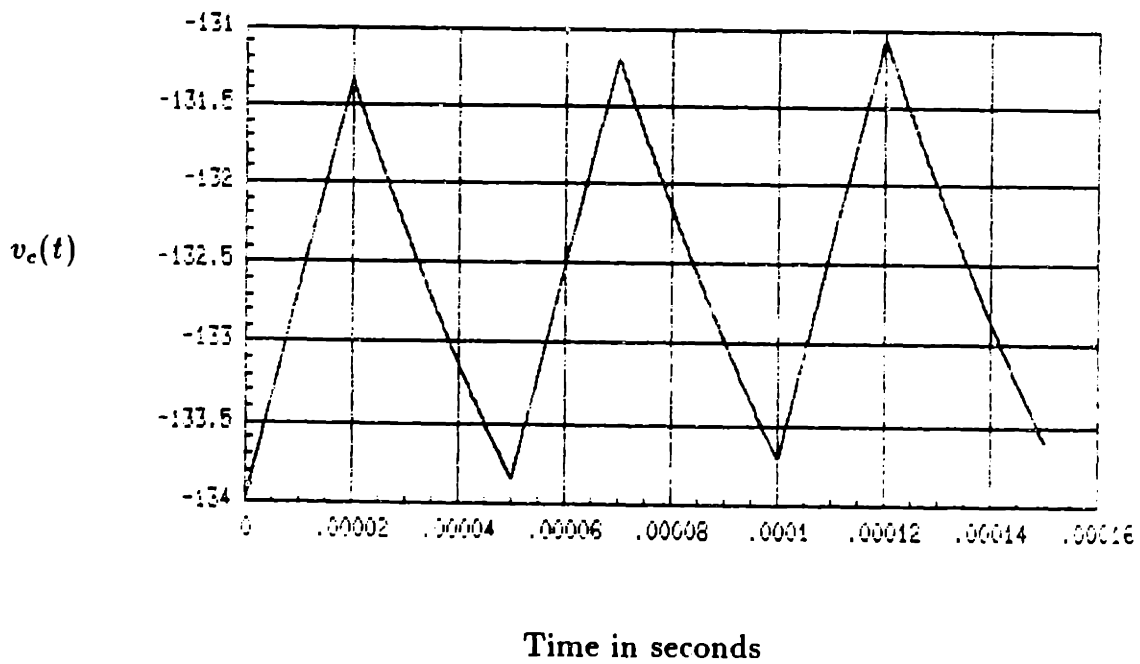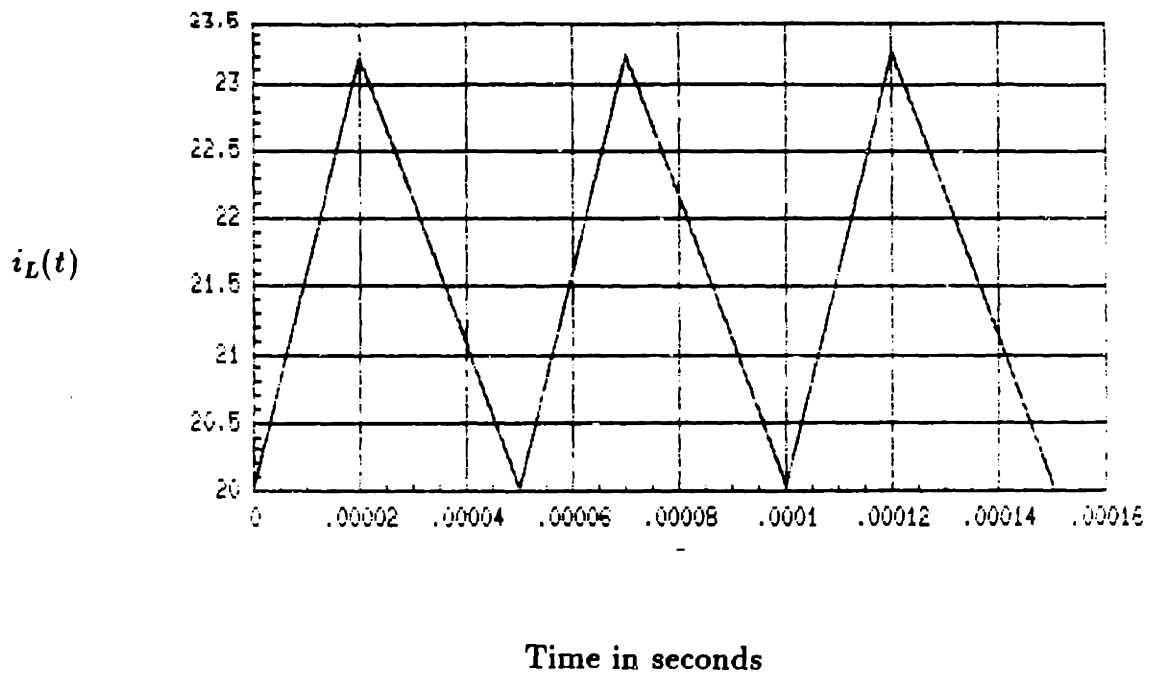
Figure 2.3: Typical buck-boost converter waveforms.

2.1.1 State space averaging

To facilitate the use of well established control design methods based on state-space models that have a continuously variable input, *state-space averaged* models for switching converters have been developed [4,3,22]. A state-space averaged model is an approximation to a model such as (2.1) that contains discrete control inputs, and can be obtained by replacing the instantaneous values of all state and control variables by their one-cycle averages, computed over an interval equal to the switching period of the converter. For example,

$$d(t) = \frac{1}{T} \int_{t-T}^{t} u(s)ds' \tag{2.5}$$

is the one-cycle average value of u. It is important to point out, as shown in [22], that since $d(t)$ can never have a fundamental frequency higher than half the switching frequency, the predictions of the continuous time averaged model at frequencies above this frequency $(1/2T)$ must be ignored.

The main motivation behind averaged models is that for practical purposes our interest is to regulate the average output at some fixed value, provided that the ripple or harmonics are sufficiently small. Also, small signal, linear averaged models, which can be easily obtained, serve to predict well the dynamics of small perturbations from a nominal operating point and can be used to obtain linear feedback controllers.

The large-signal state-space averaged model for a switching converter can be easily obtained by just replacing the exact control u in (2.1) by the duty ratio $d(t)$, now considered a continuous time function. Generally, the resulting model is still nonlinear since $d(t)$ is still the control input. However, this model predicts exceedingly well the average value of the ripple waveforms of the state $x(t)$ in the steady state (constant duty ratio $d(t) = D$, $0 < D < 1$). For example, if we substitute $u = D$ in (2.1) and set the derivatives to zero (steady-state condition) for the buck-boost converter, the resulting averaged inductor current and capacitor voltages relations are $I_L = V_{in}D/R(1-D)^2$ and $V_c = -V_{in}D/(1-D)$, respectively, and the latter expression

is just (2.3). Using the parameters given before, the results for this buck-boost converter are:$I_L = 22.22 amps$, $V_c = -133.33 volts$. The averaged, open loop response to a 10% initial perturbation on the steady-state value of the state for this system is shown in Figure 2.4. These plots represent the average values of the actual ripple waveforms of $x(t)$.

As mentioned before, the large-signal, averaged model is generally nonlinear. However, via the process of *linearization*, a linear small-signal model can be obtained which approximately describes small deviations from the nominal operating point of the system. The method consists in representing all nonlinearities in terms of deviations from steady state by a Taylor series expansion around nominal values. Then, retaining only linear or first order terms, the linear small-signal model results. After linearization, the resulting open-loop, small-signal, averaged LTI model has the general form

$$\delta x'(t) = [A_0 + D(A_1 - A_0)]\delta x(t) + [B_0 + D(B_1 - B_0)]\delta V_{in}(t) + [(A_1 - A_0)x_{ss} + (B_1 - B_0)V_{in}]\delta d(t)$$

$$(2.6)$$

or

$$\delta x'(t) = A_n \delta x(t) + B_n \delta V_{in}(t) + F_n \delta d(t) \qquad (2.7)$$

where x_{ss} is the (approximate) average value of the state vector corresponding to constant V_{in}, T, and D. From (2.6), transfer function descriptions relating perturbations in $\delta d(t)$ or $\delta V_{in}(t)$ to perturbations in state $\delta x(t)$ can be readily found and used for analysis or as a basis for designing a feedback control scheme, as will be shown in the next section. For the buck-boost converter, (2.6) takes the particular form

$$\delta x'(t) = \begin{pmatrix} 0 & \frac{D'}{L} \\ -\frac{D'}{C} & -\frac{1}{RC} \end{pmatrix} \delta x(t) + \begin{pmatrix} \frac{D}{L} \\ 0 \end{pmatrix} \delta V_{in}(t) + \begin{pmatrix} \frac{V_{in}-V_c}{L} \\ \frac{I_L}{C} \end{pmatrix} \delta d(t) \qquad (2.8)$$

where $D' = 1 - D$, and I_L, V_c are the averaged, steady-state inductor current and capacitor voltage, respectively.

$i_L(t)$

Time in seconds

$v_c(t)$

Time in seconds
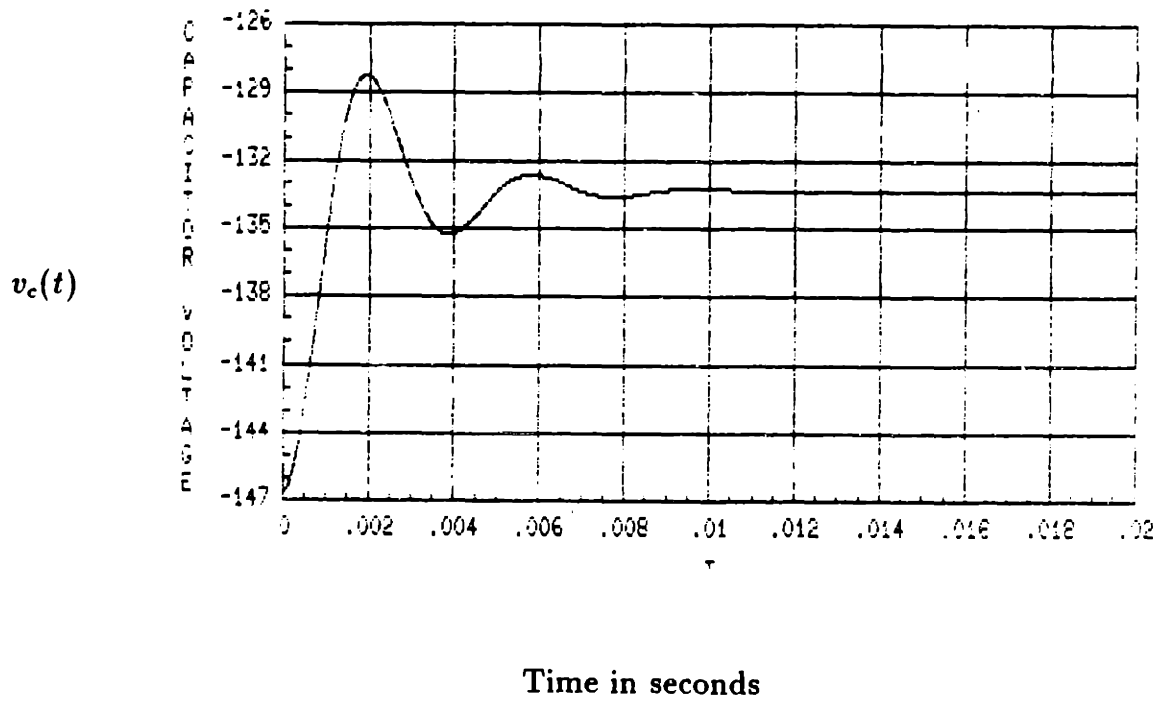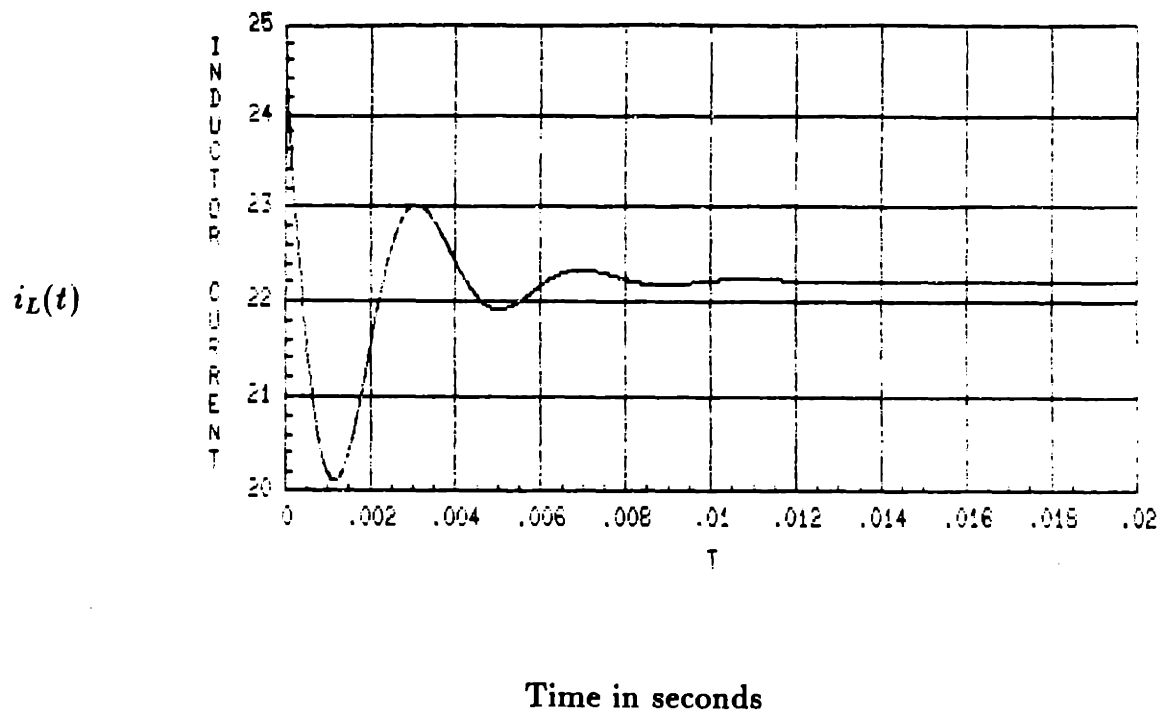
Figure 2.4: Buck-boost converter average transient response to a 10% perturbation from steady state

23

2.2   Current Mode Control

This section introduces basic concepts of a commonly used multiloop regulator scheme known as current mode control. Although no complete closed loop designs are analyzed, the main purpose is to later present a correction, see also [23], to the usual state-space averaged models for constant frequency, current mode controlled converters. This correction results in new small signal averaged models.

Current mode control is essentially a full state feedback control scheme. The control is implemented by sensing the following two quantities: the output voltage of the converter and the instantaneous current through the power switch. The principle is to regulate the output by sensing the inductor or switch current (current or ac loop) and comparing it with an output-derived reference level (i_P) in order to close the main feedback loop. The switch state transition time (and hence the duty cycle) during each cycle is determined when the switching current ascends and intersects the threshold level i_P. This threshold level (i_P), which is assumed to vary slowly (assumed constant over T- a switching period), is the output of an error compensator which has as input the error signal or difference between the output voltage and the desired reference voltage. Figure 2.5 illustrates a general current mode control scheme.

The inherent features of this control scheme are:

- Inherent pulse-by-pulse current limiting (transistor peak current protection)

- Allows easy paralleling of multiple power supply modules

- Easy hardware implementation

The key modeling task for control design is to obtain the open loop transfer function from small perturbations in i_P to small perturbations in average output voltage, with the current loop closed. Once this is obtained, classical compensation techniques such as shown in [18] can be used to design the voltage error amplifier in Fig. 2.5 in order

24

Switching

converter topology

V_{out}

i_L

Flip
Flop

comparator

i_L

i_p

Error
compensator

$-$

V_{ref}

clock
(period T)

i_p

i_L

d T

T
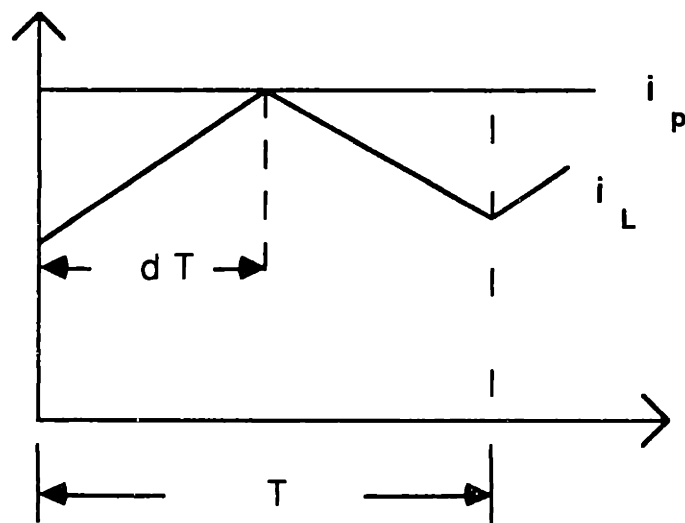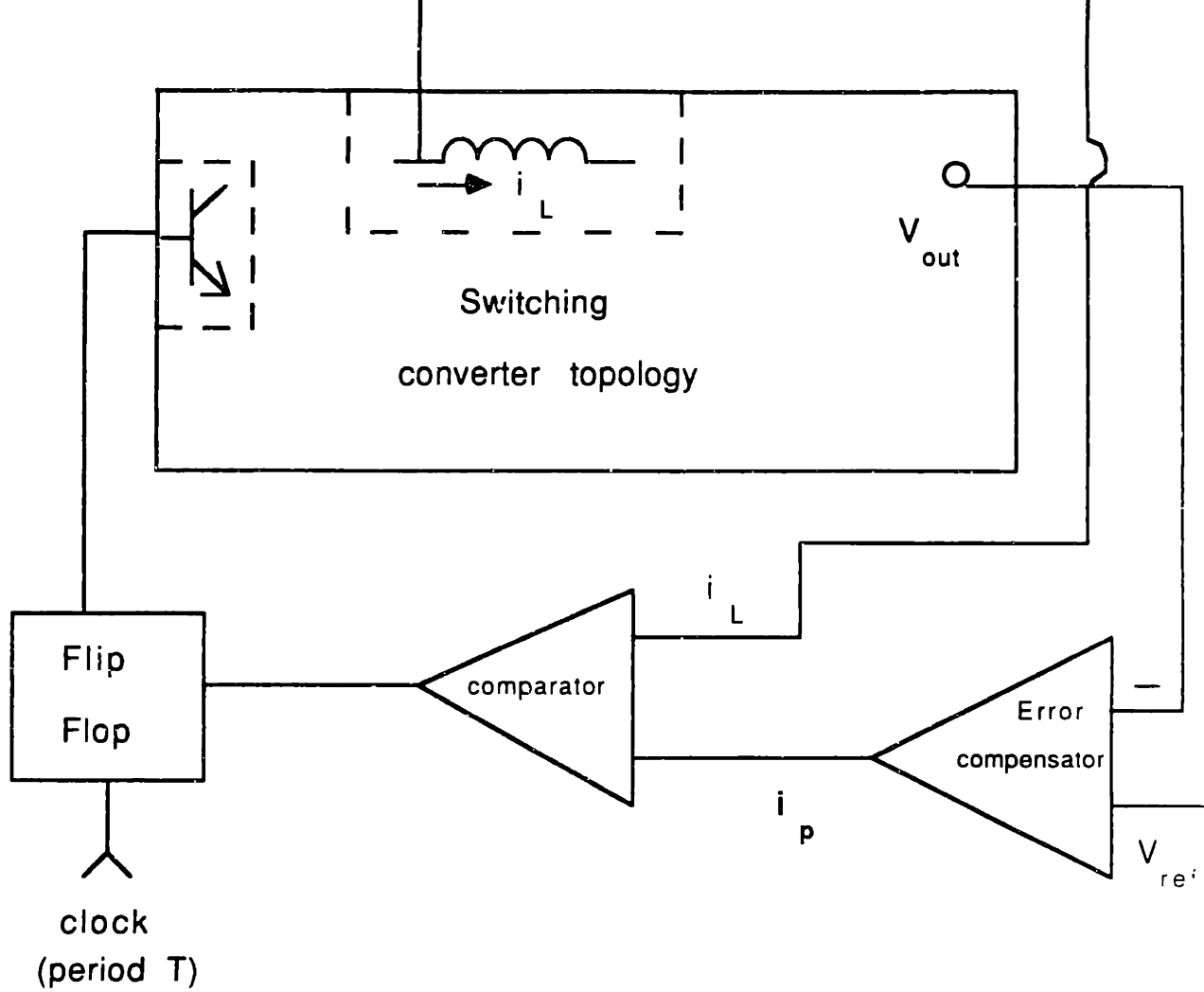
Figure 2.5: Current mode control scheme

to close the control loop. The correction to be introduced in the next section results in new open loop small signal transfer function descriptions. Before this, an inherent stability problem in current mode controlled converters will be mentioned.

2.2.1 Instabilities in current mode control

As discussed in [11], an inherent instability exists in the current loop for duty ratios greater than 0.5, unless a stabilizing ramp is introduced. This will be illustrated with Fig. 2.6, which shows general waveforms for a converter operating in current mode control. Analyzing Fig. 2.6(a) results in a current perturbation propagation from cycle to cycle of the form

$$\frac{\triangle I_{(N+1)T}}{\triangle I_{NT}} = -\frac{m_2}{m_1} \tag{2.9}$$

where m_1 and m_2 represent the inductor current slopes during charging and discharging operations, making the usual approximation that the inductor current waveforms are piecewise linear. Using the steady state condition,

$$m_1 D = m_2 (1 - D) \tag{2.10}$$

and substituting into (2.9) yields

$$\frac{\triangle I_{(N+1)T}}{\triangle I_{NT}} = -\frac{D}{1-D} \tag{2.11}$$

which shows the instability for $D > 1/2$, since for this range of D, $\triangle I_{(N+1)T}/ \triangle I_{NT} > -1$.

Using a stabilizing ramp as shown in Fig. 2.6 results in the following perturbation propagation:

$$\triangle I_{(N+1)T} = -\frac{m_2 - m_c}{m_1 + m_c} \triangle I_{NT} \tag{2.12}$$

As we can see, choosing the slope of the ramp to be $m_c = m_2$ forces all perturbations to damp out in exactly one period. A drawback of the stabilizing ramp is the inability to maintain a desired operating point as the duty ratio increases, since the intersection

26

point with the current stabilizing ramp becomes lower. This results in lower steady state values of inductor current and capacitor voltage than would be obtained for the same level of commanded reference level in the absence of the ramp.

2.3 Corrected Averaged Models for Current Mode Control

This section points out a subtle error in the usual derivation, [1]-[3], of small signal state-space averaged models for the dynamics of current mode controlled switched (CFCMC) dc-dc converters operating in continuous conduction.

Figure 2.7 shows the waveform of the inductor current $i_L(t)$ under CFCMC operation in continuous conduction. The converter switch is turned on every T seconds and turned off whenever $i_L(t)$ equals the sum of a control signal i_P and a compensating ramp of fixed slope $-M_C$ that restarts at 0 every cycle. (Extension to the case of a varying compensation slope $-m_C$ is easy.) Note that Fig. 2.7 is drawn for a *transient* condition. The usual switched converter approximation of representing the inductor current waveform as piecewise linear is made, with slopes m_1 and $-m_2$ during charging and discharging operations. As mentioned before, it is also assumed that these slopes, as well as the control signal i_P, change only slowly from cycle to cycle. Lower case letters without the time argument t will be used to denote slowly varying quantities, upper case letters to denote constants or steady-state values, and a ˆ above a symbol will denote a perturbation from steady state.

Denote the *average* inductor current over an interval of length T simply by i. Elementary geometrical calculations on Fig. 2.7 then show that

$$i = i_P - M_C dT - d(m_1 dT/2) - d'(m_2 d'T/2) \qquad (2.13)$$

where $d' = 1 - d$. In steady state, where $i_L(t) = i_L(t + T)$, we have the additional

27
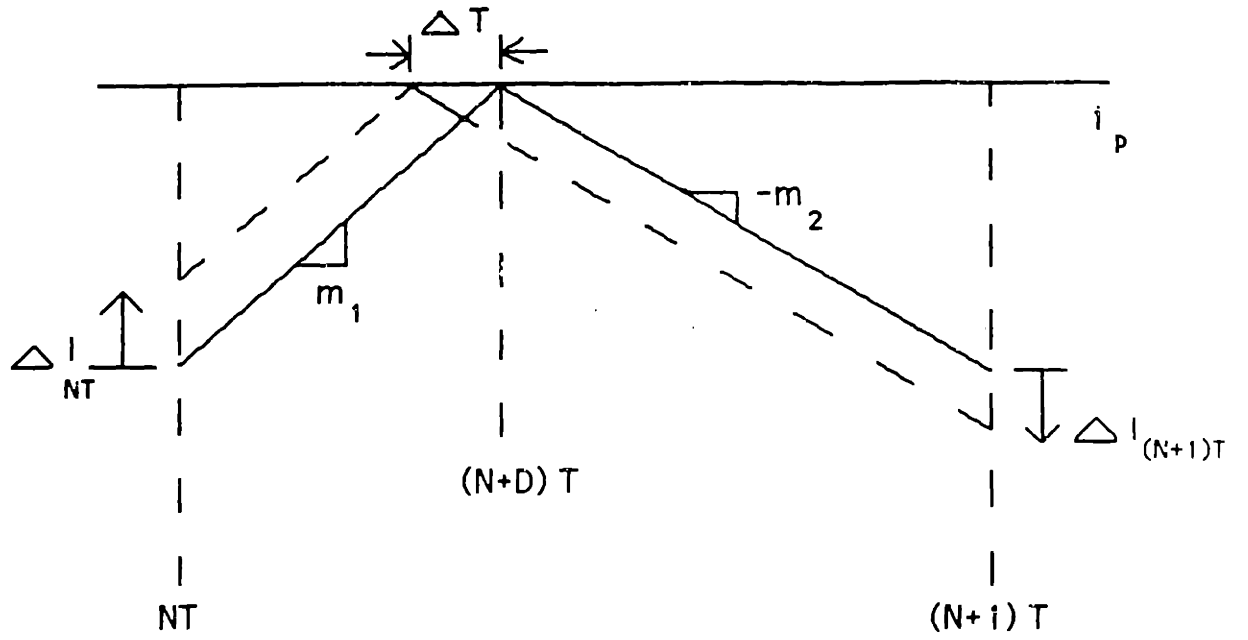
(a) no stabilizing ramp
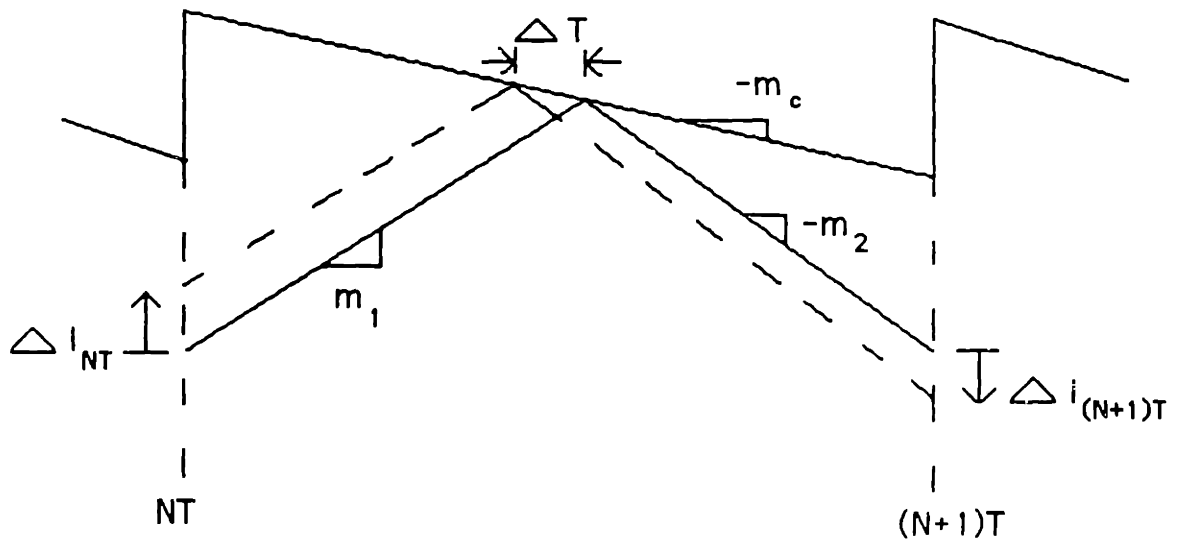
(b) with stabilizing ramp

Figure 2.6: Current perturbations propagation waveforms under current mode control
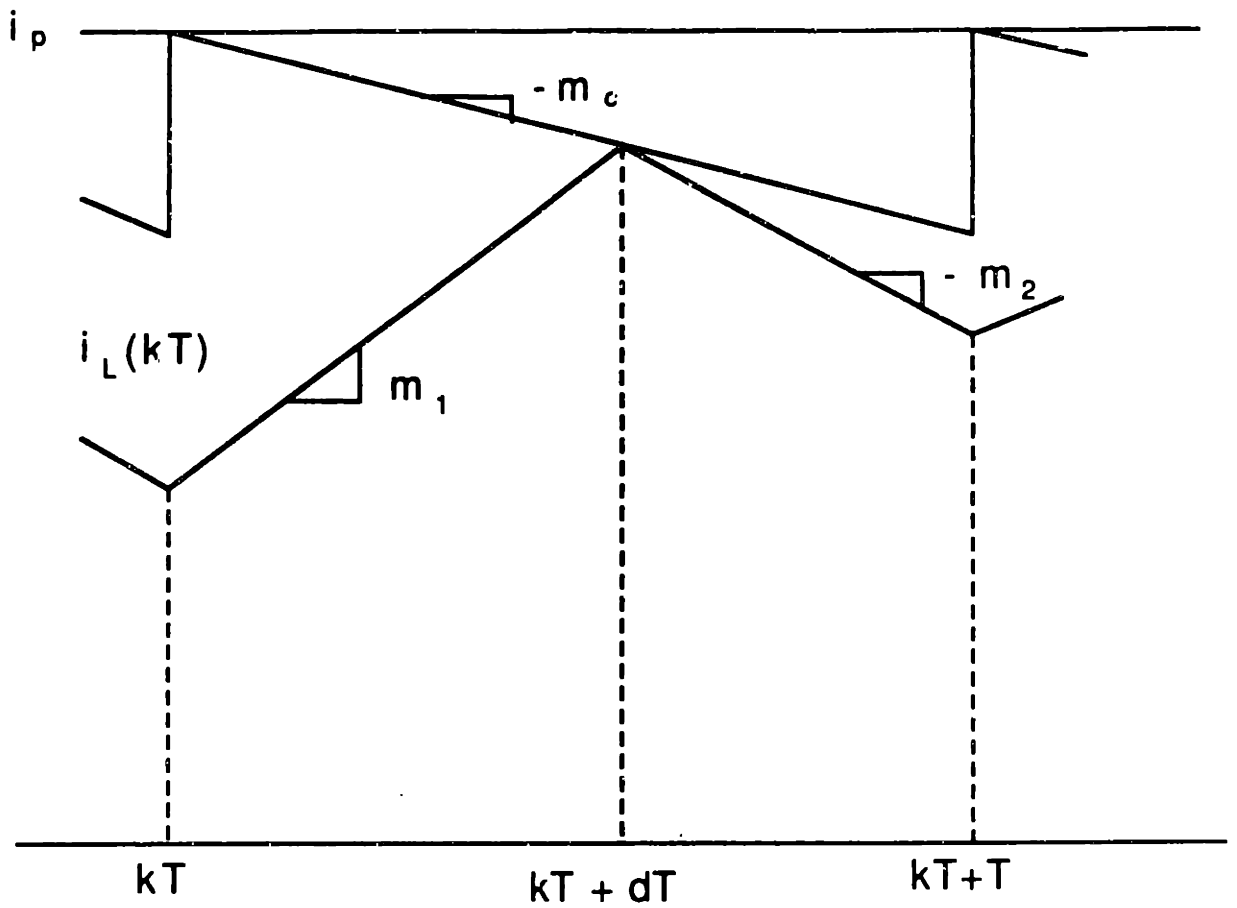
Figure 2.7: Inductor current waveform in CFCMC.

relation

$$M_1 D = M_2 D' \qquad\qquad (2.14)$$

where D, M_1 and M_2 are the steady-state value of d, m_1 and m_2 respectively. *If the system is in steady state*, then substitution of (2.14) in (2.13) *evaluated at steady state* yields $I = I_P - M_C DT - (D + D')M_1 DT/2$ or

$$I = I_P - [M_C + (M_1/2)]DT \qquad\qquad (2.15)$$

The flaw in the derivations in [1]-[3] is that (2.15) is treated as though it applied to the variables in the transient condition, i.e. it is treated as though it was $i = i_P - [M_C + (m_1/2)]dT$.

The correct procedure is to *first* perturb (2.13) and only *then* substitute in the nominal steady-state values as parameters. This results in the relationship $\hat{i} = \hat{i}_P - M_C T\hat{d} - (D^2 T/2)\hat{m}_1 - (D'^2 T/2)\hat{m}_2 - (M_1 D - M_2 D')T\hat{d}$ or, using (2.14),

$$\hat{i} = \hat{i}_P - M_C T\hat{d} - (D^2 T/2)\hat{m}_1 - (D'^2 T/2)\hat{m}_2 \qquad\qquad (2.16)$$

The usual derivation, on the other hand, obtains $\hat{i} = \hat{i}_P - [M_C + (M_1/2)]T\hat{d} - (DT/2)\hat{m}_1$.

The rest of the procedure suggested in [1]-[3] can now be followed, combining (2.16) with the usual open loop, small-signal, state-space averaged model for the converter being studied. The correct derivation results in non-trivial changes to the usual models.

2.3.1 Corrected results

Figure 2.1 shows the three basic voltage converter topologies. The large signal time-dependent line input and output voltages are u and v_o, the input and output currents are i_u and i_o (the capacitor is counted as part of the load for the analysis here), and the inductor current is i_L. Note that, since no capacitor ESR is assumed, the output voltage equals the capacitor voltage ($v_o = v_c = v$). As mentioned before, lower case

letters without time argument are used to denote slowly varying quantities, upper case letters to denote constants or steady state values, and ⌃ above a symbol denotes a perturbation from steady state. Recall that the relation given by (2.16) applies to any converter. The differences between converters result solely from how the inductor slopes m_1 and m_2 are dependent upon operating conditions. It is interesting to note that because of steady state assumptions made in [1]-[3] their small signal control law does not includes perturbations $\hat{m}_2$ in m_2. In the discussion to follow, R_F is used to denote the proportionality factor between the control input current to the comparator (i_P) and the voltage v_p that produces it, $i_P = v_P/R_F$.

Buck converter: During the switch on-time the inductor is connected between line input and output voltage u and v. During the switch-off time the inductor is connected across the capacitor-load combination. Not that in this topology the inductor current equals the output current ($i_L = i_o$). Thus,

$$\hat{m}_1 = \frac{\hat{u} - \hat{v}}{L}, \; \hat{m}_2 = \frac{\hat{v}}{L} \tag{2.17}$$

Substitution in (2.16) yields the small signal control law

$$M_c \hat{d} = \frac{1}{T} \left(\frac{\hat{v}_p}{R_F} - \hat{i}_L \right) - \frac{D^2}{2L} \hat{u} + \frac{(2D-1)}{2L} \hat{v} \tag{2.18}$$

Also, from the open loop, small-signal, state-space averaged model we obtain the relations

$$\frac{d}{dt} \hat{i}_L = -\frac{1}{L} \hat{v} + \frac{D}{L} \hat{u} + \frac{U}{L} \hat{d} \tag{2.19}$$

$$\frac{d}{dt} \hat{v} = \frac{1}{C} \hat{i}_L - \frac{1}{RC} \hat{v}$$

$$\hat{i}_u = D \hat{i}_L + I_L \hat{d}$$

$$\hat{i}_o = \hat{i}_L$$

where $I_L = DU/R$ is the averaged steady-state value of inductor current.

Boost converter: During the switch on-time the inductor is connected across the line input voltage u, while it is connected across the line and output voltages when the

switch is off. The inductor and input currents are the same ($i_L = i_o$). For this case

$$\hat{m}_1 = \frac{\hat{u}}{L}, \; \hat{m}_2 = \frac{\hat{u} - \hat{v}}{L} \tag{2.20}$$

Substitution of above expressions into (2.16) yields the small signal control law

$$M_c \hat{d} = \frac{1}{T} \left(\frac{\hat{v}_P}{R_F} - \hat{i}_L \right) - \frac{D^2 + D'^2}{2L} \hat{u} + \frac{D'^2}{2L} \hat{v} \tag{2.21}$$

Open loop, small-signal, state-space averaged model relations can be found to be

$$\begin{aligned}
\frac{d}{dt} \hat{i}_L &= -\frac{D'}{L} \hat{v} + \frac{1}{L} \hat{u} + \frac{V_c}{L} \hat{d} \\
\frac{d}{dt} \hat{v} &= \frac{D'}{C} \hat{i}_L - \frac{1}{RC} \hat{v} - \frac{I_L}{C} \hat{d} \\
\hat{i}_u &= \hat{i}_L \\
\hat{i}_o &= D' \hat{i}_L - I_L \hat{d}
\end{aligned} \tag{2.22}$$

where $I_L = U/RD'^2$ and $V_c = U/D'$ are the averaged, steady-state inductor current and output (capacitor) voltage, respectively.

Euck-boost converter: During the switch on-time (transistor on) the inductor is connected across the input voltage while during the off cycle it is connected across the output load. Then

$$\hat{m}_1 = \frac{\hat{u}}{L}, \; \hat{m}_2 = -\frac{\hat{v}}{L} \tag{2.23}$$

Substitution into (2.16) gives the small signal current mode control law as

$$M_c \hat{d} = \frac{1}{T} \left(\frac{\hat{v}_P}{R_F} - \hat{i}_L \right) - \frac{D^2}{2L} \hat{u} + \frac{D'^2}{2L} \hat{v} \tag{2.24}$$

From the open loop, small-signal, state-space averaged model

$$\begin{aligned}
\frac{d}{dt} \hat{i}_L &= \frac{D'}{L} \hat{v} + \frac{D}{L} \hat{u} + \frac{U - V_c}{L} \hat{d} \\
\frac{d}{dt} \hat{v} &= -\frac{D'}{C} \hat{i}_L - \frac{1}{RC} \hat{v} + \frac{I_L}{C} \hat{d} \\
\hat{i}_u &= D \hat{i}_L + I_L \hat{d} \\
\hat{i}_o &= -D' \hat{i}_L + I_L \hat{d}
\end{aligned} \tag{2.25}$$

where $I_L = UD/(RD'^2)$, $V_c = -UD/D'$ are the averaged, steady-state inductor current and capacitor voltage, respectively.

Equations (2.18),(2.21), and (2.24) give the corrected small signal control law relations for current mode control. It is interesting to note that when no compensating ramp is used ($M_c = 0$), $\hat{d}$ is completely eliminated from the control law for each converter. This results in the closed loop system becoming first order when no compensating ramp is used, and this is the major fact which is missed by the approach taken in [1]-[3]. For example, in the buck-boost converter case, the control law derived in [2] takes the form

$$\hat{d} = \frac{1}{T\left(\frac{U}{2L} + M_c\right)}\left(\frac{\hat{v}_P}{R_F} - \hat{i}_L\right) - \frac{D}{U + 2M_cL}\hat{u} \tag{2.26}$$

Note that not only the ac perturbation $\hat{d}$ still appears in the control law when $M_c = 0$ but this constraint also fails to include perturbations in the output voltage ($\hat{v}$).

2.3.2   Illustrative special case

To further illustrate and clarify the new results introduced by the corrected small signal control relations, the small signal frequency domain relationship between $\hat{i}_P$ and $\hat{v}$ for the buck-boost converter was derived by combining (2.24) with the open loop, small-signal, averaged model. As indicated before, this is the key modeling task for control design, since it is this transfer function which is needed to design the output voltage error amplifier, which in turns determines i_P, thus closing the main or outer feedback loop. The resulting transfer function is

$$\frac{\hat{v}(s)}{\hat{i}_P(s)} = \frac{\frac{DU}{D'^2RC}s - \frac{U}{LC}}{M_cT\,s^2 + \left[\frac{U}{D'L} - \frac{DTU}{2RLC} + \frac{M_cT}{RC}\right]s + \left[\frac{(1+D)U}{D'RLC} + \frac{D'^2TU}{2L^2C} + \frac{M_cD'^2T}{LC}\right]} \tag{2.27}$$

The above transfer function (2.27) has two poles on the negative real axis and a right half-plane zero. However, note that for no compensating ramp ($M_c = 0$) the relation effectively becomes first order (only one pole). This can be traced to the fact that $\hat{d}$

does not appears in (2.24) when $M_c = 0$. The usual transfer function, which can be obtained by combining (2.26) with the open loop, small-signal, averaged model gives

$$\frac{\hat{v}(s)}{\hat{i}_P(s)} = \frac{\frac{DU}{D'^2RC}s - \frac{U}{LC}}{\frac{T(U+2M_cL)}{2L}s^2 + \left[\frac{U}{D'L} + \frac{T(U+2M_cL)}{2RLC}\right]s + \left[\frac{U(1+D)}{D'RLC} + \frac{TD'^2(U+2M_cL)}{2L^2C}\right]} \qquad (2.28)$$

The above transfer function also has a right-half plane zero and two poles on the negative real axis. The right-half plane zero in (2.27) and (2.28) is the same for both methods. However, as can be noticed from (2.28), substitution of $M_c = 0$ in (2.28) still results in a second order system with a high frequency pole which is spurious to the averaged model. It turns out (not so obvious from transfer functions) that the low frequency (dominant pole) in (2.27) and (2.28) is the same for both methods and is independent of M_c. The high frequency pole is different for both relations and depends on the compensating ramp slope (it goes away in (2.27) for no compensating ramp).

To illustrate this point, a pole root locus of (2.27) and (2.28) as M_c is varied is shown in Fig. 2.8 for a buck-boost converter with typical parameter values ($D = 0.5, T = 50\mu sec$). M_c was varied from twenty-five percent below to above the commonly used value of $M_c = M_2 = DU/D'L$, which is the negative slope of the inductor current during the switch off time. Note that the usual and corrected models give the same dominant pole at -1.75×10^3. The high frequency pole moves to the right on the real axis as M_c is increased for both models. However, for $M_c = 0.75M_2$ our model predicts a pole which can be neglected since it is still higher than half the switching frequency, while the usual model predicts a pole at about a quarter of the switching frequency.

Figure 2.9 shows a Bode plot comparison of the transfer function between $\hat{i}_P$ and $\hat{v}$ for the usual and corrected models using a buck-boost converter with the same parameters as before but with $D = 0.2$ and $M_c = 0$ (no compensating ramp is needed in principle since $D < 0.5$). One-half the switching frequency is located at 6.3×10^4 radians per second. For low frequencies the two models are equivalent. For high enough frequencies our model shows the expected one pole behavior while the usual model

34
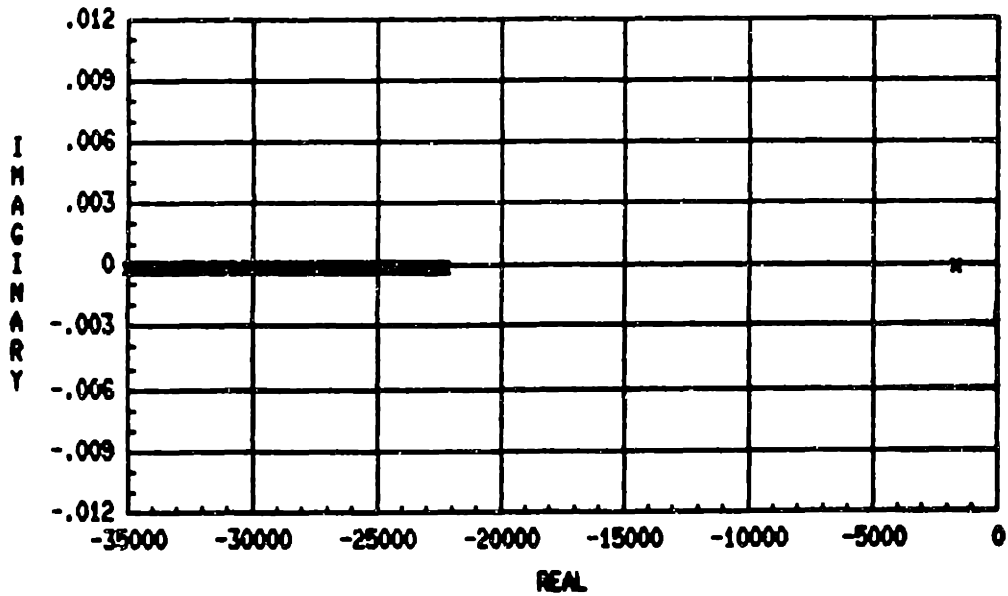
(a) corrected model

(b) usual model

Figure 2.8: Pole loci transfer function of (a) corrected model and (b) usual model.

35

starts to deviate at about a decade before one-half the switching frequency because of the addition of a second (non-existing) pole at -4.97×10^4. The exact sampled-data model response computed via the procedure described in [7] is also included for comparison. (The latter response is obtained by making the substitution $z = exp(jwT)$ in the z-transform function of the sampled-data model.) Evidently our model does as well as the usual model, despite having one less pole: both the averaged models begin to deviate from the sampled-data model at around the same frequency.

2.3.3 Y-parameters

Equations (2.17) thru (2.25) are enough to obtain any transfer function of interest (e.g. line-to-output, output impedance) for any of the converter topologies shown here. However, in order to simplify the design process it is convenient as shown in [2] to absorb the current loop into a y-parameter model as in Figure 2.10. This model serves to easily and systematically obtain frequency domain relationships between line, output, and control voltages and currents which are needed in analysis and control design. In [2], the y-parameters are derived from equivalent circuit models in which the usual (incorrect) small signal control law is used in the current loop. As expected, the resulting parameters fail to predict the single-pole behavior when no compensating ramp is used. For reference and comparison purposes, the corrected y-parameters were derived and are shown in Tables 2.1 - 2.3.

36
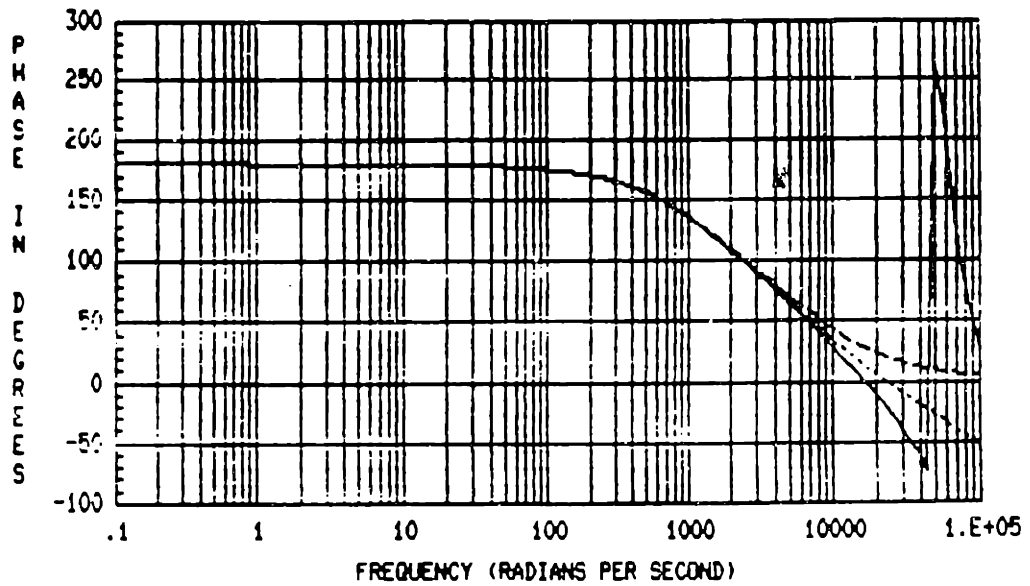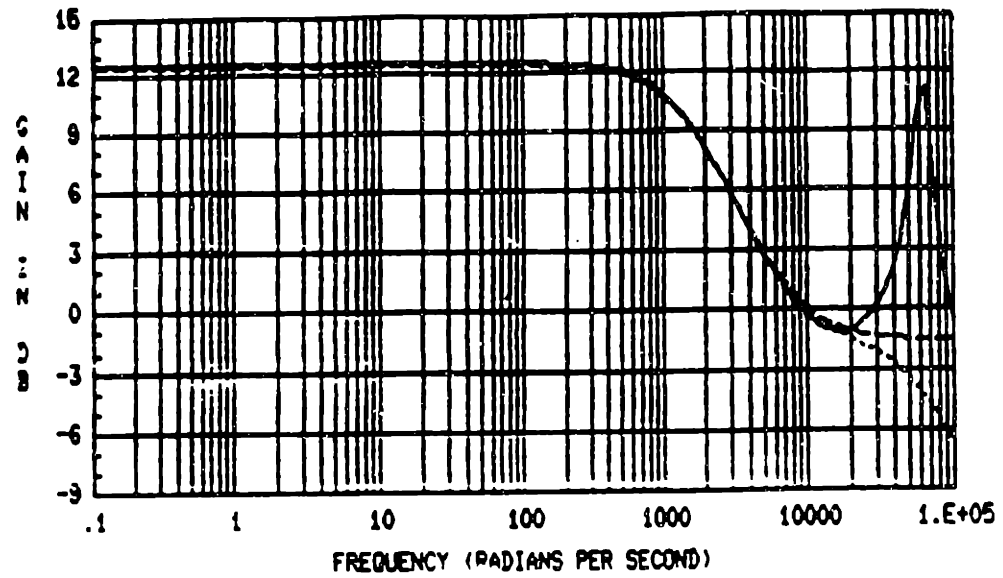
Figure 2.9: Bode plot for $\hat{v}(s)/\hat{i}_P(s)$.

——————————— 'exact' sampled-data model

- - - - - - - - - - - - one-pole average model

.... two-pole average model

37
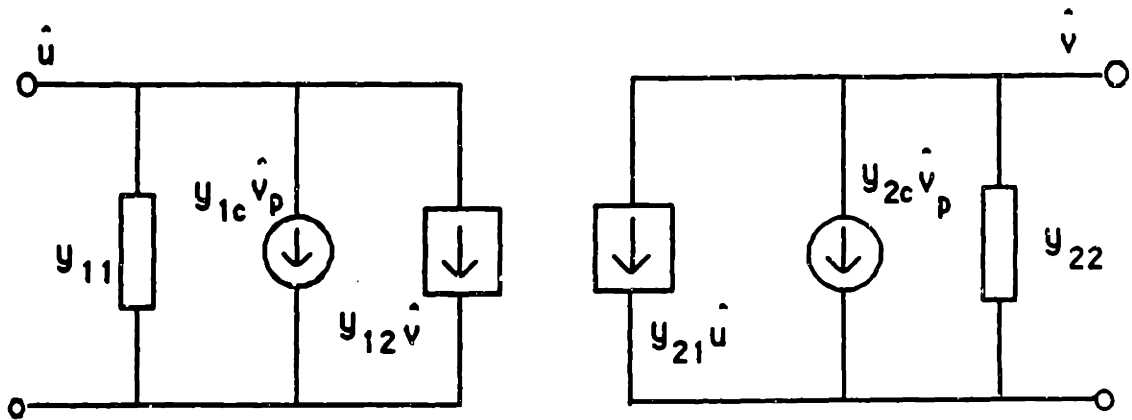
Figure 2.10: Model in y-parameter form.

The corrected y-parameters can easily and systematically be derived. For illustration purposes, y_{2C} or the short-circuit output current as a function of the control voltage v_P with zero input voltage will be derived next for the buck-boost converter using (2.24) and (2.25). From Fig. 2.10, the definition of y_{2C} is

$$y_{2C}(s) = \frac{\hat{i}_o(s)}{\hat{v}_P(s)} \Big|_{\hat{v}=\hat{u}=0} \qquad (2.29)$$

For this condition the corrected small signal control law (2.24) takes the form

$$M_c\hat{d} = -\frac{1}{T}\hat{i}_L + \frac{1}{TR_F}\hat{v}_P \qquad (2.30)$$

Substituting (2.30) into the appropiate small signal, open loop relations in (2.25) and taking the Laplace transform yields

$$\left(s + \frac{U - V_c}{M_cLT}\right)\hat{i}_L(s) = \frac{U - V_c}{M_cLTR_F}\hat{v}_P(s) \qquad (2.31)$$

$$\hat{i}_o(s) = -\left(D' + \frac{I_L}{M_cT}\right)\hat{i}_L(s) + \frac{I_L}{M_cTR_F}\hat{v}_P(s)$$

Combining the two equations above, it is straightforward to obtain $y_{2C}(s)$ for the buck-boost converter. This y-parameter model is also sufficient to determine the output

y's	buck
y11	$-\dfrac{\dfrac{D^2 I_L}{2L}s + \dfrac{D^3 TU + 2LDI_L - 2M_c D^2 LT}{2L^2 T}}{M_c s + \dfrac{U}{TL}}$
y1c	$\dfrac{\dfrac{1}{TR_F L}(I_L Ls + DU)}{M_c s + \dfrac{U}{TL}}$
y12	$\dfrac{\dfrac{I_L(2D-1)}{2L}s + \dfrac{DT(2D-1)U + 2I_L L - 2M_c DTL}{2TL^2}}{M_c s + \dfrac{U}{TL}}$
y21	$\dfrac{\dfrac{D}{2L^2}(DU - 2M_c L)}{M_c s + \dfrac{U}{TL}}$
y2c	$\dfrac{-\dfrac{U}{TR_F L}}{M_c s + \dfrac{U}{TL}}$
y22	$\dfrac{\dfrac{1}{2L^2}[2M_c L - (2D-1)U]}{M_c s + \dfrac{U}{TL}}$

Table 2.1: Y-parameter expressions for buck converter.

y's	boost
y11	$$\dfrac{\frac{1}{L}\left[M_c-\frac{V_c(D^2+D'^2)}{2L}\right]}{M_c s+\frac{V_c}{TL}}$$
y1c	$$\dfrac{\frac{V_c}{TR_FL}}{M_c s+\frac{V_c}{TL}}$$
y12	$$\dfrac{\frac{D'}{2L^2}(D'V_c-2LM_c)}{M_c s+\frac{V_c}{TL}}$$
y21	$$\dfrac{\frac{-I_L(D'^2+D'^2)}{2L}s+\frac{D'(D^2+D'^2)TV_c-2I_LL-2M_cD'TL}{2TL^2}}{M_c s+\frac{V_c}{TL}}$$
y2c	$$\dfrac{\frac{1}{TR_FL}(I_LLs-D'V_c)}{M_c s+\frac{V_c}{TL}}$$
y22	$$\dfrac{\frac{D'^2I_L}{2L}s+\frac{2D'I_LL-D'^3TV_c+2M_cD'^2TL}{2TL^2}}{M_c s+\frac{V_c}{TL}}$$

Table 2.2: Y-parameter expressions for boost converter.

y's	buck-boost
y11	$$\frac{\frac{-1}{2TL^2}\left[D^2I_LTLs+(D^3(U-V_c)T+2DI_LL-2D^2M_cTL)\right]}{M_cs+\frac{U-V_c}{TL}}$$
y1c	$$\frac{\frac{1}{TR_FL}[I_LLs+D(U-V_c)]}{M_cs+\frac{U-V_c}{TL}}$$
y12	$$\frac{\frac{D'^2I_L}{2L}s+\frac{[DD'^2T(U-V_c)-2D'I_LL+2M_cDD'TL]}{2TL^2}}{M_cs+\frac{U-V_c}{TL}}$$
y21	$$\frac{\frac{D^2I_L}{2L}s+\frac{2DI_LL-D^2D'T(U-V_c)+2M_cDD'TL}{2TL^2}}{M_cs+\frac{U-V_c}{TL}}$$
y2c	$$\frac{\frac{-1}{TR_FL}[I_LLs-D'(U-V_c)]}{M_cs+\frac{U-V_c}{TL}}$$
y22	$$\frac{\frac{-D'^2I_L}{2L}s+\frac{D'^3T(U-V_c)+2D'I_LL+2M_cD'^2TL}{2TL^2}}{M_cs+\frac{U-V_c}{TL}}$$

Table 2.3: Y-parameter expressions for buck-boost converter.

41

voltage and line input currents as functions of the control voltage (v_p) and the line input voltage.

The y-parameters pole from Tables 2.1 - 2.3 can be expressed in the general form (for all converters) as $w_c = w_s M_1 / 2\pi M_c D'$, where $w_s = 2\pi / T$. In [2], the equivalent result is $w_c = w_s M_1 / 2\pi (M_1 / 2 + M_c) D'$. Thus, it is mistakenly concluded there that for no stabilizing ramp ($M_c = 0$) this pole varies from about a third to two-thirds of the switching frequency while in fact this pole is spurious to the averaged model ($w_c \rightarrow -\infty$). If the stabilizing ramp is chosen so that $M_c = M_2$ and (2.14) is used in the expressions for w_c, it can be easily shown that as D is varied from 0 to 1 the pole from [2] varies from about a sixth to a third of the switching frequency w_s while our pole can vary all the way from a sixth of the switching frequency for $D = 1$ to $-\infty$ for $D = 0$. However, since the stabilizing ramp is only normally used for $D \geq 0.5$ (region of instability), it is important to point out that for $D = 0.5$ and $M_c = M_2$ our y-parameters pole is at about a third of the switching frequency.

2.4   Approximate Sampled-Data Models

Sampled data models provide a natural setting for describing systems in which the control is exercised once each cycle. Consider, for example, the buck-boost converter in Fig. 2.1 switching between topologies described by state-space descriptions of the form:

$$\dot{x}(t) = A_l x(t) + B_l u(t) \quad l = 1, 2 \tag{2.32}$$

Let the system be in topology $l = 1$ for a time T_1 and in topology $l = 2$ for a time T_2.

Duty Ratio Control: The period T can be expressed in terms of a duty ratio d_k in the kth cycle, $0 \leq d_k \leq 1$:

$$T = T_1 + T_2$$

$$= d_k T + (1 - d_k)T$$

$$= d_k T + d'_k T$$

The large signal sampled data model (SDM) can be obtained by integrating the state equations over one period of operation using the superposition integral, see [7] for example. The assumption that $u(t)$ is constant in each topology for any particular switching cycle is used to simplify the expressions. During T_1, the switch is on, and the state x_{k+d_k} at $t = kT + d_k T$ is given by:

$$x_{k+d_k} = F_1 x_k + H_1 u_k \tag{2.33}$$

where

$$F_1 = e^{A_1 d_k T} \quad H_1 = \int_0^{d_k T} e^{A_1 \tau} B_1 d\tau \tag{2.34}$$

Similarly, during T_2, the switch is off, and the state at $t = kT + T$ is given by:

$$x_{k+1} = F_2 x_{k+d_k} \tag{2.35}$$
$$+ H_2 u_{k+d_k}$$

where

$$F_2 = e^{A_2 d'_k T} \quad H_2 = \int_0^{d'_k T} e^{A_2 \tau} B_2 d\tau \tag{2.36}$$

The sampled data model provides a cycle to cycle description that can be chosen to track either the 'valleys' or the 'peaks' of the state waveforms. The valley to valley description is constructed by piecing together (2.33) and (2.35) to obtain:

$$x_{k+1} = F_2 F_1 x_k + (F_2 H_1 + H_2) u_k \tag{2.37}$$

The peak to peak description can be constructed similarly, resulting in:

$$x_{k+d_k+1} = F_1 F_2 x_{k+d_k} \tag{2.38}$$
$$+ (F_1 H_2 + H_1) u_{k+d_k}$$

43

The remainder of this section will focus on the valley to valley description (2.37).

The derivation of a sampled data model can be simplified greatly by approximating the matrix exponential by:

$$e^{A_l T} \approx I + A_l T \tag{2.39}$$

and by discarding quadratic terms in T when taking the product of matrix exponentials. The resulting approximate sampled data model is given by:

$$
\begin{aligned}
x_{k+1} &\approx (I + <A>_{d_k} T) x_k \\
&+ <B>_{d_k} T u_k
\end{aligned}
\tag{2.40}
$$

As before, d_k is the duty ratio in the kth cycle, and

$$<A>_{d_k} = A_1 d_k + A_2 d'_k \tag{2.41}$$

with a similar expression for $<B>_{d_k}$. The model makes the same approximations that underlie continuous time state-space averaged models, [4], [12], but is preserved and exploited as a discrete-time model. It is obtained with as little effort as the usual averaged models.

To illustrate the simplicity of these expressions, the large signal approximate SDM for the buck-boost converter where $x = [i_L \ v_c]^T$ is given by:

$$
\begin{aligned}
x_{k+1} &= \begin{bmatrix} 1 & \frac{d'_k T}{L} \\ \frac{-d'_k T}{C} & 1 - \frac{T}{RC} \end{bmatrix} x_k \\
&+ \begin{bmatrix} \frac{d_k T}{L} \\ 0 \end{bmatrix} u_k
\end{aligned}
\tag{2.42}
$$

To demonstrate the ability of (2.40) and (2.42) to represent the behavior of the actual system for large and fast variations in duty ratio, Figs. 2.11 and 2.12 show time domain simulations of the buck-boost converter in which the duty ratio is alternated between $d_k = 0$ and $d_k = 1$ in successive periods. These results were obtained by Krishna Mahabir. The solid line shows the trajectory of the (valley points of the) current in the

44
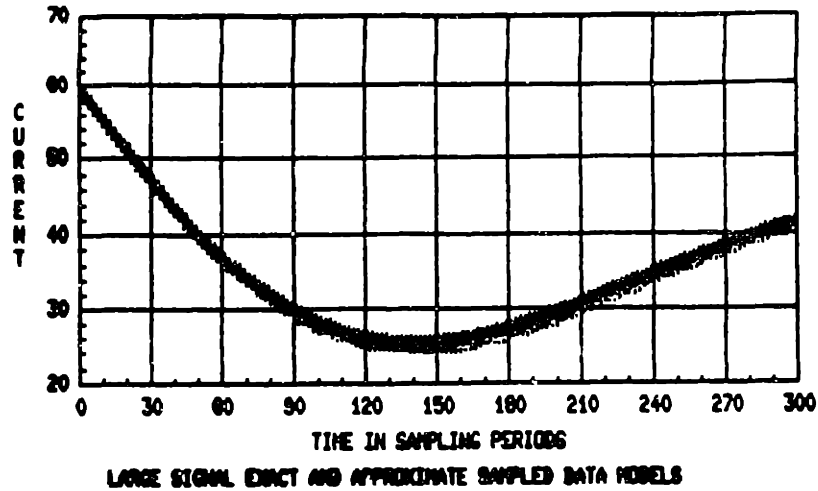
Figure 2.11: Trajectories of 'valley' points for current transient in exact and approximate sampled-data models.

exact sampled data model discussed at the beginning of this section, while the dotted line applies to the approximate SDM (2.42). The exact and approximate SDMs are initiated with the same initial condition, $X_{init} = [60 \quad -300]^T$ away from the operating point, $X_0 = [40 \quad -200]^T$. Figure 2.11 shows a portion of the current transients a short time after the system is initiated, while Fig. 2.12 shows the current transients in steady state. Similar plots are obtained for the voltage transients. Figure 2.12 shows that the current predicted by the approximate large-signal SDM differs from the actual value by about 1.5 percent. Similarly, the voltage transient predicted by the approximate large-signal SDM differs from the actual value by about 0.5 percent. Greater accuracy can be achieved easily by retaining quadratic terms in T when taking the products of matrix exponentials.

The approximate small-signal SDM can be obtained by linearizing (2.42), resulting

45
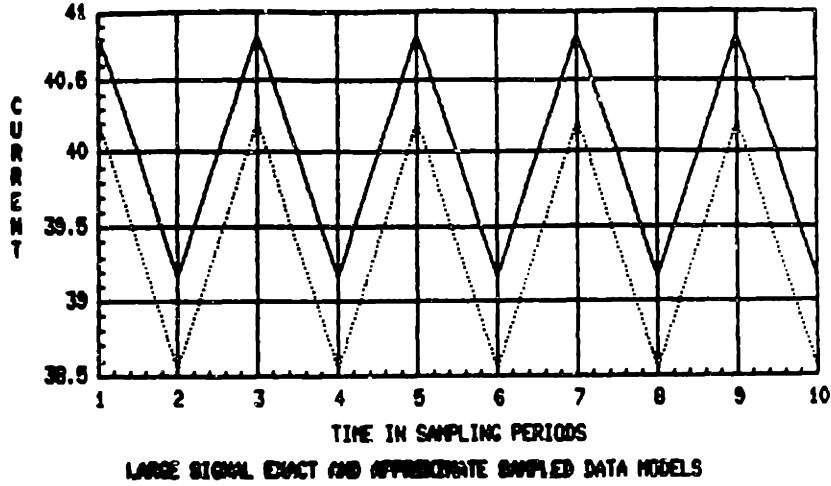
Figure 2.12: Trajectories of 'valley' points of steady state current in exact (—) and approximate (...) sampled-data models.

in:

$$\hat{x}_{k+1} = \begin{bmatrix} 1 & \frac{(1-D)T}{L} \\ \frac{-(1-D)T}{C} & 1 - \frac{T}{RC} \end{bmatrix} \hat{x}_k$$
$$+ \left\{ \begin{bmatrix} 0 & -\frac{T}{L} \\ \frac{T}{C} & 0 \end{bmatrix} X + \begin{bmatrix} \frac{T}{L} \\ 0 \end{bmatrix} U \right\} \hat{d}_k \tag{2.43}$$

where $X = [I, V]^T$ is the operating point. (We have assumed u_k is constant for simplicity). For our circuit example, the frequency response of (2.43) and of the *exact* small-signal SDM are essentially identical.

Current Mode Control: If the converter in (2.42) is in CFCMC operation, then Fig. 2.7 shows that we have the constraint

$$i_k + m_1 d_k T = i_{P,k} - M_C d_k T \tag{2.44}$$

where $i_{P,k}$ is the value of i_P in the kth cycle, so

$$d_k = [i_{P,k} - i_k]/(m_1 + M_C)T \tag{2.45}$$

46

This is combined with (2.40) to yield the desired approximate large-signal SDM for a CFCMC converter, which can then be linearized about the steady state to produce a small-signal model.

Substituting the differential constraint resulting from (2.45), namely

$$\hat{d}_k = -\hat{i}_k/(M_1 + M_C)T$$
$$+ \hat{i}_{P,k}/(M_1 + M_C)T \tag{2.46}$$

into (2.43) produces the approximate small-signal model under CFCMC. As an illustration, we shall write this model explicitly for the case where the stabilizing ramp is absent, i.e. $M_c = 0$. Substituting (2.46)) into the approximate small-signal SDM (2.43) and simplifying we get

$$
\hat{x}_{k+1} = \begin{bmatrix} -M_2/M_1 & \frac{(1-D)T}{L} \\ \frac{-DT+I/M_1}{C} & 1 - \frac{T}{RC} \end{bmatrix} \hat{x}_k \\
+ \left\{ \begin{bmatrix} 0 & -\frac{T}{L} \\ \frac{T}{C} & 0 \end{bmatrix} X \right. \\
+ \left. \begin{bmatrix} \frac{T}{L} \\ 0 \end{bmatrix} U \right\} \hat{i}_{P,k}/(M_1 + M_C)T
\tag{2.47}
$$

The open loop current perturbations are governed by:

$$\hat{i}_{k+1} = -\frac{M_2}{M_1}\hat{i}_k + \frac{(1-D)T}{L}\hat{v}_k \tag{2.48}$$

The first term is the expression predicted by the standard linearized analysis, while the second is a weak coupling term that can be neglected for the parameters in our example. Employing the steady state constraint (2.14) yields

$$\hat{i}_{k+1} \approx -\frac{D}{1-D}\hat{i}_k \tag{2.49}$$

This is the formula usually invoked to explain the instability for $D > 0.5$, see (2.11). Ignoring the weak coupling terms in (2.47), the eigenvalues of the approximate small-signal SDM operating under CFCMC are approximately given by:

$$-\frac{M_2}{M_1}, \ (1 - \frac{T}{RC}) \tag{2.50}$$

47
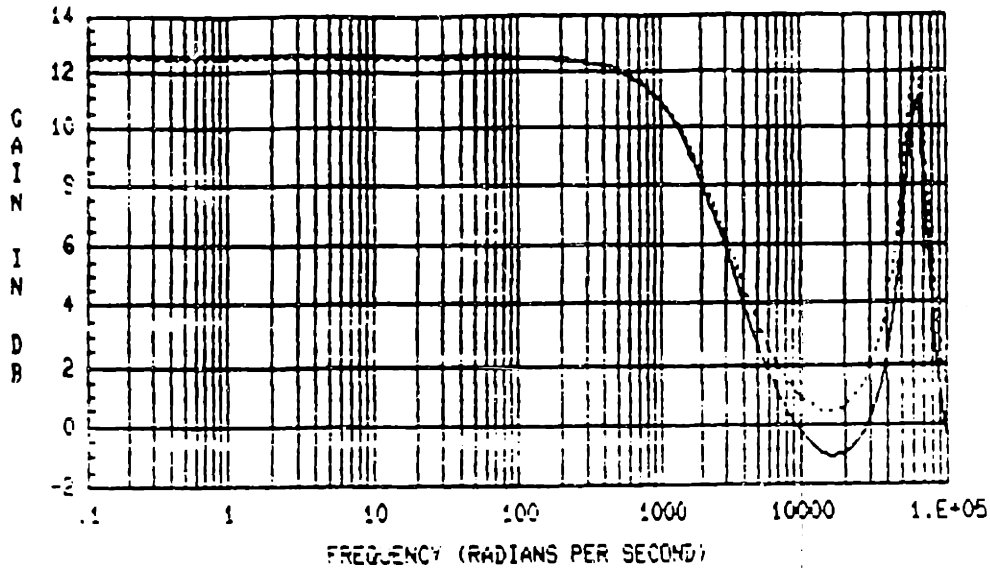
Figure 2.13: Bode plot for exact (—) and approximate (...) sampled-data models.

One eigenvalue is fixed inside the unit circle, near 1 for typical component values, while the other eigenvalue is negative and depends on the duty ratio.

The Bode plot in Fig. 2.13 compare the frequency responses of the exact and approximate small-signal SDM's for the buck-boost example of before operating under CFCMC. Note the great improvement over the averaged model results of Fig. 2.9. By retaining second-order terms in T, but still making the straight-line approximations for each segment of trajectory, we end up approximating $e^{A_2 d'T} e^{A_1 dT}$ by $I + <A>_d T + A_2 A_1 dd' T^2$ and so on. The resulting model generates a small-signal frequency response for our buck-boost example that is essentially indistinguishable from the results of the exact model. This section suggests that approximate sampled-data models may form a far better basis for analysis and control design for CFCMC converters.

48

Chapter 3

Models for Multiple Output Converters

In this chapter, the two-switch two-output half-bridge converter is presented and analyzed in order to show an example of the operation and dynamic modeling of a genuine multivariable switching power supply.

3.1   Two Output Half-Bridge Converter

When multiple regulated DC voltages are required by an electronic system, use is normally made of a single converter with multiple outputs coupled magnetically through a transformer. The addition of a transformer to the topology of a high frequency switching converter provides input-output isolation. Also, the transformer permits a turns ratio that avoids the small duty ratios and high peak currents which would arise if input and output voltage conversion ratios were far from unity, and thus reduces semiconductor component stresses.

Figure 3.1 shows a typical *buck derived* transformer-isolated half-bridge voltage converter with two outputs on the secondary side. The term *buck derived* means that, after appropiate transformation, this converter can be modeled as the basic buck converter. The input power is first rectified and filtered to form a DC link, as represented

by V_I. Power is transferred from the primary to the first output load (R_1) by diodes $D1$ and $D2$. Similarly, for the second output (R_2), power is transferred by diodes $D3$ and $D4$. As will be seen, the effect of the magnetic amplifier or auxiliary switch on the second output is to delay this transferring of power so that the second load can simultaneously be regulated at another nominal operating point. Since only $V_I/2$ is applied to the transformer primary, the half-bridge converter is mainly used for higher input voltage applications.

The half-bridge converter permits operation in both first and third quadrants of its transformer B-H characteristic curve. Thus, assuming that the two control switches $S1$ and $S2$ in Fig. 3.1 operate 180 degrees apart and have equal ON times and saturation voltages, it can be seen that the half-bridge converter transformer operation can be inherently balanced. Furthermore, the effective frequency of operation is twice the switching frequency of either $S1$ or $S2$. Using the latter argument and assuming the transformer to have ideal magnetic characteristics, the half-bridge converter can be described by the equivalent circuit shown in Fig. 3.2. Note that the equivalent periodic input voltage (on the secondary side), V_{eq}, in Fig. 3.2 incorporates both the transformer turns ratio and the frequency doubling effects. Although simplified, the circuit of Fig. 3.2 conveys the same information as Fig. 3.1 and can easily be used, as will be shown, to obtain the dynamic equations governing the system during each configuration.

The model shown in Fig. 3.2 has the following notation:
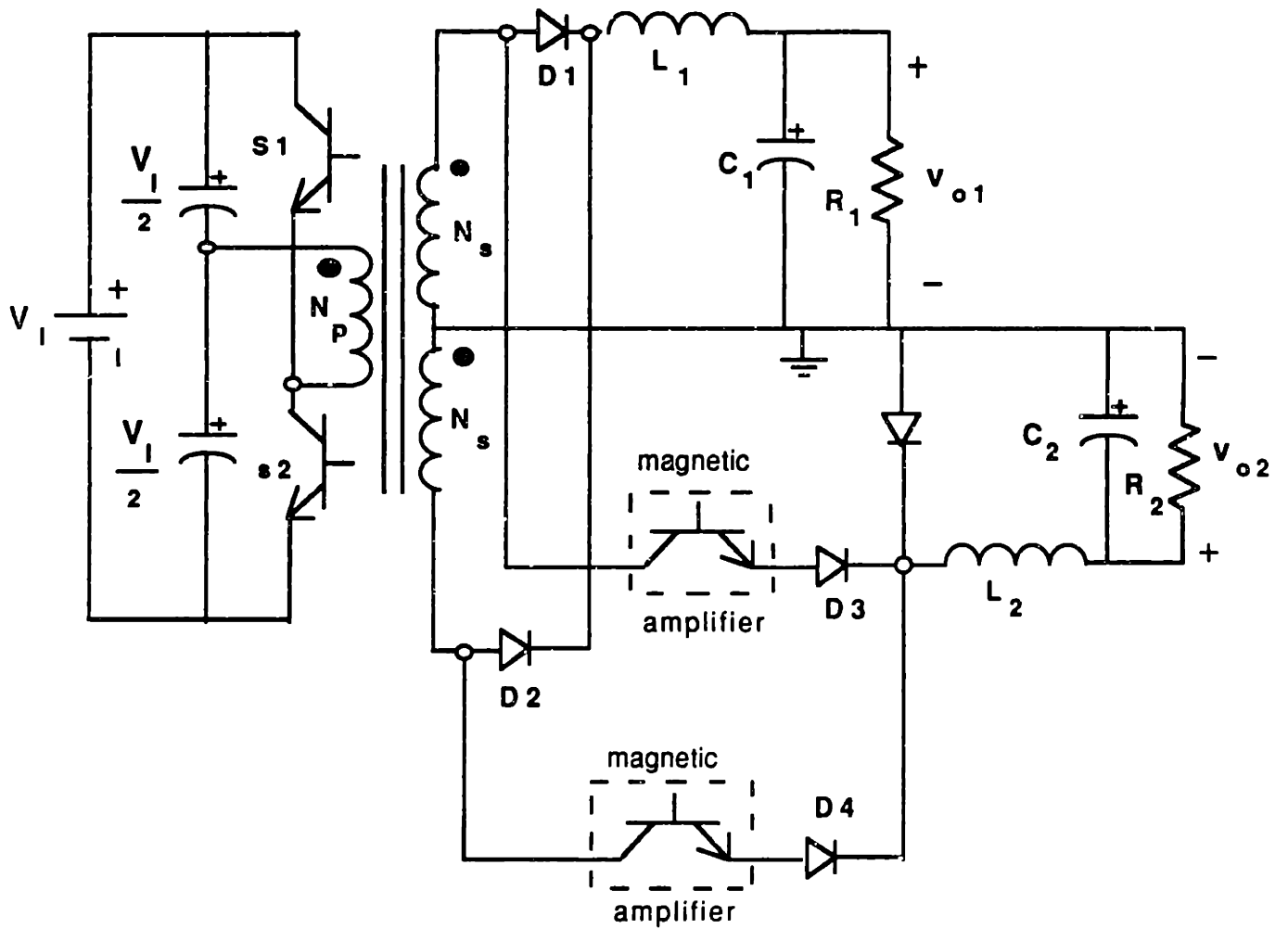
Figure 3.1: Two output half-bridge voltage converter with magnetic amplifier on second output
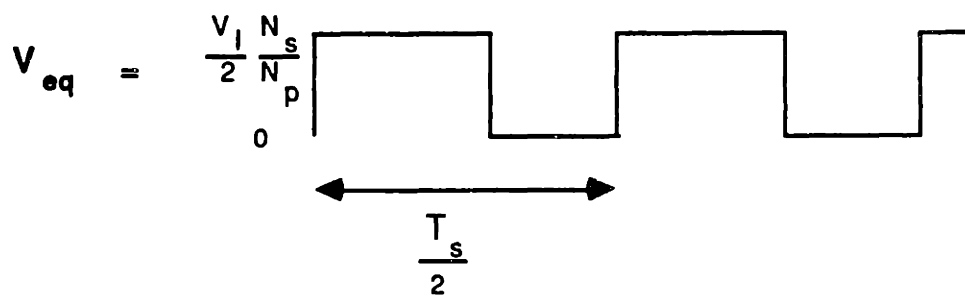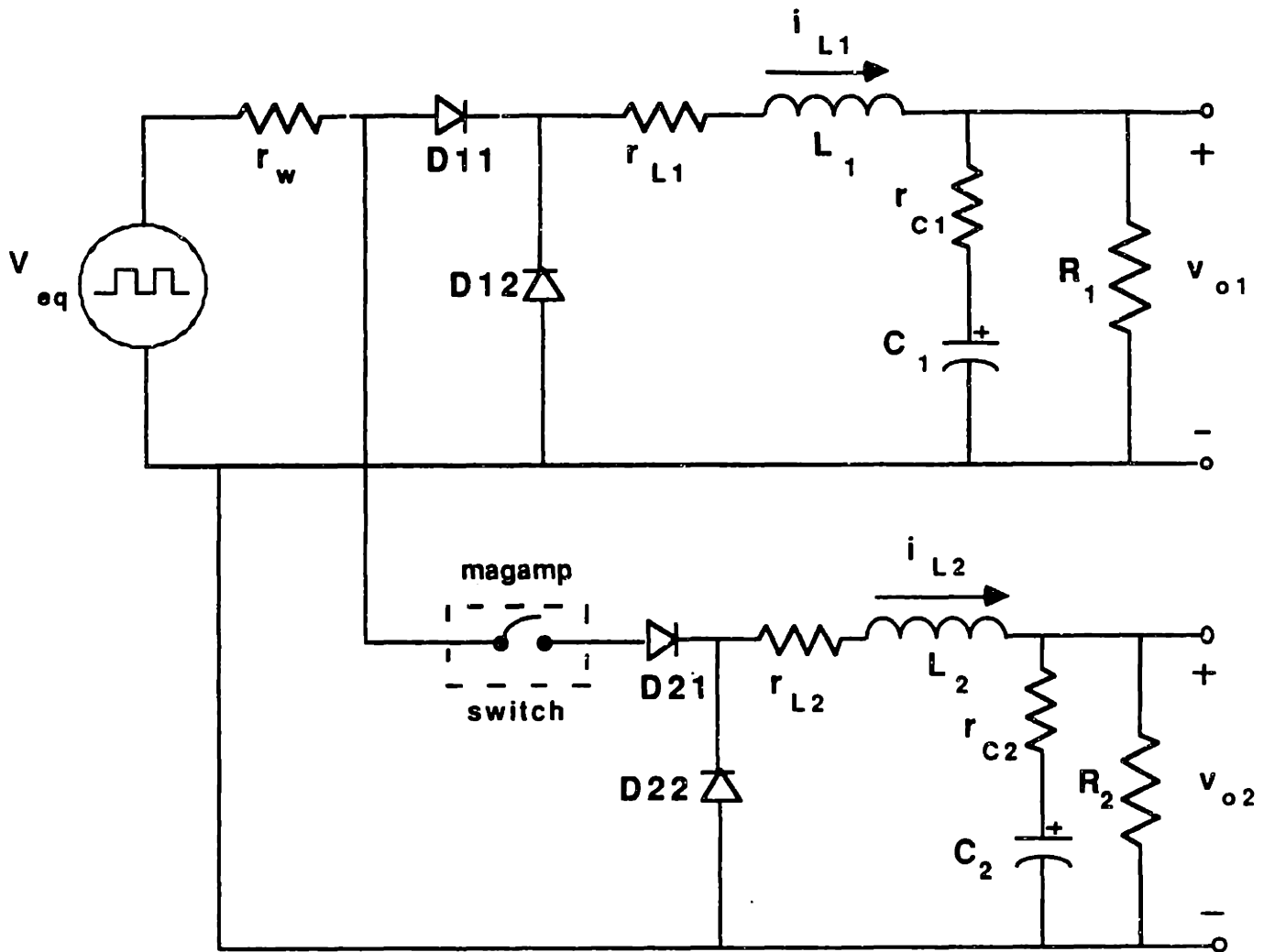
Figure 3.2: Half-bridge equivalent circuit (simplified)

52

N_p - Number of turns of the primary winding.

N_s - Number of turns of each secondary winding.

V_I - DC input voltage (primary).

V_{eq} - Equivalent input voltage (secondary).

r_w - Combined (primary and secondary) winding resistance.

R_1 - Load resistance of the first output.

R_2 - Load resistance of the second output.

C_1 - Capacitance of the first output.

C_2 - Capacitance of the second output.

r_{c1} - Equivalent series resistance of C_1.

r_{c2} - Equivalent series resistance of C_2.

L_1 - Inductor of the first output.

L_2 - Inductor of the second output.

r_{L1} - Series resistance of L_1.

r_{L2} - Series resistance of L_2.

r_d - Diode drop resistance.

V_d - Diode drop voltage (when conducting).

T_s - Primary switches period.

T - Equivalent switching period ($T_s/2$).

It should be pointed out that important practical considerations or nonidealities not explicitly shown in Fig. 3.1 (e.g. capacitor ESR, transformer winding resistance, etc.) are included in Fig. 3.2 for modeling purposes. In summary, the modeling assumptions embedded in Fig. 3.2 are:

1. The effects of capacitor equivalent series resistance are not negligible (ESR included).

2. Diode and transistor drops, when conducting, are included.

3. The transformer has ideal magnetic characteristics and there exists no leakage flux among its windings.

4. The converter operates in continuous conduction mode.

5. The magnetic amplifier (magamp) is modeled as an ideal switch which can be controlled to turn on at a later specified fraction of the switching period (T) after
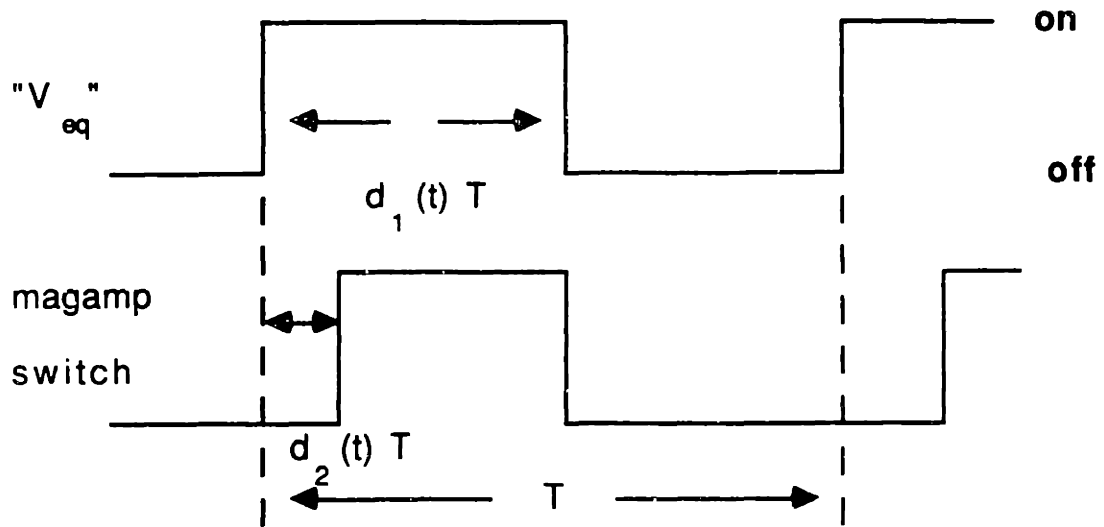
Figure 3.3: Timing diagram of control signals

STATES	V_{eq}	magamp
1	on	off
2	on	on
3	off	off

Table 3.1: State combinations for the half-bridge converter.

V_{eq} goes high. Nonlinearities associated with the magnetic amplifier will not be considered.

Figure 3.3 shows the timimg diagram of control signals used in modeling the half-bridge converter. The duty ratio $d_1(t)$ is the fraction of the switching period that the voltage V_{eq} is on. The second duty ratio $d_2(t)$ defines the fraction of the switching period that the magamp will remain off after the beginning of a new cycle. The magamp is synchronized to turn off at the same time that V_{eq} goes low. Over one switching period (period of V_{eq}), the half-bridge converter will have the different state configurations presented in Table 3.1.

To obtain the circuit state-space description in each state configuration corresponding to Table 3.1, first define the system state and input vectors to be

$$x(t) = [v_{c1}(t) \ i_{l1}(t) \ v_{c2}(t) \ i_{l2}(t)]^T \qquad (3.1)$$

$$U = [V_I \; V_d]^T \tag{3.2}$$

where

v_{c1} - Capacitor voltage of the first output.

i_{l1} - Inductor current of the first output.

v_{c2} - Capacitor voltage of the second output.

i_{l2} - Inductor current of the second output.

The exact circuit description will be characterized by three linear time invariant (LTI) models corresponding to the three states of Table 3.1. The $i - th$ state equation will be

$$x'(t) = A_i x(t) + B_i U \tag{3.3}$$

During state 1, diodes $D11$ and $D22$ are on while $D12$ and $D21$ are off. Thus, energy only gets delivered to the first load. Applying Kirchhoffs Laws to the circuit in Fig. 3.2 for state 1, the circuit state-space description in this configuration is

$$\frac{d}{dt}\begin{bmatrix} v_{c1}(t) \\ i_{l1}(t) \\ v_{c2}(t) \\ i_{l2}(t) \end{bmatrix} = \begin{bmatrix} -\frac{\rho_1}{C_1 R_1} & \frac{\rho_1}{C_1} & 0 & 0 \\ -\frac{\rho_1}{L_1} & -\frac{(r_w + r_{e1})}{L_1} & 0 & 0 \\ 0 & 0 & -\frac{\rho_2}{C_2 R_2} & \frac{\rho_2}{C_2} \\ 0 & 0 & -\frac{\rho_2}{L_2} & -\frac{r_{e2}}{L_2} \end{bmatrix} \begin{bmatrix} v_{c1}(t) \\ i_{l1}(t) \\ v_{c2}(t) \\ i_{l2}(t) \end{bmatrix} + \begin{bmatrix} 0 & 0 \\ \frac{N_s}{2L_1 N_p} & -\frac{1}{L_1} \\ 0 & 0 \\ 0 & -\frac{1}{L_2} \end{bmatrix} U$$
$$\tag{3.4}$$

or

$$x'(t) = A_1 x(t) + B_1 U \tag{3.5}$$

where

$$\rho_1 = \frac{R_1}{r_{c1} + R_1}$$

$$\rho_2 = \frac{R_2}{r_{c2} + R_2}$$

$$r_{e1} = r_{c1}\rho_1 + r_{L1} + r_d$$

$$r_{e2} = r_{c2}\rho_2 + r_{L2} + r_d$$

During state 2, the magamp switch is assumed to be closed ($D21$ on, $D22$ off) so that power from V_{eq} is also being delivered to the second load. The state equations for this circuit configuration are

$$
\frac{d}{dt}\begin{bmatrix} v_{c1}(t) \\ i_{l1}(t) \\ v_{c2}(t) \\ i_{l2}(t) \end{bmatrix} = \begin{bmatrix} -\frac{\rho_1}{C_1 R_1} & \frac{\rho_1}{C_1} & 0 & 0 \\ -\frac{\rho_1}{L_1} & -\frac{(r_w+r_{e1})}{L_1} & 0 & -\frac{r_w}{L_1} \\ 0 & 0 & -\frac{\rho_2}{C_2 R_2} & \frac{\rho_2}{C_2} \\ 0 & -\frac{r_w}{L_2} & -\frac{\rho_2}{L_2} & -\frac{(r_w+r_{e2})}{L_2} \end{bmatrix} \begin{bmatrix} v_{c1}(t) \\ i_{l1}(t) \\ v_{c2}(t) \\ i_{l2}(t) \end{bmatrix} + \begin{bmatrix} 0 & 0 \\ \frac{N_s}{2L_1 N_p} & -\frac{1}{L_1} \\ 0 & 0 \\ \frac{N_s}{2L_2 N_p} & -\frac{1}{L_2} \end{bmatrix} U
$$

(3.6)

or

$$
x'(t) = A_2 x(t) + B_2 U \tag{3.7}
$$

In the final configuration (state 3), both outputs are isolated and the stored energy in the inductors and capacitors is dissipated by the load. The state space description of this circuit configuration is

$$
\frac{d}{dt}\begin{bmatrix} v_{c1}(t) \\ i_{l1}(t) \\ v_{c2}(t) \\ i_{l2}(t) \end{bmatrix} = \begin{bmatrix} -\frac{\rho_1}{C_1 R_1} & \frac{\rho_1}{C_1} & 0 & 0 \\ -\frac{\rho_1}{L_1} & -\frac{r_{e1}}{L_1} & 0 & 0 \\ 0 & 0 & -\frac{\rho_2}{C_2 R_2} & \frac{\rho_2}{C_2} \\ 0 & 0 & -\frac{\rho_2}{L_2} & -\frac{r_{e2}}{L_2} \end{bmatrix} \begin{bmatrix} v_{c1}(t) \\ i_{l1}(t) \\ v_{c2}(t) \\ i_{l2}(t) \end{bmatrix} + \begin{bmatrix} 0 & 0 \\ 0 & -\frac{1}{L_1} \\ 0 & 0 \\ 0 & -\frac{1}{L_2} \end{bmatrix} U \tag{3.8}
$$

or

$$
x'(t) = A_3 x(t) + B_3 U \tag{3.9}
$$

The system output voltages for each of the configurations can be expressed as

$$
y_1(t) = v_{o1}(t) = [\rho_1 \ r_{c1}\rho_1 \ 0 \ 0]x(t) = C_1 x(t) \tag{3.10}
$$

$$
y_2(t) = v_{o2}(t) = [0 \ 0 \ \rho_2 \ r_{c2}\rho_2]x(t) = C_2 x(t) \tag{3.11}
$$

The output voltages are a linear combination of the states due to the equivalent series resistance (ESR) of the output filter capacitors.

The *exact large signal model* of the half-bridge converter can be obtained, as shown in Section 2.1, by introducing input variables u_1 and u_2, which take on the values 1 or 0 depending on whether V_{eq} and the magamp switch are 'on' or 'off', respectively. Then, the exact large-signal model takes the form

$$x'(t) = [u_2 A_1 + (u_1 - u_2)A_2 + (1 - u_1)A_3]x(t) + \qquad (3.12)$$
$$[u_2 B_1 + (u_1 - u_2)B_2 + (1 - u_1)B_3]U$$
$$y(t) = C x(t) \qquad (3.13)$$

where

$$C = \begin{bmatrix} C_1 \\ C_2 \end{bmatrix}$$

Typical switched waveforms for this converter are shown in Fig. 3.4 and Fig. 3.5. The switching period (T) is $2\mu sec$. These waveforms were obtained by simulating (3.12) with the analysis and control software package $MATRIX_X$, as shown in [5]. Note that the three switch configurations are present. From Figs. 3.4 and 3.5, it can be seen that for well designed converters the state waveforms ripple can be made relatively small. This is one of the main justifications for working with simpler averaged models.

3.2   Averaged Models

Replacing u_1 and u_2 in (3.12) with their respectives one cycle averages $d_1(t)$ and $d_2(t)$, results in the large signal state-space averaged model. As shown in [5], the averaged model curve approximates well the average value of the switched trajectory, and thus can be used as a basis for analysis and control design. The envelope or average value of the waveform is what needs to be controlled, not the exact trajectories of the state variables. Figure 3.7 shows average open loop responses of the output voltages to a large increase in load resistance for a typical half-bridge converter (parameter values shown below). These plots represent the average values of the actual output voltage

57
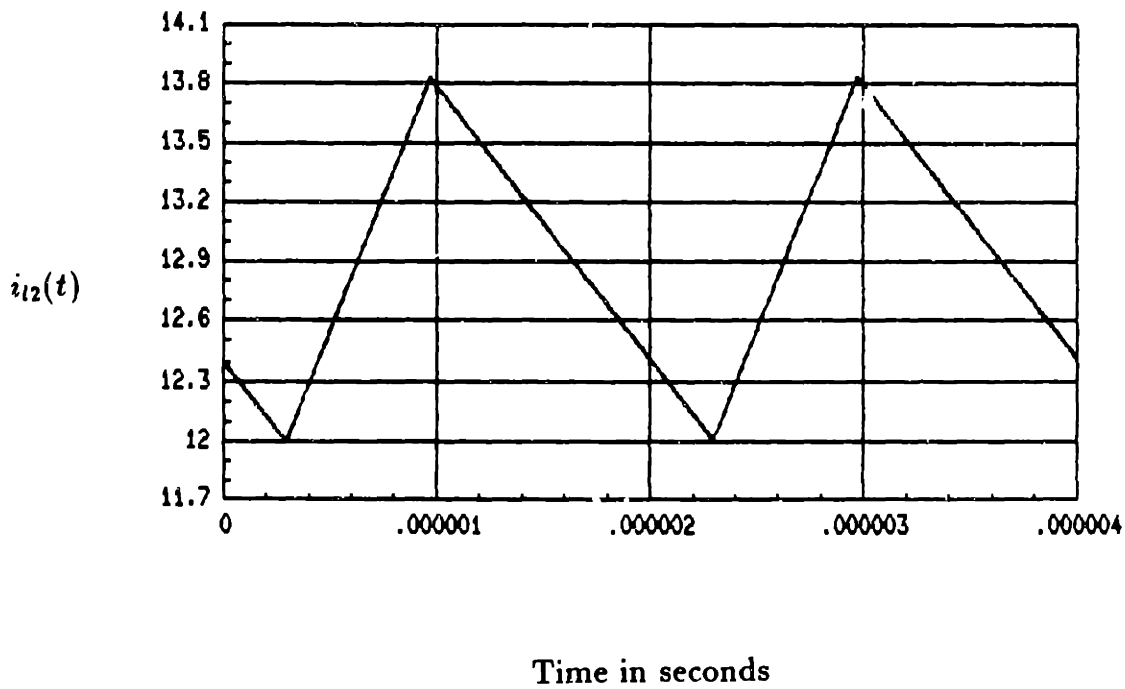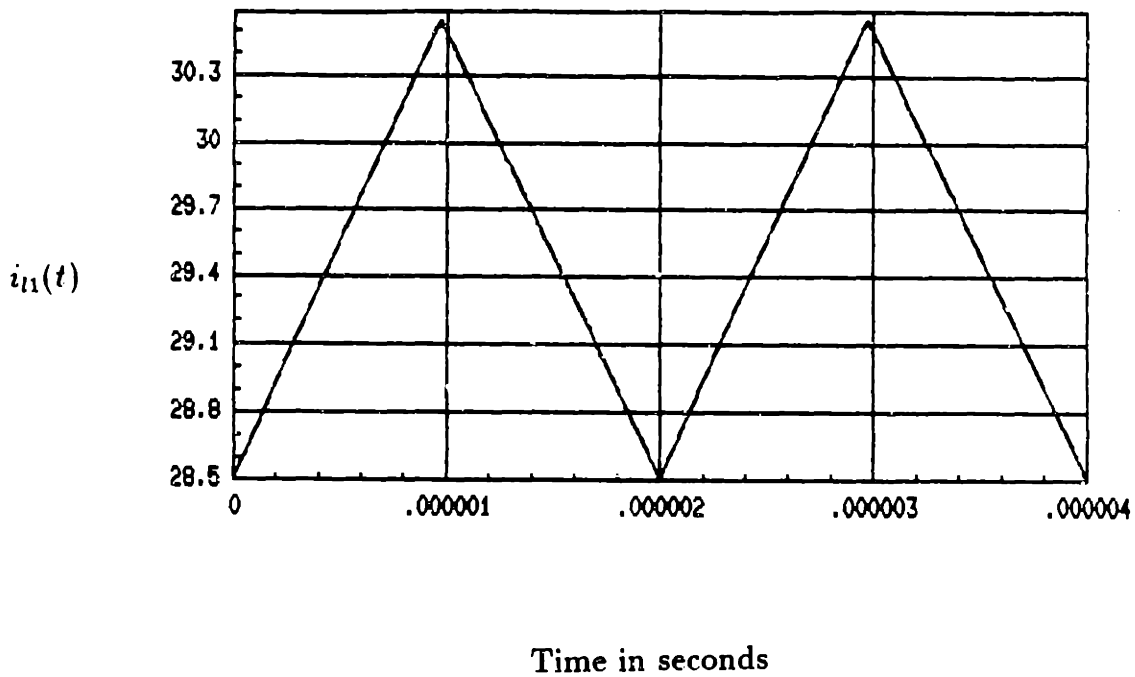
Figure 3.4: Typical inductor current waveforms of the half-bridge converter.

Time in seconds

Time in seconds
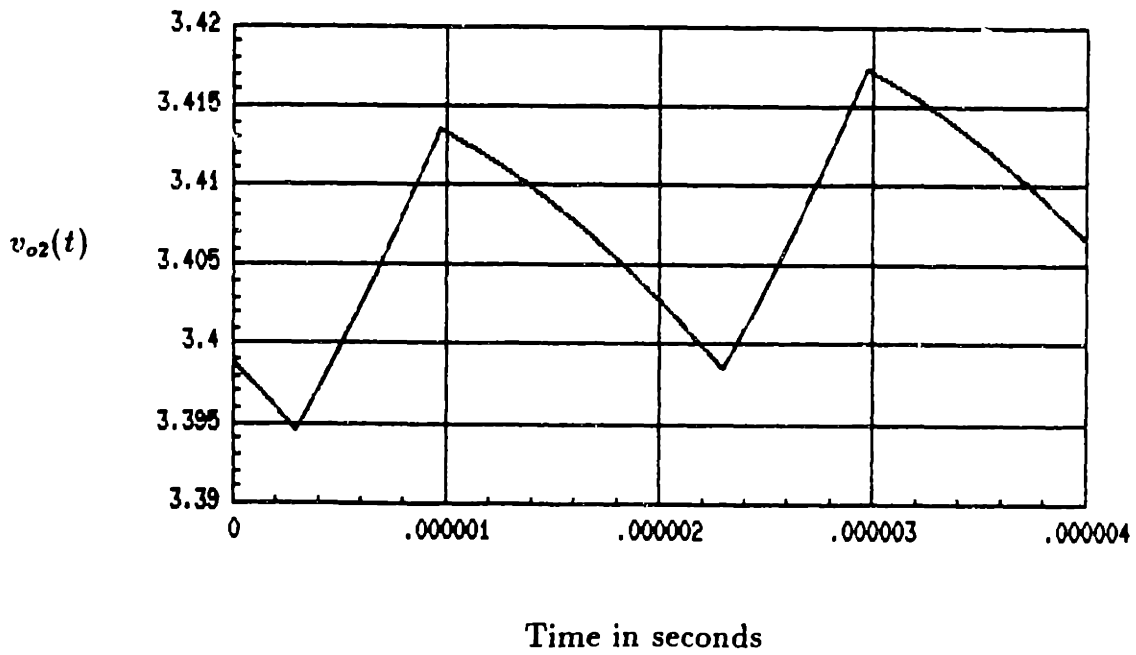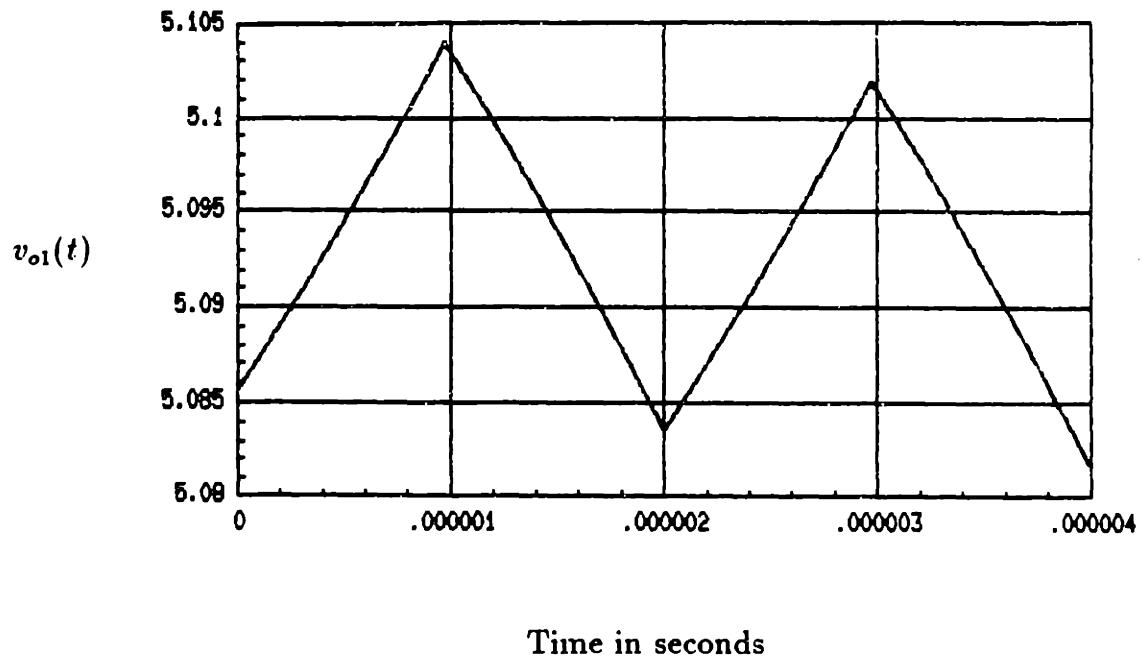
Figure 3.5: Typical output voltage waveforms of the half-bridge converter.
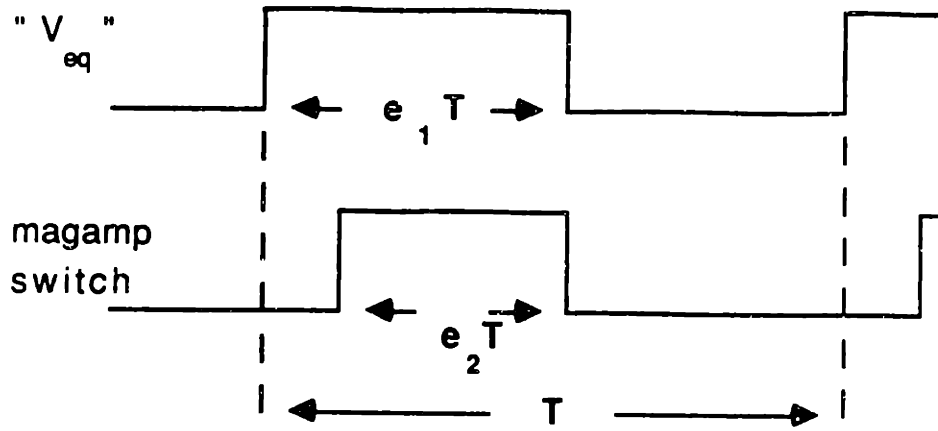
Figure 3.6: Definition of the duty ratio $e_2(t)$.

waveforms. The nominal parameters values of the half-bridge converter which will be studied in this work are

$$
\begin{aligned}
N_p : N_s &= 12 : 1 \\
V_I &= 300 \\
r_w &= 5.8 m\Omega \\
R_1 &= 0.17\Omega \\
R_2 &= 0.272\Omega \\
C_1 &= 400\mu F \\
C_2 &= 200\mu F \\
r_{c1} &= 10 m\Omega \\
r_{c2} &= 10 m\Omega \\
L_1 &= 3\mu H \\
L_2 &= 3\mu H \\
r_{L1} &= 1 m\Omega \\
r_{L2} &= 1 m\Omega \\
r_d &= 7.5 m\Omega \\
V_d &= 0.6 V \\
T &= 2\mu sec
\end{aligned}
$$

The control inputs to the large signal averaged model are the duty ratios $d_1(t)$ and $d_2(t)$. In order to greatly simplify the analysis and control design of this system, the control inputs will be transformed or redefined as done in [5] for a forward converter topology. In [5], it was shown that by defining the new set of input variables to be

$$e_1(t) = d_1(t) \tag{3.14}$$
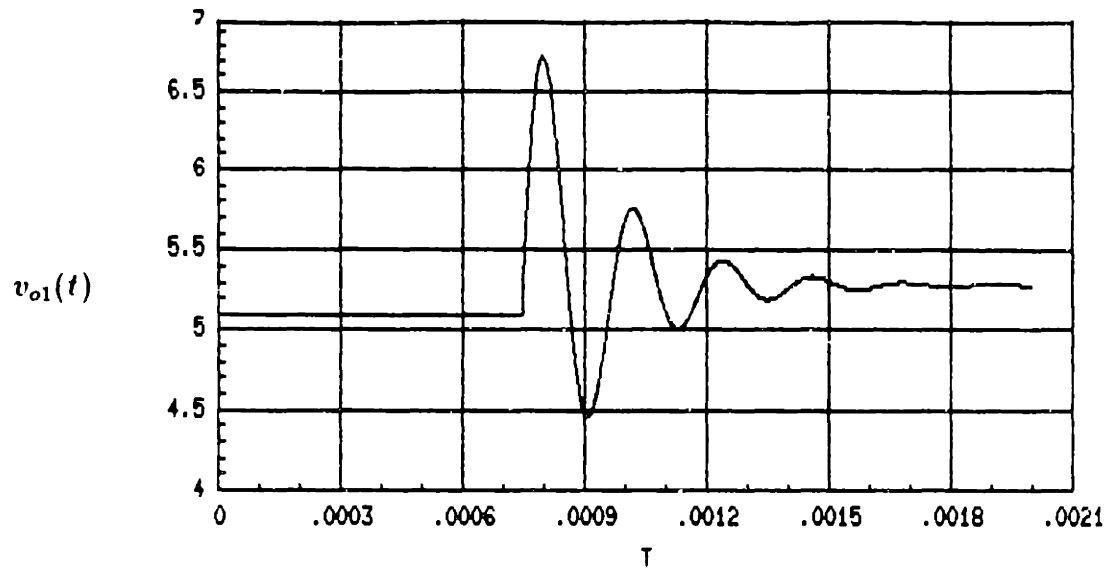
Time in seconds
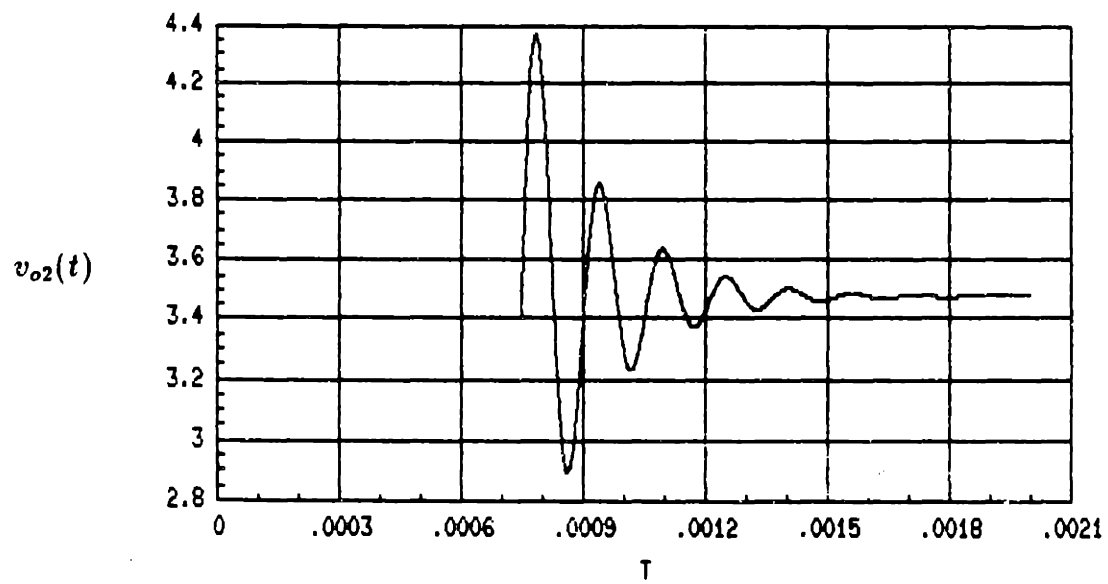
Time in seconds

Figure 3.7: Open-loop average output voltage transient responses to a large step increase in load.

and

$$e_2(t) = d_1(t) - d_2(t) \tag{3.15}$$

where the new duty ratio $e_2(t)$ defines the fraction of the switching period in which the magamp switch is on (as shown in Fig. 3.6), the two output systems are effectively decoupled and control design reduces to the control of two (almost) independent single-input, single-output systems. Using these redefined controls, the large signal state space averaged model for the half-bridge converter becomes

$$\frac{d}{dt}\begin{bmatrix} v_{c1}(t) \\ i_{l1}(t) \\ v_{c2}(t) \\ i_{l2}(t) \end{bmatrix} = \begin{bmatrix} -\frac{\rho_1}{C_1 R_1} & \frac{\rho_1}{C_1} & 0 & 0 \\ -\frac{\rho_1}{L_1} & -\frac{(r_w e_1(t)+r_{e1})}{L_1} & 0 & -\frac{r_w e_2(t)}{L_1} \\ 0 & 0 & -\frac{\rho_2}{C_2 R_2} & \frac{\rho_2}{C_2} \\ 0 & -\frac{r_w e_2(t)}{L_2} & -\frac{\rho_2}{L_2} & -\frac{r_w e_2(t)+r_{e2}}{L_2} \end{bmatrix} \begin{bmatrix} v_{c1}(t) \\ i_{l1}(t) \\ v_{c2}(t) \\ i_{l2}(t) \end{bmatrix} \tag{3.16}$$
$$+ \begin{bmatrix} 0 & 0 \\ \frac{N_s V_I}{2N_p L_1} & 0 \\ 0 & 0 \\ 0 & \frac{N_s V_I}{2N_p L_2} \end{bmatrix} \begin{bmatrix} e_1(t) \\ e_2(t) \end{bmatrix} + \begin{bmatrix} 0 \\ -\frac{1}{L_1} \\ 0 \\ -\frac{1}{L_2} \end{bmatrix} V_d$$

where V_d (diode drop voltage) is considered as a deterministic input or disturbance. Note that if the small winding resistance r_w is neglected, the state dynamics of the first output are only influenced by the duty ratio $e_1(t)$ while the dynamics of the second output depend only on $e_2(t)$. Moreover, the large signal state-space representation of the system becomes linear. Since (as corroborated by simulations) the effect of r_w on the exact and averaged behavior of the system is negligible, it is convenient for analysis and control purposes to neglect r_w and model the half-bridge converter as two decoupled systems with control inputs $e_1(t)$ and $e_2(t)$. Then, separating the system results in

$$x_1'(t) = A_1 x_1(t) + F_1 e_1(t) + L_1 V_d \tag{3.17}$$

where

$$x_1(t) = [v_{c1}(t) \; i_{l1}(t)]^T$$

$$A_1 = \begin{bmatrix} -\frac{\rho_1}{C_1 R_1} & \frac{\rho_1}{C_1} \\ -\frac{\rho_1}{L_1} & -\frac{r_{e1}}{L_1} \end{bmatrix}, \quad F_1 = \begin{bmatrix} 0 \\ \frac{N_s V_I}{2N_p L_1} \end{bmatrix}, \quad L_1 = \begin{bmatrix} 0 \\ -\frac{1}{L_1} \end{bmatrix}$$

and

$$x_2'(t) = A_2 x_2(t) + F_2 e_2(t) + L_2 V_d \qquad (3.18)$$

where

$$x_2(t) = [v_{c2}(t)\ i_{l2}(t)]^T$$

$$A_2 = \begin{bmatrix} -\frac{\rho_2}{C_2 R_2} & \frac{\rho_2}{C_2} \\ -\frac{\rho_2}{L_2} & -\frac{r_{s2}}{L_2} \end{bmatrix}, \quad F_2 = \begin{bmatrix} 0 \\ \frac{N_s V_I}{2 N_p L_2} \end{bmatrix}, \quad L_2 = \begin{bmatrix} 0 \\ -\frac{1}{L_2} \end{bmatrix}$$

The output equations for both systems are the same linear combinations of the states given in (3.13). The mathematical description of the half-bridge converter now comprises two single-output converters whose large signal averaged models are given by (3.17) and (3.18). Setting the left side of (3.17) and (3.18) equal to zero gives the steady state average relation for both output units, namely,

$$0 = A_1 x_{1\bullet\bullet} + F_1 E_1 + L_1 V_d \qquad (3.19)$$

$$0 = A_2 x_{2\bullet\bullet} + F_2 E_2 + L_2 V_d,$$

where $x_{i\bullet\bullet}$ $(i = 1, 2)$ is the nominal steady state operating point for each output system with nominal duty ratios

$$E_1 = D_1 \qquad (3.20)$$

$$E_2 = D_1 - D_2$$

Combining (3.19) with the output voltage relation for each system, the required nominal duty ratio needed to achieve a desire nominal operating condition can be found. The desired nominal operating conditions for the half-bridge converter are

1. Output 1: $V_{o1} = 5.1 volts$, $I_{l1} = 30A$.

2. Output 2: $V_{o2} = 3.4 volts$, $I_{l2} = 12.5A$.

For these operating conditions, the required nominal duty ratios can be found to be $E_1 = 0.485$ and $E_2 = 0.148$.

63

It is important to stress at this point that the second output is still not completely decoupled from the first, as can be seen by examining the duty ratio constraints of the decoupled system. The large signal averaged model (3.17),(3.18) has input constraints, obtained from the definition of the new duty ratios and from Figs. 3.3 and 3.6. These are

$$0 \leq e_1(t) \leq 1 \tag{3.21}$$

$$0 \leq e_2(t) \leq e_1(t) \tag{3.22}$$

and for the small signal control inputs

$$- E_1 \leq \delta e_1 \leq 1 - E_1 \tag{3.23}$$

$$- E_2 \leq \delta e_2(t) \leq E_1 - E_2 + \delta e_1(t) \tag{3.24}$$

Thus, the upper bound of the duty ratio input $e_2(t)$ is dependent on $e_1(t)$. As will be seen in Chapter 5, this is an important factor in controller performance.

3.2.1   Small signal analysis

The small signal analysis of the half-bridge converter will be based on the decoupled system (two single-input, single-output systems) with the new redefined controls. For this case, the large signal averaged model is linear. Thus, the *small-signal state space averaged models* for the half-bridge converter are obtained from the large signal model by replacing the vector $x(t)$ by the small signal state vector $\delta x(t)$ and the actual inputs by the duty ratio perturbation input $\delta e(t)$. For the decoupled system, this results in

$$\delta x_1'(t) = A_1 \delta x_1(t) + F_1 \delta e_1(t) \tag{3.25}$$

$$\delta y_1(t) = C_1 \delta x_1(t) \tag{3.26}$$

and

$$\delta x_2'(t) = A_2 \delta x_2(t) + F_2 \delta e_2(t) \tag{3.27}$$

$$\delta y_2(t) = C_2 \delta x_2(t) \tag{3.28}$$

These LTI models allow us to approach the small signal and feedback control design of the two-output half-bridge converter simply in terms of two single-input single output problems. Inserting the numerical parameter values of the half-bridge converter into the above equation yields

$$\delta x_1'(t) = \begin{bmatrix} -13888 & 2361 \\ -314800 & -5981 \end{bmatrix} \delta x_1(t) + \begin{bmatrix} 0 \\ 4166666 \end{bmatrix} \delta e_1(t) \tag{3.29}$$

$$\delta y_1(t) = \delta v_{o1}(t) = [0.9444 \ 0.00944] \delta x_1(t)$$

and

$$\delta x_2'(t) = \begin{bmatrix} -17730 & 4822 \\ -321500 & -6048 \end{bmatrix} \delta x_2(t) + \begin{bmatrix} 0 \\ 4166666 \end{bmatrix} \delta e_2(t) \tag{3.30}$$

$$\delta y_2(t) = \delta v_{o2}(t) = [0.9645 \ 0.00965] \delta x_2(t)$$

The open loop poles for output 1 are

$$-1.0 + j2.7 \ and \ -1.0 - j2.7 \ (\times 10^4) \tag{3.31}$$

and for output 2 are

$$-1.2 + j3.9 \ and \ -1.2 - j3.9 \ (\times 10^4) \tag{3.32}$$

The pole locations show that both open loop systems are highly oscillatory. The natural frequencies for these complex conjugate pole pairs match the frequencies of the oscillations of the initial perturbation transient responses of the respective output units shown in Fig. 3.7. The controllability and observability matrices [20] of each system

have full rank, and therefore both of the single-output converters are controllable and observable. As will be seen in the next chapters, controllability is essential in feedback, state feedback and dynamic compensator control designs. Observability is fundamental in observer, Kalman filter and dynamic feedback compensator design.

The small signal frequency analysis and control of the half-bridge converter will focus on the two transfer functions

$$\frac{v_{o1}(s)}{e_1(s)} = G_1(s) \tag{3.33}$$

and

$$\frac{v_{o2}(s)}{e_2(s)} = G_2(s) \tag{3.34}$$

which numerically are

$$G_1(s) = \frac{39350(s + 2.5 \times 10^5)}{s^2 + 1.99 \times 10^4 s + 8.3 \times 10^8} \tag{3.35}$$

and

$$G_2(s) = \frac{40188(s + 5.0 \times 10^6)}{s^2 + 2.4 \times 10^4 s + 1.7 \times 10^9} \tag{3.36}$$

The zeros in the above transfer functions are introduced by the equivalent series resistances of the output capacitors. The Bode plots for these two systems are shown in Fig. 3.8. The low frequency gain amplifications of these plots reflect the impact that each duty ratio perturbation will have on its respective output voltage. Recall that $T = 2\mu sec$ and so the small signal average results are only presented up to about $w = 1 \times 10^6 \ rad/sec$ or about one-half the switching frequency because, as mentioned in Chapter 2, predictions above that frequency should be discarded. As we will see in the next chapters, this is another modeling assumption which will constrain the bandwith of the compensators to be designed for this converter.
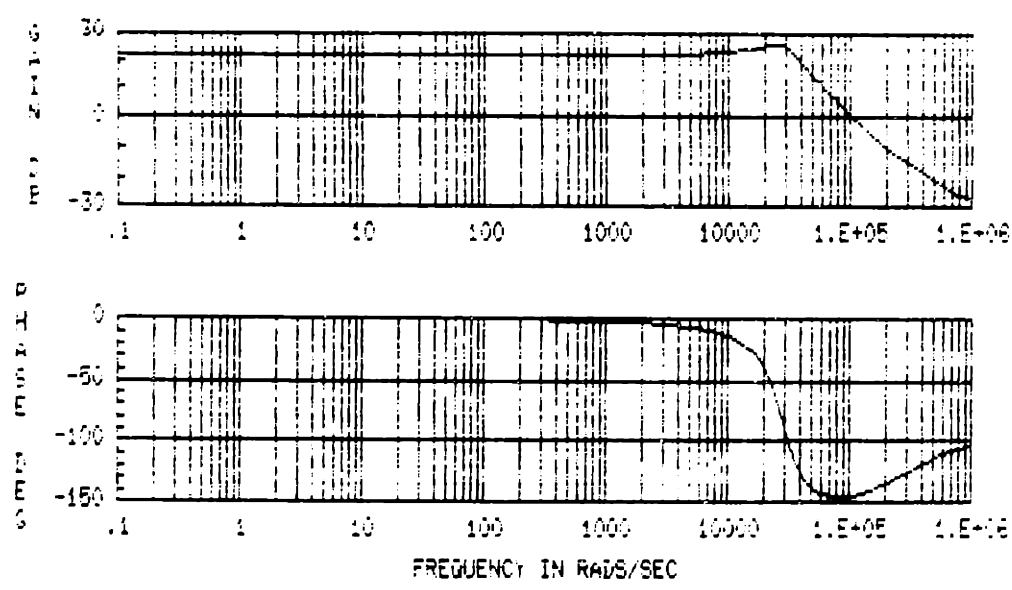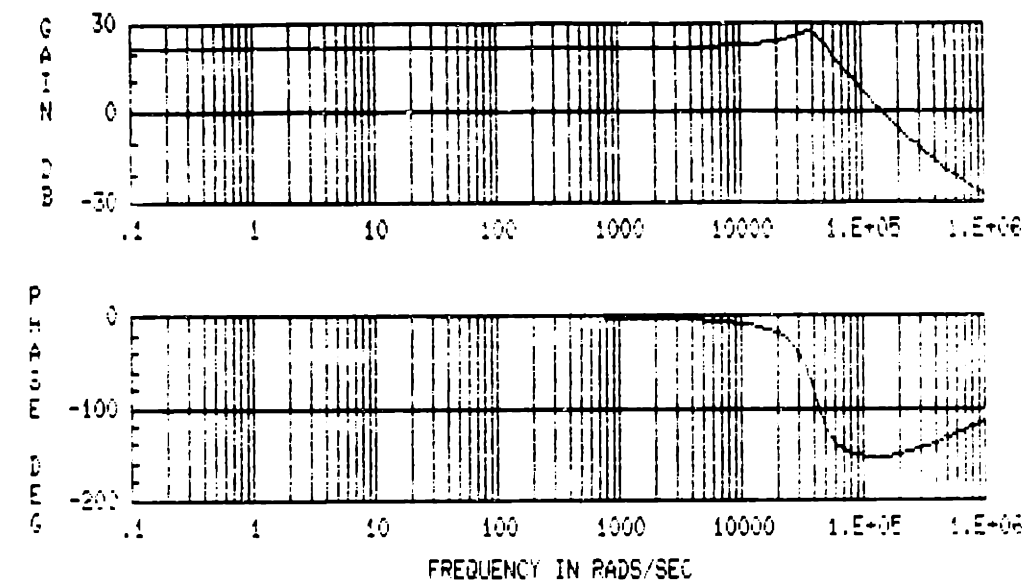
Figure 3.8: Bode plots for $G_1(s)$, top, and for $G_2(s)$, bottom.

3.3 Sampled-Data Models

Although not used for control design and analysis in this thesis work, large and small signal exact sampled-data models were derived for each decoupled half-bridge converter system. The main purpose was to obtain small signal sampled-data models for each output system in order to use these more exact models as a benchmark in the next section, where the stability robustness of the closed loop half-bridge converter will be studied. See [13] for the use of sampled-data models in the design of discrete controllers for switching converters.

As shown in [7,13] and mentioned in Chapter 2, the sampled-data description can be found by piecing together the solutions corresponding to each of the LTI circuit descriptions during one period of operation. This will give us an exact description of the circuit state variables at the end of each cycle or at intervals of T seconds. Neglecting the effects of V_d, the resulting large signal sampled-data models for each of the half-bridge converter output systems ($i = 1, 2$) have the general form

$$x_i(k+1) = A_{si}x_i(k) + B_{si}V_I \qquad (3.37)$$

$$y_i(k+1) = C_i x_i(k+1) \qquad (3.38)$$

where k represents the $k - th$ cycle of operation, and B_{si} depends on the duty ratio $c_i(k)$. Thus, the resulting description is nonlinear. For notational convenience, the matrices A_{si} and B_{si} are presented in Appendix A.

Standard linearization procedures [20] can be applied to (3.37) in order to find the small signal sampled-data model description for this system. Letting $\delta x_i(k)$ and $\delta e_i(k)$ denote perturbations in the sampled state and duty ratio inputs for each output, respectively, and letting $f_i = x_i(k+1)$, the general small signal model is given by

$$\delta x_i(k+1) = \left(\frac{\partial f_i}{\partial x_i(k)}\right)_Q \delta x_i(k) + \left(\frac{\partial f_i}{\partial e_i(k)}\right)_Q \delta e_i(k) \qquad (3.39)$$

$$\delta y_i(k+1) = C_i \delta x_i(k+1) \qquad (3.40)$$

where Q represents evaluation at a nominal operating point (where $e_i(k) = E_i$). The corresponding matrices are also presented in Appendix A. The model (3.39) will be used in the next section to obtain stability robustness boundaries for the closed loop half-bridge converter.

3.4 Stability Robustness of the Closed Loop Half-Bridge Converter

The design of linear feedback controllers for the half-bridge converter will be based on the small signal state space averaged model, which approximates the average value of the nonlinear, switched circuit. Guarantees are needed that controllers based on this nominal plant model will not yield an unstable control system when placed in the actual loop. In general there are many sources of model errors. Besides the averaging approximation, modeling errors of the half-bridge converter can be characterized in terms of structured uncertainty of the power circuit with respect to line and load changes, and parameter variations. The performance requirement that the switching converter must exhibit good output regulation under all anticipated conditions of line and load requires at least that the closed loop control system remain stable under all changes in line and parameters. This stability issue will be termed the stability robustness requirement of the nominal closed loop system.

Since the half-bridge converter is modeled as two single-output switching converters, the following discussion will focus on stability robustness for a single-input single-output system (see [14,15] for extensions of these results for multi-input multi-output plants). Let the small signal model of such a converter be defined as

$$\delta x'(t) = A_n \delta x(t) + F_n \delta e(t) \tag{3.41}$$

$$\delta y(t) = \delta v_o(t) = C_n \delta x(t) \tag{3.42}$$

so the nominal transfer function from the duty ratio to output load voltage is

$$G_n(s) = C_n(sI - A_n)^{-1}F_n = C_n\Phi(s)F_n; \quad \Phi(s) = (sI - A_n)^{-1} \qquad (3.43)$$

Model errors can be reflected at the plant output (or equivalently at the plant input for a single-input single-output system) by writing

$$G_{actual}(s) = L(s)G_n(s) = [1 + P(s)]G_n(s) \qquad (3.44)$$

where $P(s)$ is referred to as the multiplicative error, as illustrated in Figure 3.9. Given these definitions, one can try to quantify all of the power circuit's structured uncertainty in terms of modeling errors of the nominal plant model. An upper bound curve, $P_{max}(w)$, can then be obtained which reflects the worst case modeling errors versus frequency. This frequency curve will play a fundamental role in the control system design.

Consider a controller designed from the nominal plant model $G_n(s)$ and described mathematically by the compensator $K(s)$ shown in Fig. 3.10. One can now define the standard frequency domain descriptions:

1. Nominal loop transfer function: $T(s) = G_n(s)K(s)$.

2. Nominal closed loop transfer function: $C(s) = [1 + T(s)]^{-1}T(s)$.

The actual feedback control system is obtained by replacing $G_n(s)$ in Fig. 3.10 by $G_{actual}(s)$.

A sufficient condition to guarantee that the actual physical system will remain stable if the nominal one is stable is:

$$|C(jw)| < P_{max}^{-1}(w), \quad for\ all\ w. \qquad (3.45)$$

The proof of this result to guarantee stability of the nominal control system design is given in [14,15]. It is evident from (3.45) that the stability robustness requirement
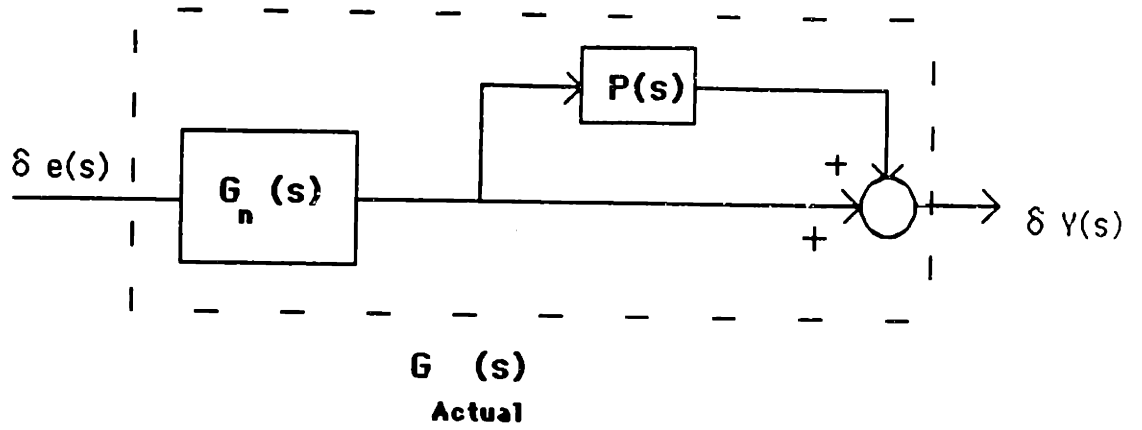
70

Figure 3.9: Structure of the multiplicative error.
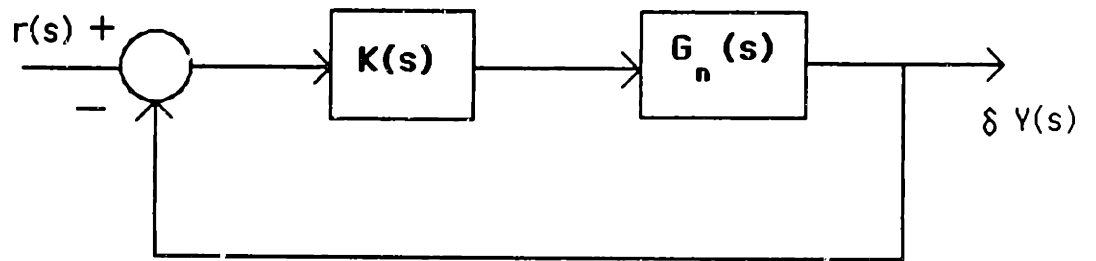
Figure 3.10: Nominal closed loop system with feedforward compensator $K(s)$.

will in general limit the bandwith of the control system based on $G_n(s)$. For switching converter control design based on the averaged model, this may limit the closed loop bandwith more severely than the fact that it must be less than one half the switching frequency.

The types of structured uncertainty of the half-bridge converter to be analyzed are noted below:

1. Resistive load variations, $R_i \to 2R_i$.

2. A $\pm 4\%$ fluctuation of the supply voltage, V_I, from its nominal value.

3. A $\pm 10\%$ fluctuation in the nominal duty ratios, E_i, from its nominal values.

With the above quantities, the model errors can be described in terms of the magnitude of $P(w)$. The above information will lead to having an idea of the worst case magnitude of the modeling error, assuming a phase uncertainty of plus or minus 180 degrees. From (3.44), $P(w)$ is found to be

$$P(w) = \frac{G_{actual}(w)}{G_n(w)} - 1, \; for \; all \; w. \tag{3.46}$$

where $G_{actual}(w)$ is evaluated by making the substitution $z = exp(jwT)$ in the small signal sampled-data model of (3.39).

For both single-output systems of the half-bridge converter, $G_{actual}(w)$ is obtained by selecting values of load resistance R_i, supply voltage V_I, and nominal duty ratios E_i in the range indicated before and substituting these into (3.39). Then the upper bound frequency curves, $P^{-1}(w)$, are calculated from (3.46) and analyzed. From these the stability robustness boundary curves, $P_{max}^{-1}(w)$ of (3.45), are determined as the frequency curves that are most bandwidth limiting. The stability robustness boundary curves of both single-input single-output units describing the half-bridge converter are shown in Fig. 3.11. For both cases, the worst case modeling error versus frequency occurred for load resistance equal to $2R_i$. The results are encouraging since for both

cases $P_{max}^{-1}(w)$ crosses the 0 db line at about one half the switching frequency, so the stability robustness constraints are not bandlimiting in the frequency range of interest. In Chapters 5 and 6, the nominal closed loop control systems bandwiths will be checked to see that they do not cross these boundaries.
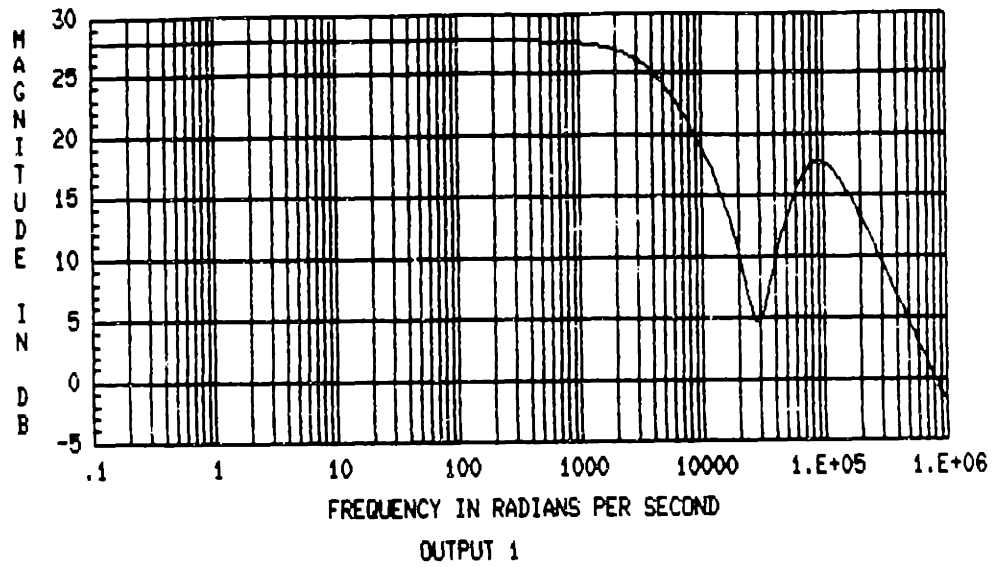
output 1
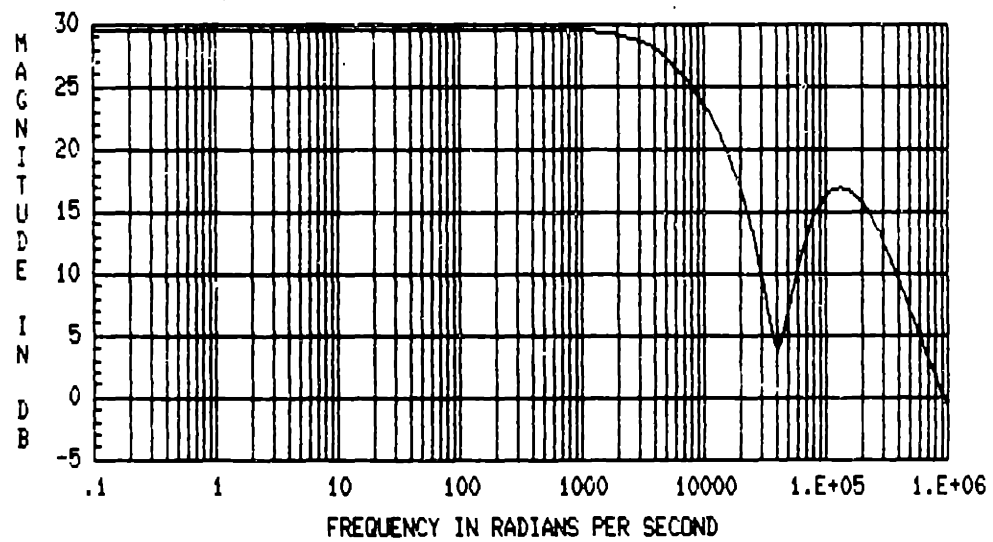
output 2

Figure 3.11: Stability robustness boundaries for each output unit of the half-bridge converter.

Part II

Control

Chapter 4

Control and Estimation System Design

This chapter will focus on a tutorial on certain aspects of modern control and estimation theory. The Linear Quadratic Regulator problem and its closed loop properties are presented. Essentials of observer theory are also included. The results presented here will be applied in the next two chapters to the decoupled half-bridge converter system.

4.1 Current Control Approach for Power Converters

The linearization of the (generally nonlinear) large signal state-space averaged model about an operating point allows the control engineer to take advantage of myriad results from linear control theory. A drawback of this approach is that for large perturbations away from this desired operating point the small signal analysis fails to faithfully predict the system behavior and large signal transients may converge but may be significantly different than those expected from the linear design. This inherent limitation of the small signal analysis has to be taken into account in analysis and control design.

In present practice, state feedback control for power converters is based on classical control theory which utilizes analytical tools such as Bode plots. As in the case of

current mode control, the practice is to close one loop at a time: current loop first, then voltage loop. The voltage loop is closed by choosing a compensation network for an error amplifier such that the closed loop system has a satisfactory frequency characteristics in terms of gain margin and bandwith. Guidelines are given to shape this closed loop Bode plot in a way consistent with design specifications. An example of such a methodology is shown in [19]. The limitations of such an approach become clear when multiple, independently controlled switches are present. For example, the usual practice for this case is to make one of the outputs or switches respond much faster (larger bandwith) than the others in order to independently design the error amplifiers for each of the outputs. Thus, the bandwith of the other outputs are overconstrained.

Modern state-space based control theory methodologies can eliminate some classical control limitations. For example, the Linear Quadratic Regulator to be studied next can offer a very systematic design procedure that has 'built-in' performance and robustness guarantees independent of plant and design parameters. Such guarantees cannot be made for state variable feedback designs that are based upon eigenstructure assignment. Also, modern control concepts and design techniques for single-input single-output systems are easily extendable and applicable to multivariable systems without the neccesity of overly constraining the bandwith of any of the system outputs.

4.2 Linear Quadratic Regulators

The Linear Quadratic Regulator (LQR) formulation and solution are the outcome of a specific mathematical optimization problem. The solution of the problem is due to R.E. Kalman in 1960, although explorations of, for example, the frequency domain properties of the LQR problem continue even today. Note that the following brief introduction to the LQR solution and properties is only intended to expose the necessary facts in order to apply the design methodology to the small-signal state-space averaged models

of high frequency switching converters. Good references on LQR theory are [17,16] and [14].

4.2.1 Problem statement and solution

Let the state dynamics of a multivariable LTI (linear, time-invariant) system be

$$x'(t) = Ax(t) + Bu(t) \qquad (4.1)$$

$$y(t) = Cx(t) \qquad (4.2)$$

with

$$x(t) \in R^n, \ u(t) \in R^m, \ y(t) \in R^p$$

and A, B being constant matrices of appropiate dimensions.

For the LTI Linear Quadratic Regulator problem, the following assumptions will be made

1. All state variables, $x(t)$,can be measured in real time.

2. The system (4.1) is stabilizable. A system is stabilizable if all its unstable modes are controllable, so an controllable system is stabilizable.

3. The system (4.1) is detectable. A system is detectable if all of its unstable modes are observable, so an observable system is detectable.

The optimization problem is formulated as follows. Define a quadratic cost function to be

$$J = \int_0^\infty [x^T(t)Qx(t) + u^T(t)Ru(t)]dt \qquad (4.3)$$

where the constant matrices Q and R are both assumed symmetric and positive definite. Consider the problem of regulating the state vector $x(t)$ about the desired equilibrium

value of zero. The optimization problem is then to find the control $u(t)$, $0 \leq t \leq \infty$, that minimizes the cost J subject to the state dynamic constraints (4.1).

The solution to this special LQR problem turns out to require only constant full state feedback of the system (4.1). The optimal control law is given by

$$u(t) = -Gx(t) \tag{4.4}$$

with the gain matrix G defined as

$$G = R^{-1}B^T K \tag{4.5}$$

where $K = K^T$ is the unique, positive semidefinite solution to the following algebraic Riccati equation (ARE):

$$0 = -KA - A^T K - Q + KBR^{-1}B^T K. \tag{4.6}$$

The proof of this result is non-trivial and requires calculus of variations techniques. For a detailed proof refer to [14].

Equation (4.6) represents a system of coupled quadratic equations for the entries of K, so it is not surprising that in general there are many matrices K that are solutions to the ARE. However, if $[A, B]$ is controllable and $[A, C]$ is observable, then there exists one and only one solution matrix K to the ARE that is positive definite. If the controllability assumption is relaxed to that of stabilizability, and the observability assumption to that of detectability, then there exists one and only one positive semidefinite solution matrix K to the ARE. It should be noted that reliable software exists for solution of (4.6), and the regulator function of $MATRIX_x$ can solve (4.6) efficiently and return the optimal feedback gain matrix G.

4.2.2 Properties of closed loop system

The results of this section are all proved in [14]. All of the following LQR design properties hinge upon the full state feedback assumption and the specific way the control

79
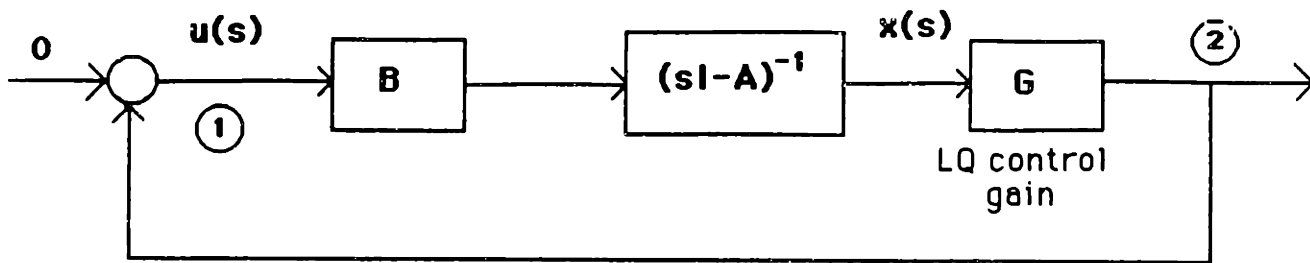
Figure 4.1: The LQR feedback loop.

gain matrix G is computed, namely via the solution of the ARE. It is stressed that these properties hold for any order system with any number of controls and outputs. They also hold for any A, B, C (modulo the stabilizability and detectability assumptions) and any symmetric positive definite matrices R and Q. Thus, the open loop-system may have unstable open-loop poles and nonminimun phase (right-half plane) zeros.

Substituting (4.5) into the open loop dynamic state equations (4.1), the LQR closed loop system is found to be

$$
\begin{aligned}
x'(t) &= [A - BG]\, x(t) & (4.7) \\
y(t) &= C x(t) &
\end{aligned}
$$

The guaranteed properties of the above system are:

- Guaranteed stability of the LQR closed loop system. The poles of the system (4.7) are strictly in the left half of the $s - plane$.

- The LQR control law (4.5) generates the minimun possible value of the quadratic cost function J given by (4.3).

- Excellent robustness properties. The LQR loop transfer function matrix is de-

80

fined mathematically by $G_{LQ}(S) = G(sI - A)^{-1}B$ as seen from Fig. 4.1. The LQR closed-loop transfer function, defined as $C_{LQ}(s) = [I + G_{LQ}(s)]^{-1}G_{LQ}(s)$, is guaranteed to be minimum phase (no zeros in right half plane). If the LQR design parameter matrix R is assumed to be diagonal with equal entries on the diagonal, then certain LQR robustness properties are guaranteed.

1. The maximum singular values of the sensitivity transfer function matrix $S_{LQ}(jw) = (I + G_{LQ}(jw))^{-1}$, which is defined as the transfer function relation from an input disturbance at point 1 to point 2 in Fig. 4.1, are always less than 1(0dB).

2. The upward gain margin of the loop is infinite.

3. The downward gain margin is at least 1/2 or $-6dB$.

4. The phase margin is at least plus or minus 60 degrees.

The gain and phase margins above can occur simultaneously and independently in all m control channels. For single-input single-output systems the matrix R is now a scalar parameter r, the LQ control gain is simply the vector $g = (1/r)B^T K$, and the inherent robustness properties of the LQR design are visualized in terms of the transfer function $g^T(sI - A)^{-1}B$.

All of the above performance and robustness guarantees rely on the assumption that all of the state variables are available for measurement. When this is not the case, state estimators or observers can be used to obtain an estimate of the unavailable state variables. The next section presents essentials of observer theory, following [24].

4.3   Linear Estimator/Observer Theory

Consider a system modeled by the state-space description

$$x'(t) = Ax(t) + Bu(t) + Ln(t) \qquad (4.8)$$

where $x(t)$ is an n-dimensional state vector, $x'(t)$ is its component-wise derivative, $u(t)$ is an m-dimensional vector of known inputs, and $n(t)$ is a vector of unknown inputs representing external disturbances and parameter uncertainties. Suppose the measured outputs of the system are modeled by

$$y(t) = Cx(t) + \theta(t) \tag{4.9}$$

where $\theta(t)$ represents sensor noise.

Observer theory is aimed at providing a real-time estimate $\hat{x}(t)$ of the state $x(t)$ in the above model, using only the known signals $u(t)$ and $y(t)$. A straightforward approach to providing a state estimate for the model (4.8) when $d(t)$ is unknown is via a real-time simulation of (4.8) that ignores the term $Ln(t)$, namely

$$\hat{x}'(t) = A\hat{x}(t) + Bu(t). \tag{4.10}$$

However, an observer for the system modeled by (4.8) and (4.9) goes one step further, in that one corrects the above real-time simulation by use of the discrepancy between the actual outputs $y(t)$ of the system and the prediction $C\hat{x}(t)$ of these outputs that is obtained by ignoring the term $\theta(t)$ in (4.9). This results in the system of equations

$$\hat{x}'(t) = \underbrace{A\hat{x}(t) + Bu(t)}_{simulation} + \underbrace{H[y(t) - C\hat{x}(t)]}_{measurement\ feedback} \tag{4.11}$$

The term in brackets is called the prediction error, and the matrix H is termed the observer gain. When $H = 0$, one recovers the simple real-time simulation of (4.10). Given $u(t)$ and $y(t)$, the system (4.11) can be solved by integrating forward in real time from some specified initial condition. In the context of switching converters, observers will be used to estimate the small signal state vector.

The effectiveness of the observer is assessed by examining the dynamics of the estimation error

$$e(t) = \hat{x}(t) - x(t). \tag{4.12}$$

By letting $n(t) = 0$, it can be easily seen from (4.8),(4.9), and (4.11) that

$$e'(t) = (A - HC)e(t) \tag{4.13}$$

The behavior of (4.13) is thus governed by the eigenvalues of $A - HC$. If we set $H = 0$, the real time simulation is not corrected by a prediction error term and the error dynamics are governed by the eigenvalues of the matrix A. For a sluggish or unstable system this is unacceptable since the estimate $\hat{x}(t)$ will then converge only sluggishly or not at all to $x(t)$. We might expect that the error dynamics can be modified to obtain faster convergence of the estimate if we appropiately pick some nonzero observer gain H. It turns out–see [20]–that if the pair $[A, C]$ is observable, an appropiate choice of H can place the eigenvalues of $A - HC$ arbitrarily (subject only to the requirement that complex eigenvalues are specified in complex conjugate pairs). The error dynamics can therefore, in principle, be modified arbitrarily from that of the simple real-time simulator.

A fast observer would require large values of the entries of H, and these large values would in turn accentuate the disturbance effects. Thus, one would not attempt in practice to make the observer overly fast. The primary objective of observer design often shifts altogether to that of obtaining estimates that are less sensitive to disturbances/uncertainties, rather than obtaining estimates that converge fast. For example, the most familiar version of the celebrated Kalman filter is precisely an observer in which the gain H is chosen to give minimun mean square estimation error when $n(t)$ and $\theta(t)$ are modeled as white Gaussian noise processes. The Kalman filter gain matrix can be found off-line by solving an algebraic Riccati equation similar to (4.6) and all Kalman filter properties are mathematically dual to those established for the Linear Quadratic Regulator (LQR) problem (see [14,17]).

The results in this work focus entirely on obtaining fast small-signal state estimates for switching converters so that state observer based feedback controllers can be obtained, as will be shown in Chapter 6. Since they will be based on averaged models,

the main constraint in the design of these observers is that their error dynamics should not be made faster than one half of the switching frequency.

The observers discussed above are also called *full order* observers because they attempt to estimate all of the state variables. A *full order* observer in the case of power converters would attempt to estimate, for example, i_L (inductor current) and v_c (capacitor voltage), because it is both of these variables that together make up the state variables in the model of our system. As shown in [20], *reduced order* observers of order $n - p$, where n and p are the number of state variables and outputs, respectively, can be designed by a suitable coordinate transformation. Although the price one usually pays with the resulting reduced observer is a stronger sensitivity of the estimates to noise in the unfiltered variables, there are two main issues that motivate the study of reduced observers for switching converters. First, in constructing an estimate for the capacitor voltage state (v_c) the capacitor ESR enters in the model and this value is usually only known with a certain degree of uncertainty anyway. Second, as we will see in Chapter 6, reduced order observers that only attempt to estimate the inductor current result in reduced order feedback compensator networks which will reduce the complexity and cost in implementation.

4.3.1 Observer-based compensation

There is an important result in systems theory which permits one to separate the problem of observer design from that of control design. This result is known (see [21]) as the *eigenvalue separation theorem*.

Specifically, assume that the system (4.1) is both controllable and observable and that a feedback control law is first designed under the assumption that the entire state is available for direct measurement. This corresponds to setting $u(t) = Kx(t)$, resulting in the closed loop system

$$x'(t) = (A + BK)x(t). \tag{4.14}$$

The characteristic polynomial of $A + BK$ can be selected arbitrarily and using the optimal LQR control law presented before, $K = -G$ with G as given in (4.5). Next, assume that an observer (either full or reduced order) is designed to obtain an approximation $\hat{x}(t)$ of the state $x(t)$. Finally, if the two designs are combined by setting the control input equal to $u(t) = K\hat{x}(t)$, that is, using the observer generated state in place of the actual state as shown in Fig. 4.2, it can be shown that the characteristic polynomial of the composite system is the product of the characteristic polynomial of the feedback system matrix $A + BK$ and the characteristic polynomial of the observer. Consequently, the design of state feedback and the design of a state estimator can be carried out independently, and the eigenvalues of the entire system are the union of those of state feedback and those of state estimator. A simple and reasonable guideline to achieve a tradeoff between speed and performance is to choose the observer poles two or three times faster than the eigenvalues of $A + BK$.

In the next chapter LQ full state feedback controllers will be presented and analyzed for the half-bridge converter illustrated in Chapter 3. Next, in Chapter 6, reduced order observer-based feedback compensators designs will be presented for this converter and comparisons will be made. These designs will be based on the two decoupled small signal averaged models for the half-bridge converter.
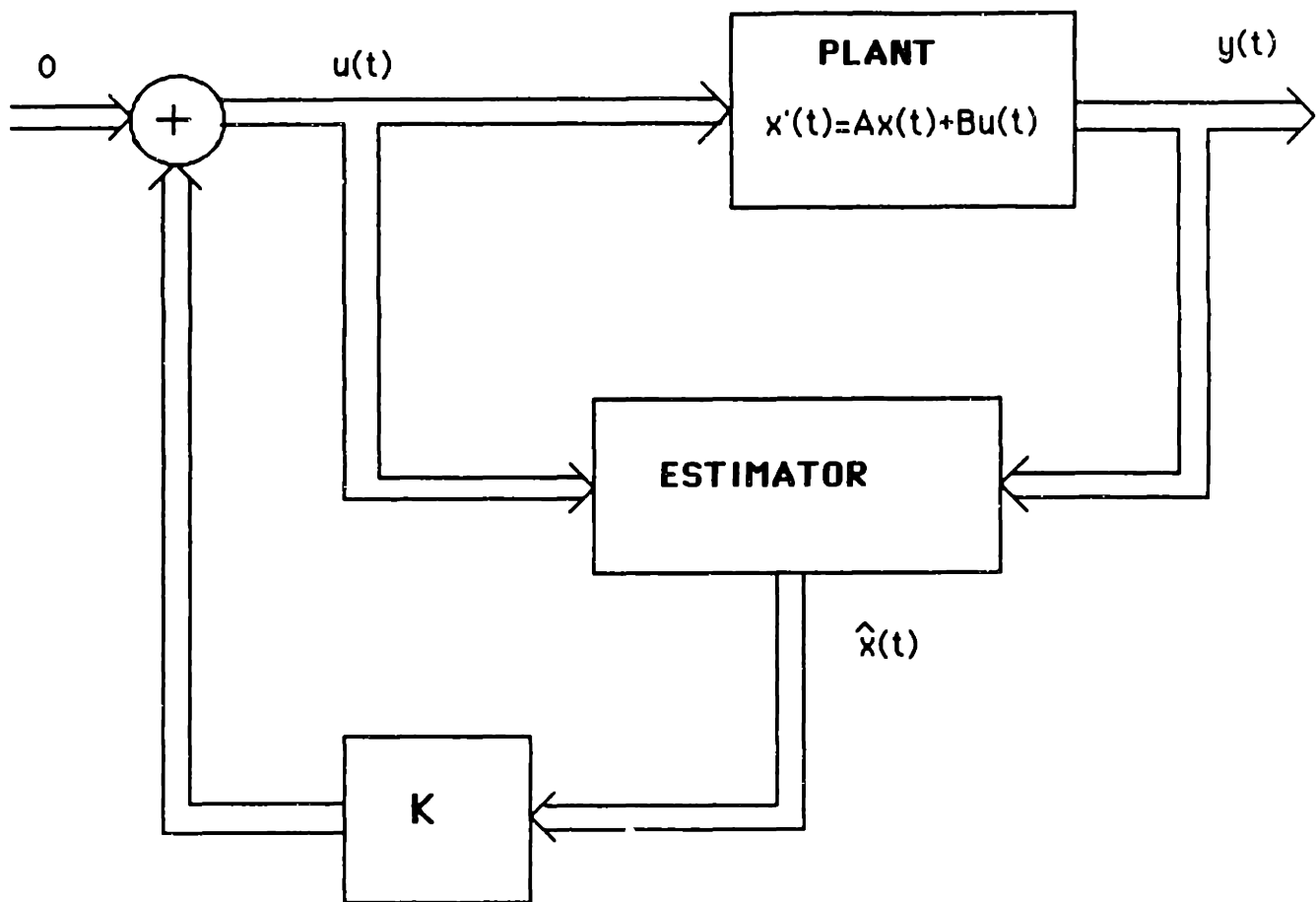
Figure 4.2: Feedback from the estimated state.

Chapter 5

Linear Quadratic Regulator Control of Half-Bridge Converter

In this chapter, the Linear Quadratic Regulator (LQR) state feedback design procedure discussed in the last chapter will be applied to the half-bridge converter presented in Chapter 3. Both time and frequency domain analysis of the resulting closed loop system will be performed.

5.1 Closed Loop Analysis of Half-Bridge Converter

The half-bridge converter circuit is shown in Fig. 3.1. It is an example of a switching power supply that can provide two regulated and isolated DC voltages to an external electronic system. The circuit operation requires a closed-loop control to provide robust, independent regulation of each output unit.

The performance of the resultant closed-loop circuit is evaluated through $MATRIX_x$ simulations using the large signal averaged model for the half-bridge converter. The tests to be performed pulse the output load current by an appropiate amount for several milliseconds to see the effects on the voltage regulation. The reason for picking these tests is that they are typical of those used to test such converters and they are consistent with the typical operation of this converter. Table 5.1 summarizes the two

Test	Output 1 conditions	Output 2 conditions	Δi_{o1}	Δi_{o2}
1	5.1V at 30A	3.4V at 12.5A	+10 A	0
2	5.1V at 30A	3.4V at 12.5A	0	+3 A

Table 5.1: Summary of half-bridge converter performance tests.

tests that have been used to evaluate LQR designs for the half-bridge converter. The output currents, represented by Δi_{oi} in Table 5.1, are not pulsed simultaneously and it is assumed that both output units are operating in steady state at the time of these steps.

The LQR feedback controller designs will be obtained from the two decoupled small-signal averaged models for the half-bridge converter obtained in Chapter 3. Although this input decoupling introduced before is a good modeling and control assumption, the actual system is still not completely decoupled because of transformer nonidealities, control variable constraints, etc. Thus, the resulting closed-loop system has to be carefully examined. In the output voltage transients that result from the tests of Table 5.1, the following closed-loop performance specifications will be evaluated:

1. Stability of the power supply under the operating conditions of Table 5.1.

2. Maximum peak overshoot of 2% from the steady state average voltages.

3. Maximum settling time of two milliseconds.

4. Zero steady state error under all operating conditions.

5. Insensitivity of the voltage regulation in one output during disturbance in other output.

6. The final closed loop bandwidth of each output unit must meet requirements posed by the validity of the small signal models and that of the stability robustness boundaries obtained in Chapter 3.

5.2 LQR Design for Half-Bridge Converter

5.2.1 LQR design formulation

The LQR systematic design approach for the half-bridge converter was performed by using the general guidelines described in [5]. Key aspects of the procedure described there will be repeated here for convenience and completion.

First, the small-signal plant dynamics for each of the two decoupled outputs of the converter are augmented to include an integrator in the forward path of the output voltage in order to provide integral control and achieve the zero steady-state error requirement that has been specified. Then, the resulting (augmented) small-signal model for each unit of the half-bridge converter ($i = 1, 2$) takes the form

$$\delta x'_{ai}(t) = A_{ai}\delta x_{ai}(t) + B_{ai}\delta e_i(t) \qquad (5.1)$$

$$\delta y_i(t) = C_{ai}\delta x_{ai}(t) \qquad (5.2)$$

with

$$\delta x_{ai}(t) = [\delta z_i(t)\ \delta v_{ci}(t)\ \delta i_{li}(t)]^T$$

$$A_{ai} = \begin{bmatrix} 0 & C_i \\ 0 & A_i \end{bmatrix}, \ B_{ai} = \begin{bmatrix} 0 \\ F_i \end{bmatrix}, \ C_{ai} = [0\ C_i]$$

where $\delta z_i(t)$ is the integral of the output voltage perturbation and A_i, F_i, and C_i are given by (3.25) and (3.27). The augmented models for each single-input single-output system with the parameters of Chapter 3 were verified to be controllable.

The proposed small signal LQ regulator block diagram is shown in Fig. 5.1. The regulator design will assume feedback of δx_{ai} to simplify the design process, but in the actual implementation the output voltage is sensed instead of δv_{ci} and fed back through the capacitor voltage gain, as shown in Fig. 5.1. The simulations results presented later show that the ESR is not large enough to cause this to introduce a noticeable error. The augmented plant model for each output unit will be used in conjunction
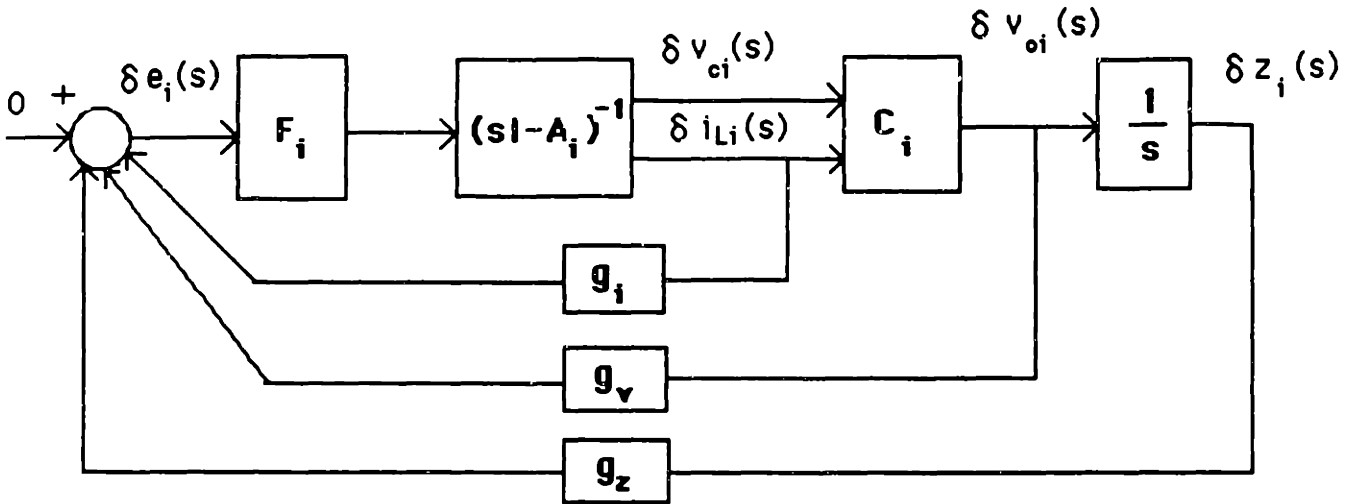
89

Figure 5.1: Linear Quadratic Regulator block diagram.

with the quadratic cost

$$J = \int_0^\infty [\delta x_a^T(t)Q\delta x_a(t) + r\delta e^2(t)]dt \tag{5.3}$$

in order to obtain a state feedback controller. (The subscript i has been dropped for notational simplicity.) Using the general results presented in Chapter 4, the LQR feedback law is

$$\delta e(t) = -[g_z \ g_v \ g_i]\delta x_a(t) = -G\delta x_a(t) \tag{5.4}$$

$$G = \frac{1}{r}B_a^T K \tag{5.5}$$

where K is the solution to the following algebraic Ricatti equation

$$0 = -KA_a - A_a^T K - Q + \frac{1}{r}KB_aB_a^T K \tag{5.6}$$

The LQR design parameters are the constant state weighting matrix Q and scalar control weighting constant r. For simplicity, Q was chosen to be diagonal, so each of its diagonal elements will correspond to penalizing the deviation of a state variable from its nominal operating value. The output voltage and its error integral are clearly the states to be penalized most for deviations from steady state values. Their respective

90

weighting should be picked orders of magnitude higher than the rest of the states (e.g. inductor currents). If zero steady state error is required to coincide with the settling time of the output voltage transient, then the integral weight must be very large, even with respect to the output voltage weight. Once r is fixed, more weighting on states will typically result in smaller maximum perturbations of the state and faster transients, but with a corresponding increase in the bandwidth and the need for larger duty ratio variations (i.e. control effort). Alternatively, control weighting, r, can be used to tune the bandwidth of the closed loop system. Small control weighting results in high gain, high bandwidth designs, while large values of r yield low gain, low bandwidth solutions.

There are limiting factors to this approach, such as the stability robustness boundaries constraint or excessive duty ratio perturbations (input saturation) that will degrade performance. Thus, as with any control system design methodology, iteration is needed until the closed loop specifications are met, while, at the same time, the model validity and constraints are not violated.

In order to obtain a satisfactory LQR design for the half-bridge converter, the following criteria must be satisfied simultaneously:

1. The closed-loop performance specifications for the tests given in Section 5.1 must be satisfied.

2. The closed loop poles (eigenvalues of $A_a - B_a G$ for each output system) must be well below one half the switching frequency (or else state-space averaged models have no meaning).

3. The disturbance rejection response, measured in terms of the sensitivity transfer function $S_{LQ}(s) = [1 + G_{LQ}(s)]^{-1}$, where $G_{LQ}(s) = G(sI - A_a)^{-1}B_a$, should give high attenuation at low frequencies.

4. The stability robustness boundaries obtained in Chapter 3 should not be crossed by the nominal closed loop transfer function $C_{LQ}(s) = [1 + G_{LQ}(s)]^{-1}G_{LQ}(s)$.

5. The required duty ratio perturbation for each transient test must not be excessive. The closed loop regulator may have good speed of response at the cost of input saturation that may degrade regulation. The constraints on duty ratio perturbations (inputs) for the particular system of Chapter 3 are found to be

$$- .485 \leq \delta e_1(t) \leq .515 \tag{5.7}$$

$$- .337 \leq \delta e_2(t) \leq .148 + \delta e_1(t) \tag{5.8}$$

As we can see from the above equations, even after the input decoupling, it is possible that large disturbances and/or load changes in the first output can degrade regulation in the second output.

Utilizing the approppiate $MATRIX_X$ functions, the LQ design was automated so that for each LQR design (Q and r) all the above mentioned factors could be examined. The large signal nonlinear simulations for the closed loop performance tests of Table 5.1 were performed on the System Build tools of $MATRIX_X$. A satisfactory LQ design that satisfies all of the requirements mentioned above for the half-bridge converter described in Chapter 3 is presented next. Time and frequency domain results using the averaged model will be shown.

5.2.2 Final LQR designs

The LQR designs for both LTI small signal circuit models representing the half-bridge converter studied here were carried out independently on $MATRIX_X$. The final LQR designs follow the general guidelines mentioned in the last section. For output 1, a choice of weights that led to good performance was found, through iterative simulations, to be:

$$Q_1 = \begin{bmatrix} 6.5 \times 10^{12} & 0 & 0 \\ 0 & 9.5 \times 10^5 & 0 \\ 0 & 0 & 3.5 \end{bmatrix}, \quad r_1 = 6800 \tag{5.9}$$

Similarly, for output 2:

$$Q_2 = \begin{bmatrix} 7 \times 10^{12} & 0 & 0 \\ 0 & 8 \times 10^5 & 0 \\ 0 & 0 & 4 \end{bmatrix}, \quad r_2 = 7000 \tag{5.10}$$

The optimal state feedback gains for these LQR parameters are

$$G_1 = [30,907 \quad 11.08 \quad 0.114] \tag{5.11}$$

for output 1, and

$$G_2 = [30,694 \quad 11.01 \quad 0.16] \tag{5.12}$$

for output 2. The closed-loop poles for each design are

$$-2,620, \; (-2.45 \pm j2.38) \times 10^5 \tag{5.13}$$

for output 1 and

$$-2,600, \; (-3.5 \pm j3.4) \times 10^5 \tag{5.14}$$

for output 2. The closed-loop poles of each single-input single-output system lie well below one half the switching frequency (recall that $1/T = 500kHz$ or $3.14 \times 10^6 rad/sec$). The choice of the design parameters reflects the fact that the output voltage error must decay to zero in about two milliseconds and that the duty ratio perturbations must stay within the bounds given by (5.7) and (5.8). This is confirmed by the tests shown next.

5.2.3 Transient performance analysis

The performance tests in Table 5.1 were carried out on the System Build utility of $MATRIX_X$. The small-signal LQR state feedback controllers presented in the last section are simulated on the large-signal averaged model of the half-bridge converter as given by (3.16). Figure 5.2 presents the implementation block diagram of an LQ regulator applied to one of the output systems of the half-bridge converter, which subtracts the nominal reference signals from the inductor current and output voltage.

For the physical implementation of this controller, the waveform $E_{nom} + \delta e(t)$ is the reference signal for the PWM comparator of each output. In the simulations, both small signal controllers are integrated into the half-bridge converter large-signal model to obtain the total System Build average simulations.

Figures 5.3 and 5.4 show the transients of Test 1 (see Table 5.1), in which a current source of 10 A is effectively connected in parallel with the first output load resistance at .002 seconds. This effect is corroborated by the first output inductor current ($i_{l1}(t)$) transient shown in Fig. 5.3. Note that the first output average voltage $v_{o1}(t)$ deviates a maximun of .08 volts or 1.6 % from the steady state value and it settles back to this value in less than two milliseconds. Thus, the peak overshoot and settling time requirements are both met by this design. Also, the transient of $e_1(t)$ shows that the regulation requires a maximun duty ratio perturbation of .02 which is well below the constraints in the inequality in (5.7) and (5.8). This implies that the swing of $e_1(t)$ will not affect the regulation of the second output. However, as can be seen from $v_{o2}(t)$ in Figure 5.4, the second output voltage still undergoes a very small perturbation at .002 seconds. This is due to the small coupling effect of the coupling resistance r_w as expected from Chapter 3.

Figures 5.5 and 5.6 show the transients of Test 2, in which a source load current in the second output is stepped to 3 A at time .002 seconds. Since, except for the small effects of r_w, the first output is practically completely decoupled in the half-bridge converter, the small perturbations of output 1 for this test are not included. Again, the maximun peak deviation and settling time requirements for the second output voltage $v_{o2}(t)$ are met for this test. Also, the duty ratio perturbation $e_2(t)$ required is found to be nonexcessive.
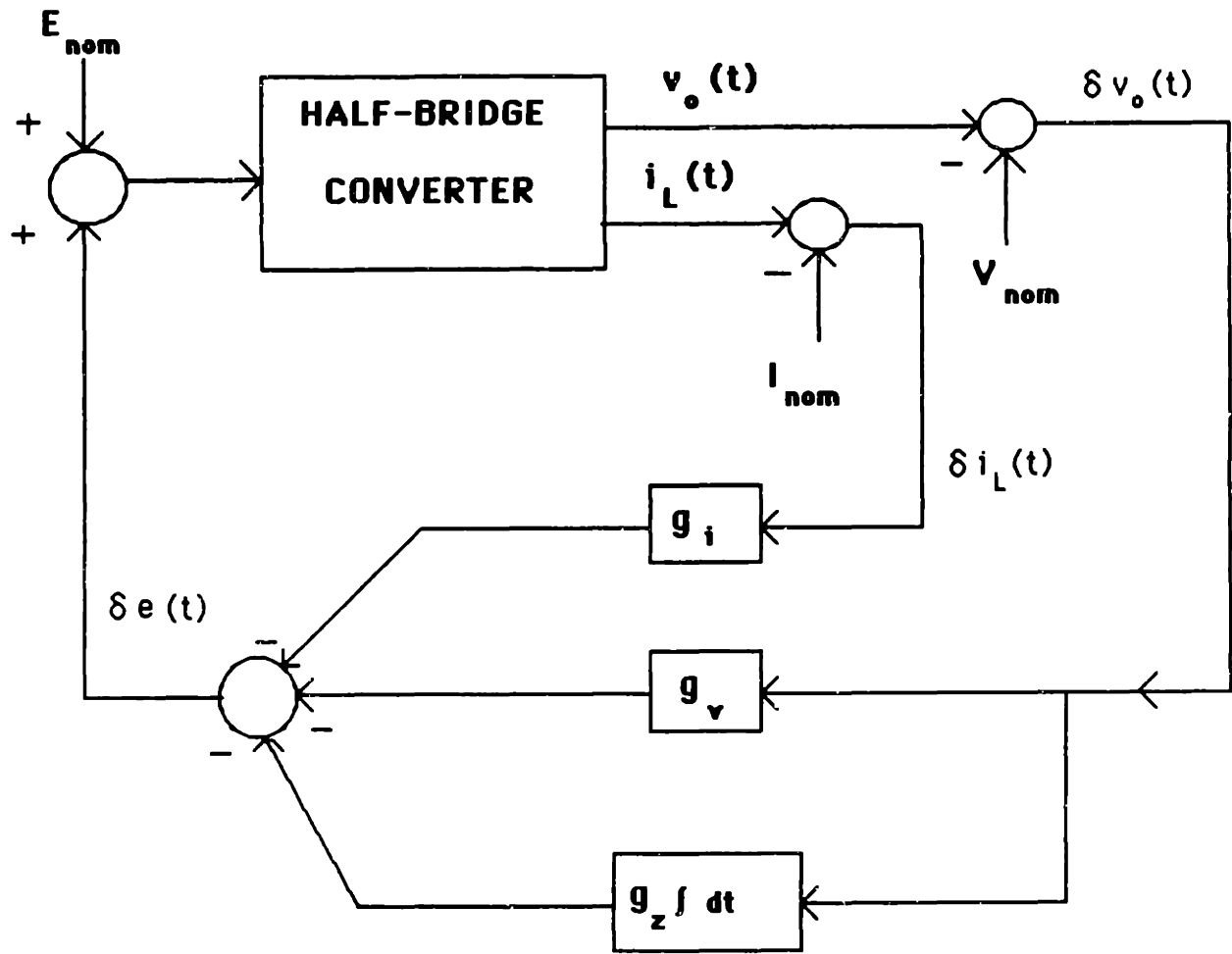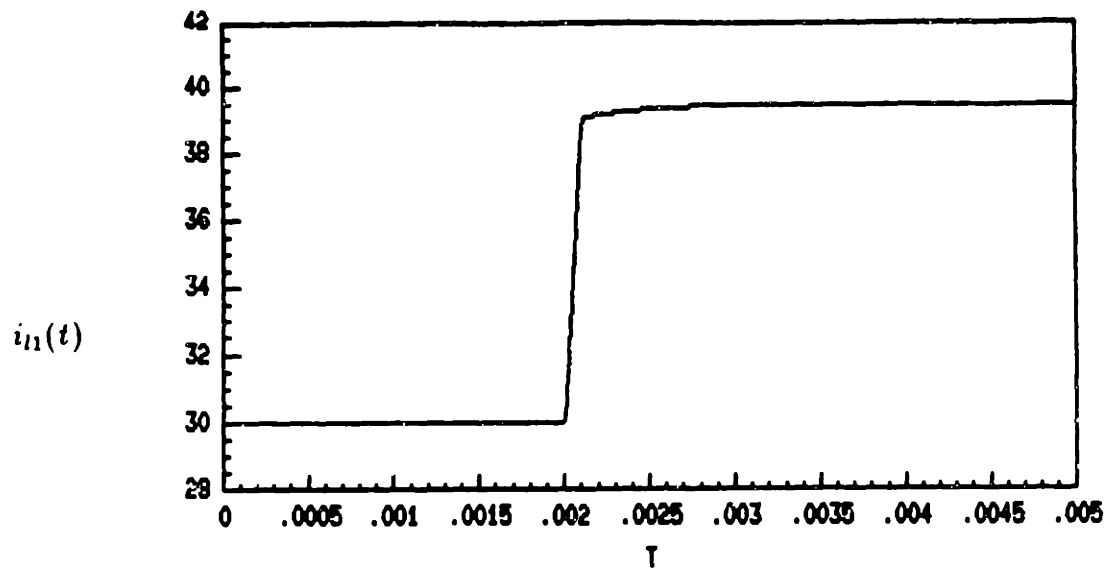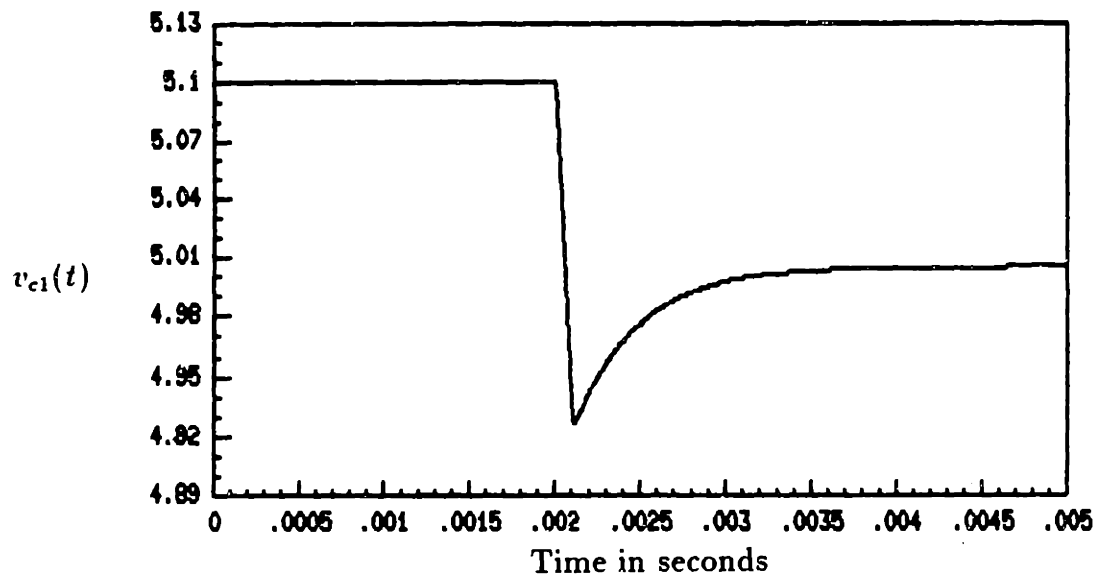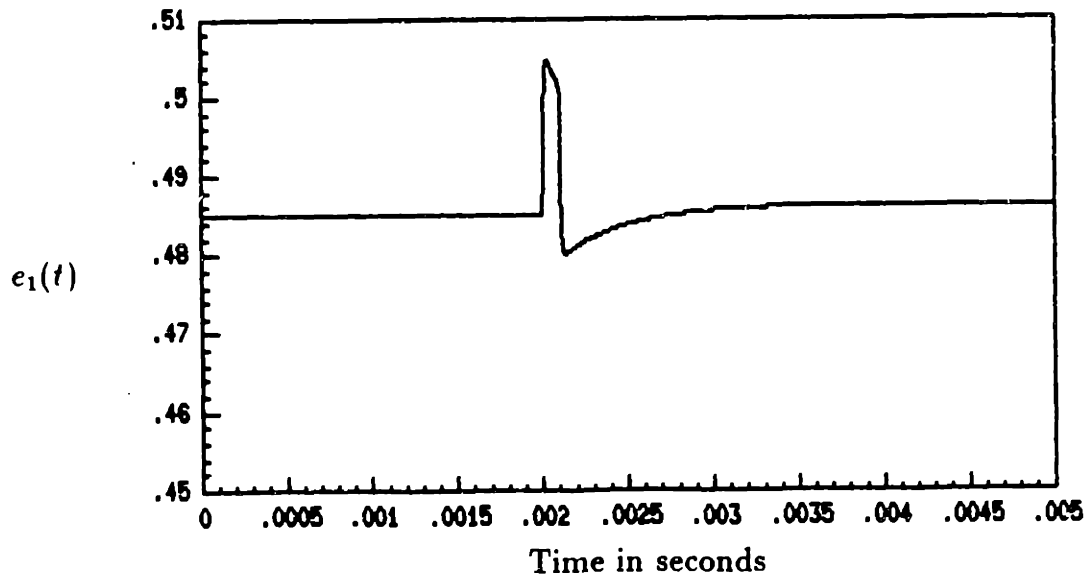
94

Figure 5.2: Implementation block diagram for the Linear Quadratic Regulator.

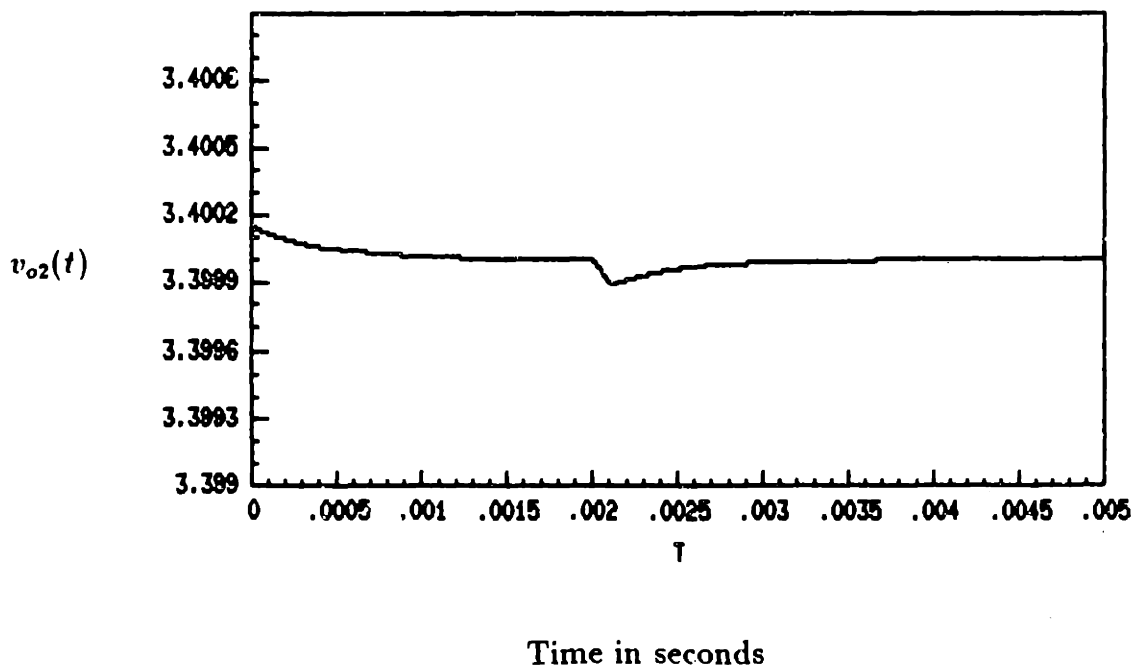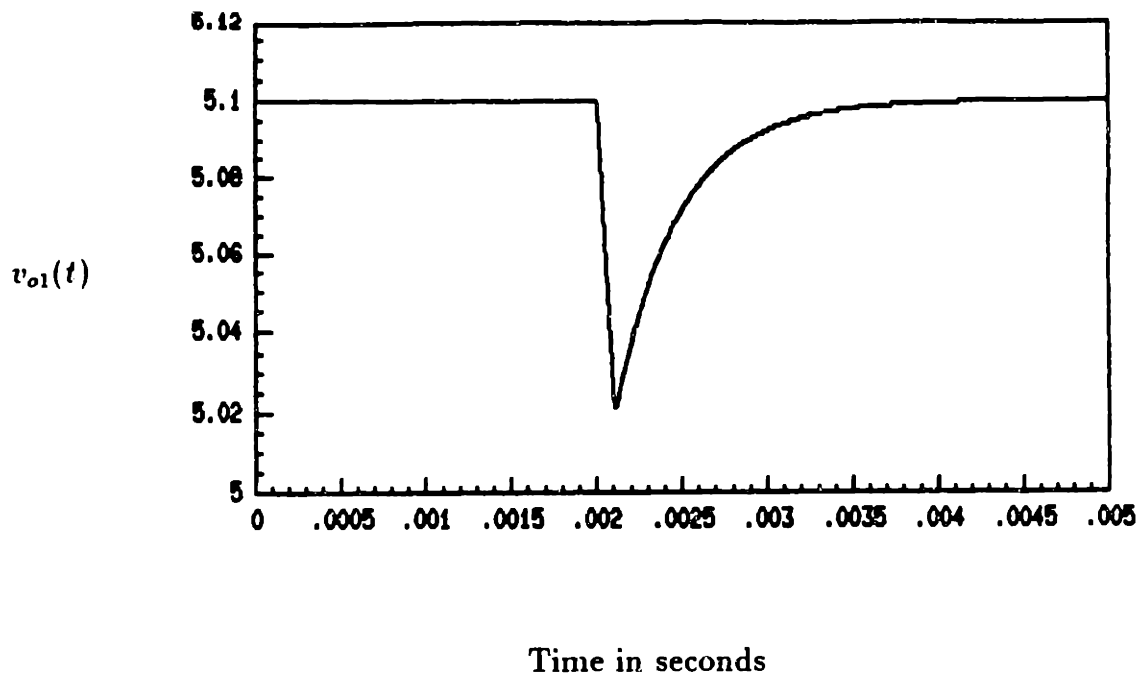Figure 5.3: Test 1 transients for $i_{l1}(t)$, $v_{c1}(t)$ and $e_1(t)$.

Figure 5.4: Test 1 transients for $v_{o1}(t)$ and $v_{o2}(t)$.

97

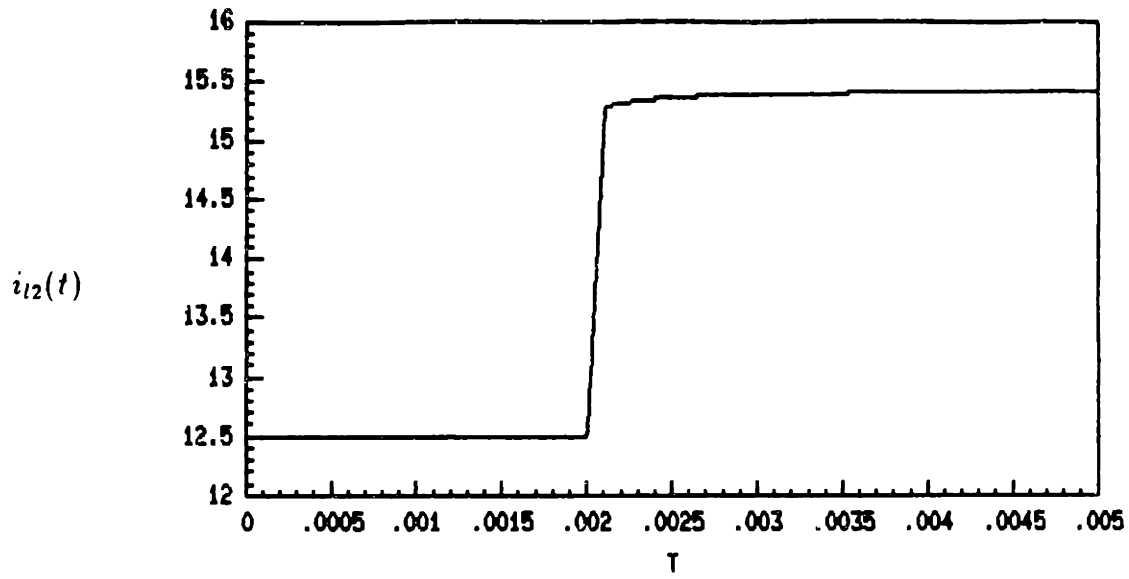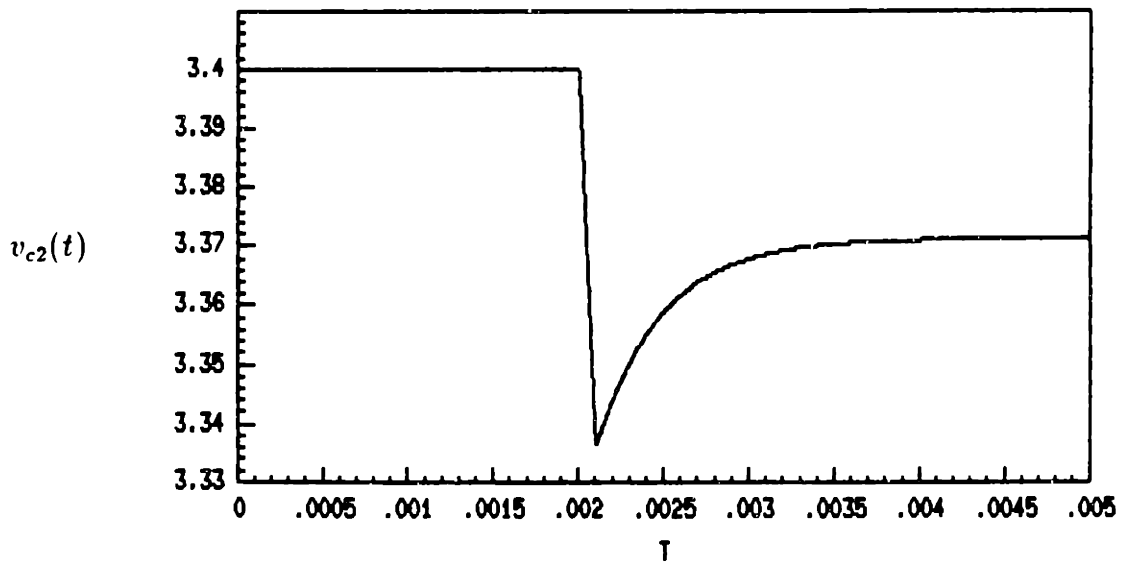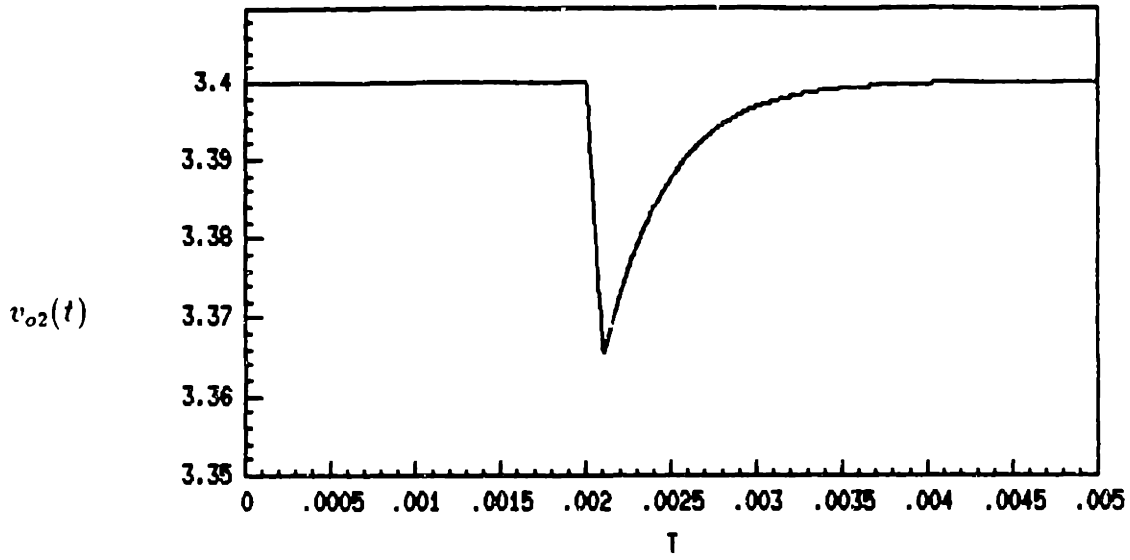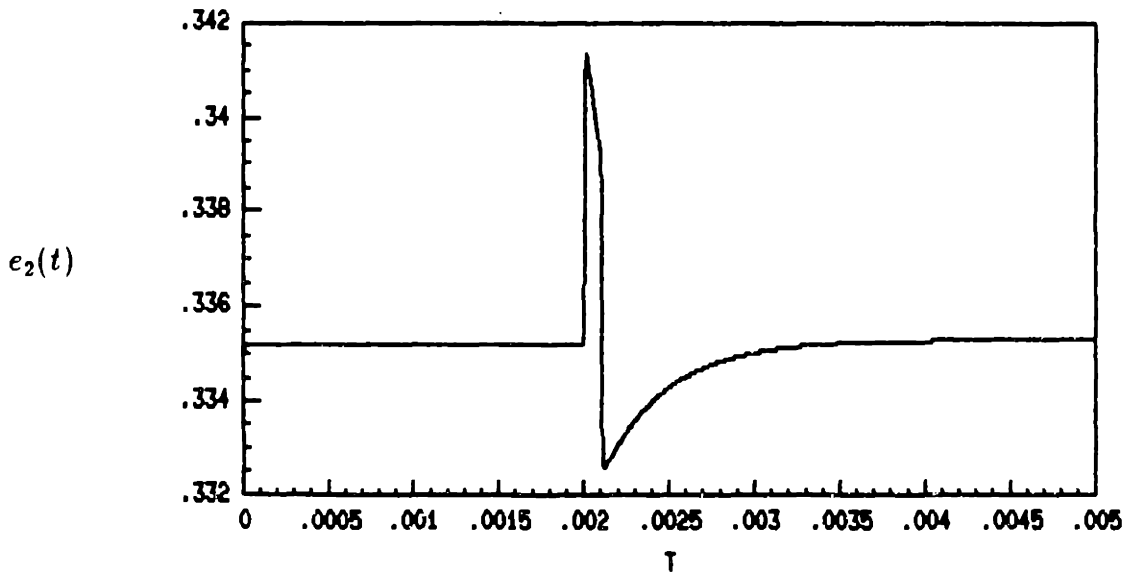$i_{l2}(t)$

Time in seconds

$v_{c2}(t)$

Time in seconds

Figure 5.5: Test 2 transients for $i_{l2}(t)$ and $v_{c2}(t)$.

Time in seconds

Time in seconds

Figure 5.6: Test 2 transients for $v_{o2}(t)$ and $e_2(t)$.

5.2.4 Frequency domain analysis

The Bode plots of $G_{LQ}(s)$ for both LQR designs are shown in Fig. 5.7. Note that the small-signal frequency domain analysis is only carried up to $1 \times 10^6 rad/sec$, which is close to one half the switching frequency, since averaged model predictions above that frequency should be discarded. These Bode plots show that our designs produced high-gain, high bandwidth closed-loop systems. The phase margins for both outputs are seen to be about 80 degrees. Recall from Chapter 4 that LQR designs have an inherent guaranteed phase margin of at least 60 degrees.

The magnitude plots of $S_{LQ}(s)$ and $C_{LQ}(s)$ for both designs are presented in Figs. 5.8 and 5.9, respectively. The plots of $S_{LQ}(s)$ show a gain attenuation of -20 dB or larger for $w < 1 \times 10^5 rad/sec$ so both systems have excellent disturbance rejection in this large frequency range. The closed-loop transfer function magnitude plots $C_{LQ}(s)$ are verified not to cross the stability robustness boundaries obtained in Chapter 3, so it is guaranteed that the actual half-bridge converter will remain stable under this controllers.

5.2.5 LQR Design Comments

The LQR designs required an iterative process of picking the best parameters Q and r. This procedure and the closed-loop performance evaluation are easily automated using $MATRIX_X$. The systematic LQR design procedure can easily be extended to genuine multivariable converters that can not justifiably be decoupled in the way possible for the half-bridge converter. However, the assumption that all state variables (e.g. inductor currents) are available for feedback might be unrealistic in real practice. Nevertheless, as stated in Chapter 4, LQR results can still be combined with state observers to obtain observer based compensators, which avoid the need to measure all state variables and can still result in robust designs. This will be shown in the next chapter for the half-bridge converter system analyzed here.
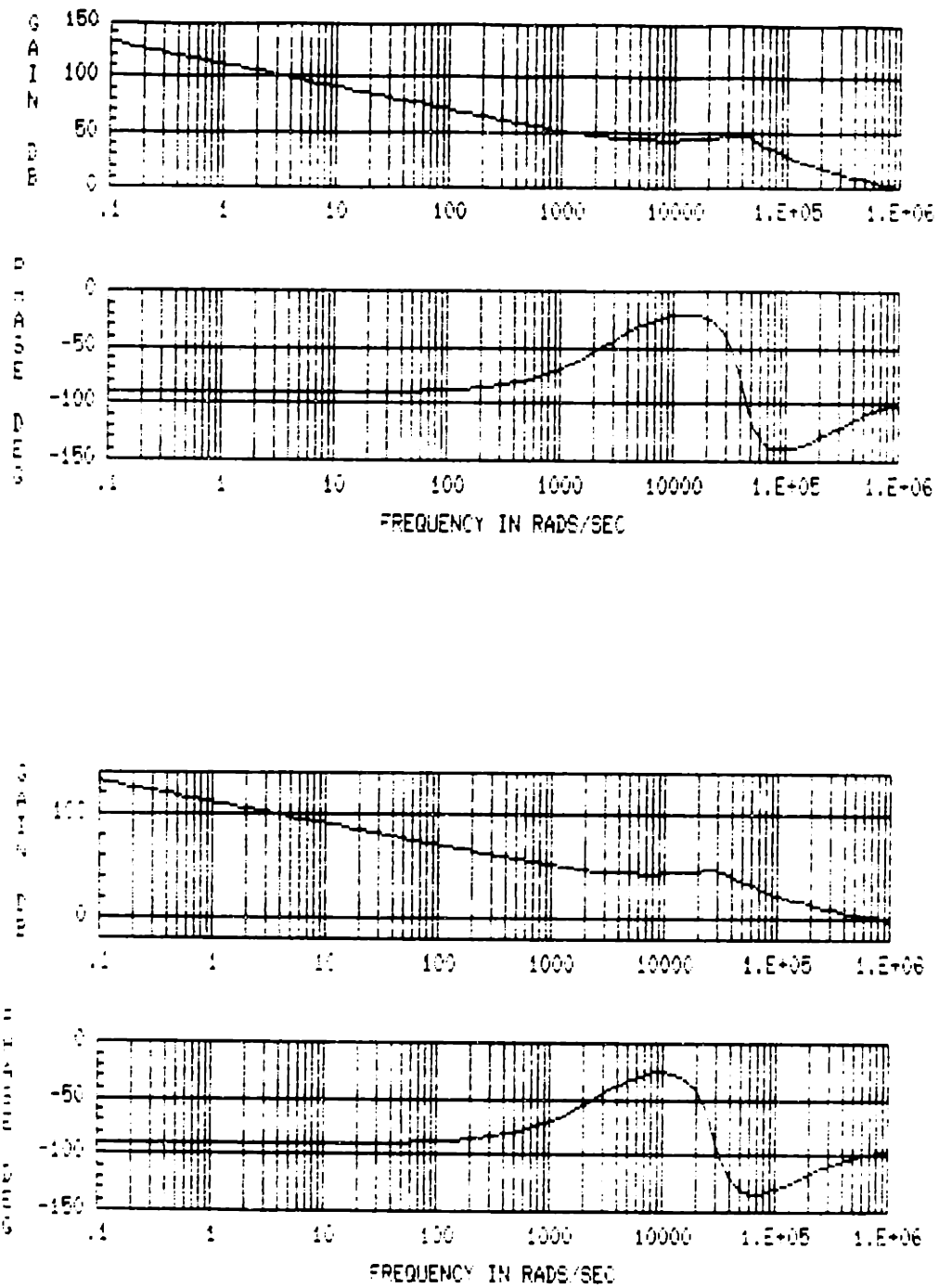
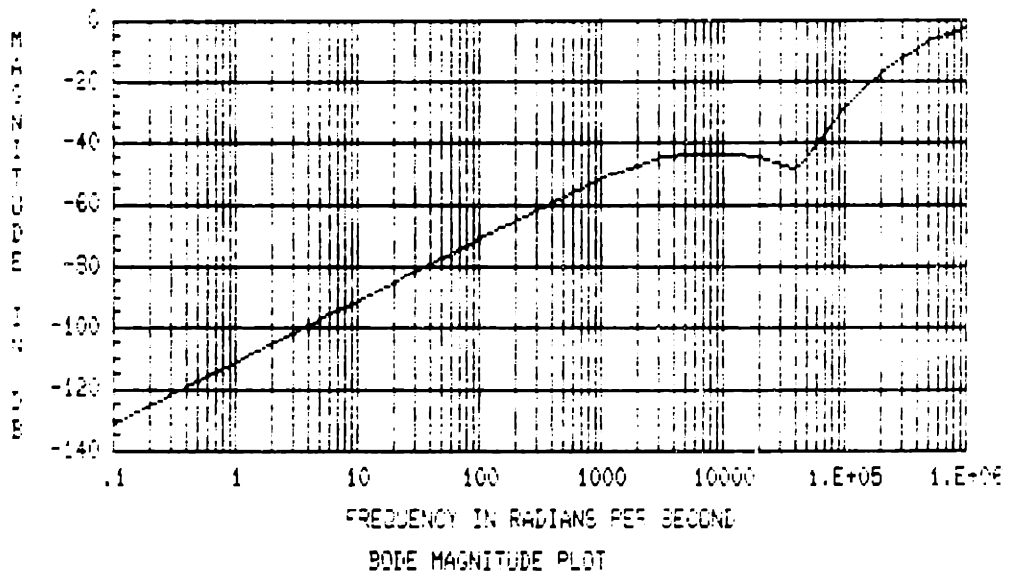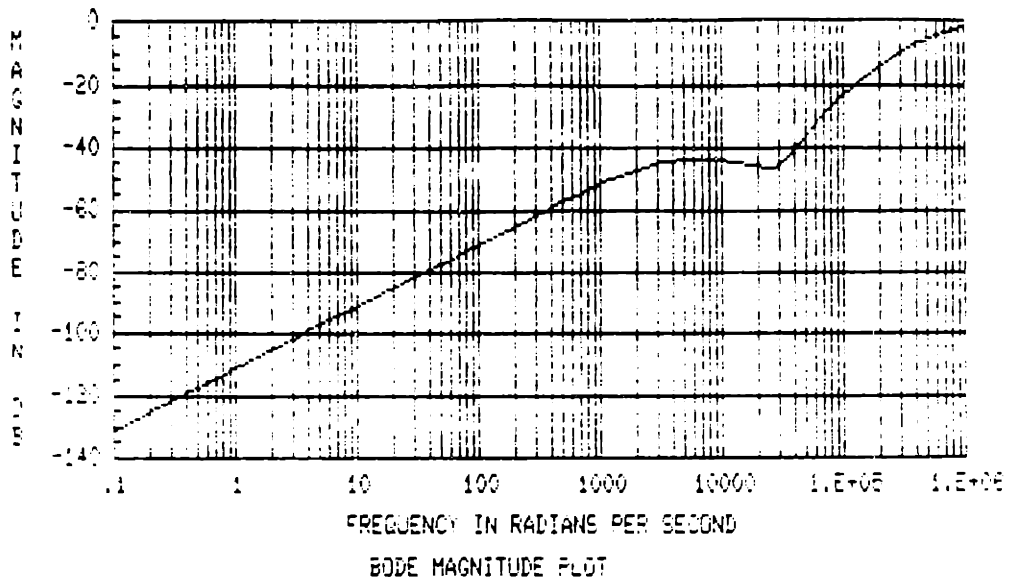Figure 5.7: Bode plot of $G_{LQ}(s)$ for output 1, top, and for output 2, bottom.

101

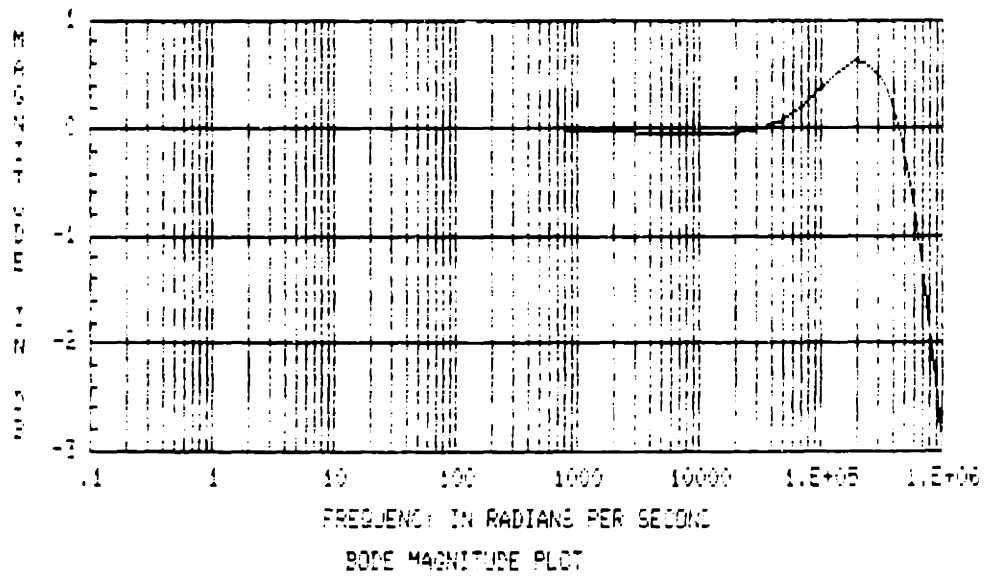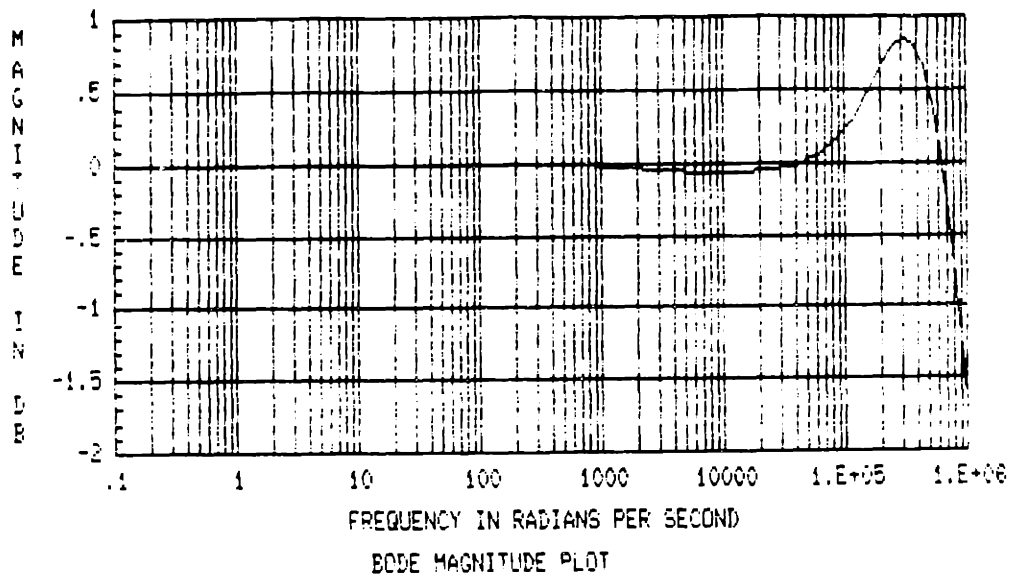Figure 5.8: Magnitude plot of $S_{LQ}(s)$ for output 1, top, and for output 2, bottom.

Figure 5.9: Bode plot of $C_{LQ}(s)$ for output 1, top, and for output 2, bottom.

Chapter 6

Observer Based Compensators

This chapter will address the design and evaluation of an observer-based controller for the half-bridge converter. Specifically, state-space estimators for the inductor currents in each output system will be obtained and combined with the state feedback LQ results presented in the last chapter, as described in Section 4.3.

6.1 Reduced Observer Design for Half-Bridge Converter

The main motivation behind the observer design here is to avoid the need to directly measure a state variable for feedback control purposes. The specific goal of this work is to obtain small-signal average estimates of the inductor currents in the power stage of the half-bridge converter, so that observer based compensators can be systematically obtained as shown in Chapter 4. As will be seen, the results are robust and result in controllers that only require measuring the perturbations in output voltage. The formulation for obtaining the dynamics of the small-signal current estimators will be presented next. The procedure to be shown here is specific to the models we are using;the general method for the design of a reduced order observer is presented in [20].

104

As mentioned before, this design will be based on the small-signal averaged state equations for each output system, namely (dropping the subscripts since the state equations are the same for each output),

$$\begin{bmatrix} \delta v_c'(t) \\ \delta i_l'(t) \end{bmatrix} = \begin{bmatrix} -\frac{\rho}{RC} & \frac{\rho}{C} \\ -\frac{\rho}{L} & \frac{r_e}{L} \end{bmatrix} \begin{bmatrix} \delta v_c(t) \\ \delta i_l(t) \end{bmatrix} + \begin{bmatrix} 0 \\ \frac{\alpha}{L} \end{bmatrix} \delta e(t) \qquad (6.1)$$

where $\alpha = N_s V_I / 2 N_p$ and ρ, r_e are as defined in Chapter 3. Let $\delta \hat{v}_c(t)$ and $\delta \hat{i}_l(t)$ be the real-time estimates of the small-signal capacitor voltage and inductor current, respectively. Then, assuming that the perturbation in average output voltage equals the perturbation in capacitor voltage ($\delta v_o(t) = \delta v_c(t) = \delta \hat{v}_c(t)$ - ignoring ESR), a real-time open-loop simulation from (6.1) for the small-signal differential equation of the inductor current gives

$$\delta \hat{i}_l'(t) = -\frac{\rho}{L} \delta v_o(t) - \frac{r_e}{L} \delta \hat{i}_l(t) + \frac{\alpha}{L} \delta e(t) \qquad (6.2)$$

The observer to be introduced corrects the above simulation by the use of a second constraint obtained from the first equation in (6.1). Note first that if $\delta \hat{i}_l(t) = \delta i_l(t)$, and using $\delta \hat{v}_c(t) = \delta v_o(t)$, we would have

$$\delta v_o'(t) + \frac{\rho}{RC} \delta v_o(t) - \frac{\rho}{C} \delta \hat{i}_l(t) = 0 \qquad (6.3)$$

The deviation of the left side from 0 serves as a measure of estimation error. Using the above constraint as a correction term in the open-loop simulation of (6.3) yields

$$\delta \hat{i}_l'(t) = -\frac{\rho}{L} \delta v_o(t) - \frac{r_e}{L} \delta \hat{i}(t) + \frac{\alpha}{L} \delta e(t) - h \left[\delta v_o'(t) + \frac{\rho}{RC} \delta v_o(t) - \frac{\rho}{C} \delta \hat{i}_l(t) \right] \qquad (6.4)$$

where h is the observer gain. Rearranging the above equation gives

$$\delta \hat{i}_l'(t) = \left(\frac{\rho}{C} h - \frac{r_e}{L} \right) \delta \hat{i}_l(t) - h \delta v_o'(t) - \left(\frac{\rho}{L} + \frac{\rho}{RC} \right) \delta v_o(t) + \frac{\alpha}{L} \delta e(t) \qquad (6.5)$$

Using (6.3), the observer error dynamics can be found to be given by the simple expression

$$\delta \tilde{i}_l'(t) = \delta i_l'(t) - \delta \hat{i}_l'(t) = \frac{\rho}{C} h \delta \tilde{i}_l(t) \qquad (6.6)$$

Thus, by choice of h we can modify the speed of convergence of this proposed observer. However, a direct implementation of (6.5) will require not only the perturbation in output voltage but its derivative as well. This is easily avoided by defining a new variable $q(t)$ as

$$q(t) = \delta\hat{i}_l(t) + h\delta v_o(t) \tag{6.7}$$

Using this transformation in (6.5) yields the implementable equation

$$q'(t) = \left(\frac{\rho}{C}h - \frac{r_e}{L}\right)q(t) - \left[\frac{\rho}{C}h^2 + \left(\frac{r_e}{L} - \frac{\rho}{RC}\right)h + \frac{\rho}{L}\right]\delta v_o(t) + \frac{\alpha}{L}\delta e(t) \tag{6.8}$$

The desired estimate $\delta\hat{i}_l(t)$ can be obtained from $q(t)$ by rearranging (6.7). Equations (6.8) and (6.7) can be simulated (or physically implemented) for each output in order to obtain the required small-signal estimate of the inductor current ($\delta\hat{i}_l(t)$) with the speed of convergence given by (6.6). Note that the only inputs necessary to obtain this estimate are the real-time signals of the output voltage and duty ratio perturbations. This estimate can then be fed back for use in the state feedback control law of Chapter 5 in place of the actual inductor current perturbation.

The proposed observer/controller closed-loop system for each output is shown in Fig. 6.1. The constant gains g_z, g_v, and g_i are the LQR feedback gain constants obtained in the last chapter. As discussed in Chapter 4, the poles or eigenvalues of this composite system are just the union of the LQR feedback poles and the observer poles.

The transfer function relation describing the 'observer' block in Fig. 6.1 is just obtained by taking Laplace transforms of (6.7) and (6.8). This yields

$$\delta\hat{i}_l(s) = -\frac{1}{s + (\frac{r_e}{L} - \frac{\rho}{C}h)}\left[-\frac{\alpha}{L}\delta e(s) + \left(hs + \left(\frac{\rho}{RC}h + \frac{\rho}{L}\right)\right)\delta v_o(s)\right]. \tag{6.9}$$

The total frequency domain expression for the compensator control law expression for each output can be easily obtained from Fig. 6.1 to be

$$\delta e(s) = \underbrace{-g_i\,\delta\hat{i}_l(s)}_{estimation\ feedback} \underbrace{- \left(g_v + \frac{g_z}{s}\right)\delta v_o(s)}_{P-I\ term} \tag{6.10}$$

106

where $\delta \hat{i}_l(s)$ is as given by (6.9), and the proportional-integral (P-I) term is due to the feedback of the output voltage perturbation and its integral. The control law described by (6.11) can be easily implemented in real-time using analog components as shown in Fig. 6.2. Appropriate choices of the parameters (R's and C's) are needed, of course. As can be seen, the input to the controller is just the output voltage perturbation, which can be obtained by subtracting the nominal reference voltage from the large signal output voltage. The output of the controller $\delta e(t)$ is the input to the error amplifier signal of the PWM chip which drives the transistor switch $s1$ or $s2$ in the primary of the converter as shown in Fig. 3.1.

6.2   Observer-Based-Controller Results

Once the simple relations presented in the last section are obtained, the design and analysis of the reduced observer design is straightforward. Since the same feedback gain constants presented in Chapter 5 will be used, the only new design parameters needed are the observer gains h_1 and h_2 for each output. These gains will determine the speed of convergence of our estimates. As mentioned in Chapter 4, a simple and reasonable guideline to use is to choose the observer poles two to three times faster than the slowest eigenvalue of the closed-loop state fedback control dynamics ($A_a - B_a G$ in this case). In our case, we still have to check that the corresponding observer poles are also below one-half the switching frequency, so that the validity of the averaged model is not violated.

Specifically, substituting the required numerical values into (6.6), the observer error dynamics for each output are given by

$$\delta \tilde{i}'_{l1}(t) = 2361 h_1 \delta \tilde{i}_{l1}(t) \tag{6.11}$$

$$\delta \tilde{i}'_{l2}(t) = 4822 h_2 \delta \tilde{i}_{l2}(t) \tag{6.12}$$

From (5.13) and (5.14), the dynamics of the LQR feedback loops are governed by a pole
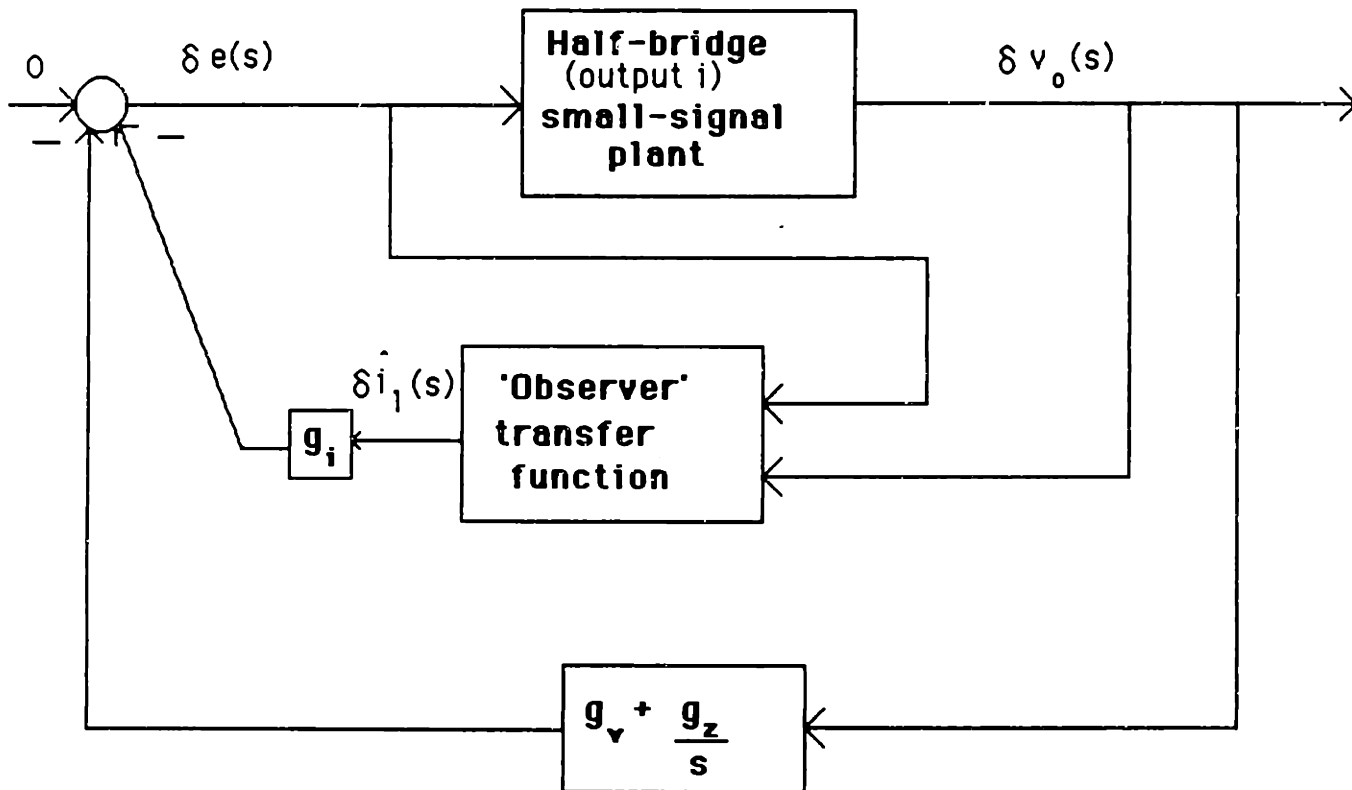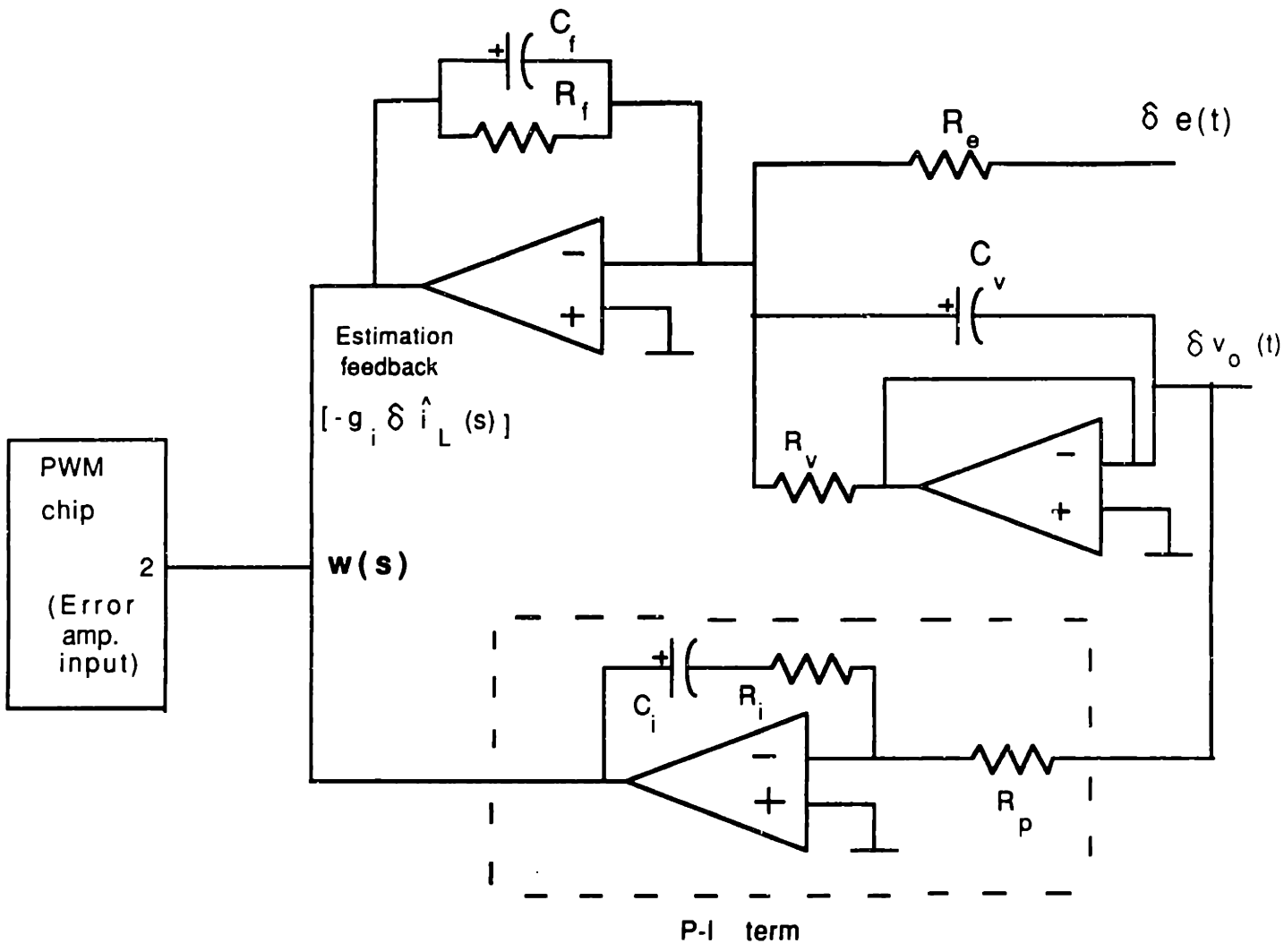
Figure 6.1: Observer-based compensator block diagram.

$$w(s) = - \frac{R_f}{1 + R_f C_f s} [G_e \, \delta e(s) + (C_v s - G_v) \, \delta V_o(s)]$$

$$- \frac{R_i C_i s + 1}{R_p C_i s} \, \delta V_o(s)$$

Figure 6.2: Compensator hardware implementation.

at about $-2,600$ *nepers*. By choosing $h_1 = -3.3$ and $h_2 = -1.7$, the error dynamics of both observers are three times faster than this frequency.

Time and frequency domain results for the resultant compensator design will be presented next. As before, the resultant designs will be seen to satisfy all closed-loop specifications and requirements presented in Chapter 5. The simulations on $MATRIX_X$ only required a simple extension in order to obtain the estimate of $\delta \hat{i}_l(t)$ as required by (6.7) and (6.8).

6.2.1 Transient performance analysis

Figure 6.3 shows the closed-loop compensator transients of Test 1 for the half-bridge converter. As seen from the figure, the required duty ratio perturbations for $e_1(t)$ are nonexcessive, so the second output is practically insensitive to this test. Note that the first output average voltage deviates only 0.8 % from the steady state value of 5.1 V and it settles back to this value in less than the specified 2 milliseconds. Recall that the maximum perturbation for the LQR full state feedback design was 1.6 % for this same test.

Figure 6.4 shows the transients for Test 2 of the second output. The first output was found to be insensitive to this disturbance. Again, the required input duty ratio perturbation in $e_2(t)$ was found to be nonexcessive. Also, the time domain output voltage regulation of this output showed a satisfactory response since the maximum peak deviation was only 0.6 % from the steady state average value of 3.4 volts and the settling time is still less than 2 milliseconds.

6.2.2 Frequency Domain Analysis

The Bode plots of the equivalent loop transfer function of the observer based compensator shown in Fig. 6.1 for both outputs are shown in Fig. 6.5. These Bode
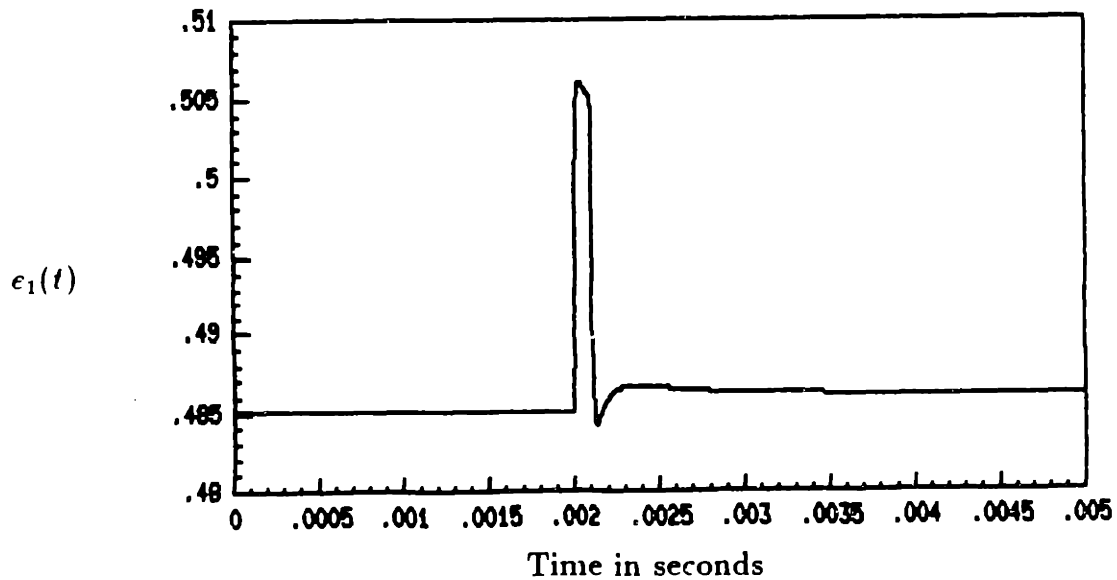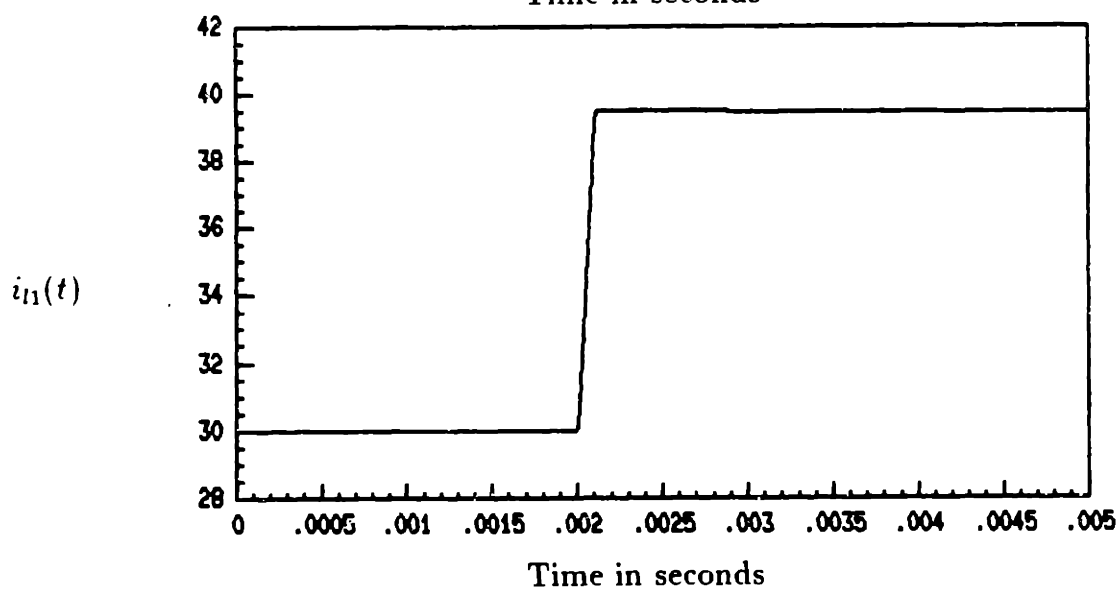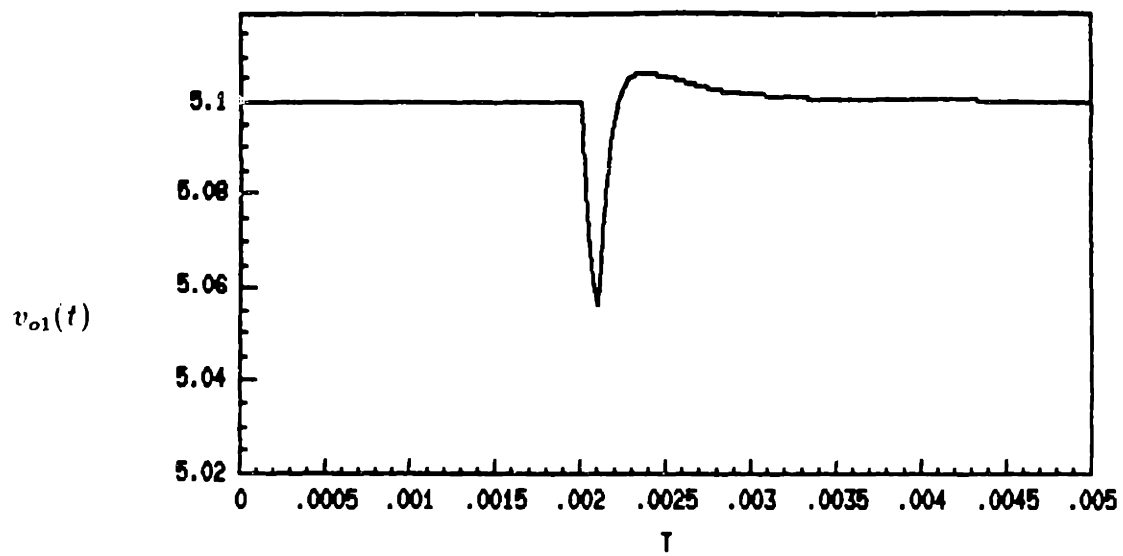
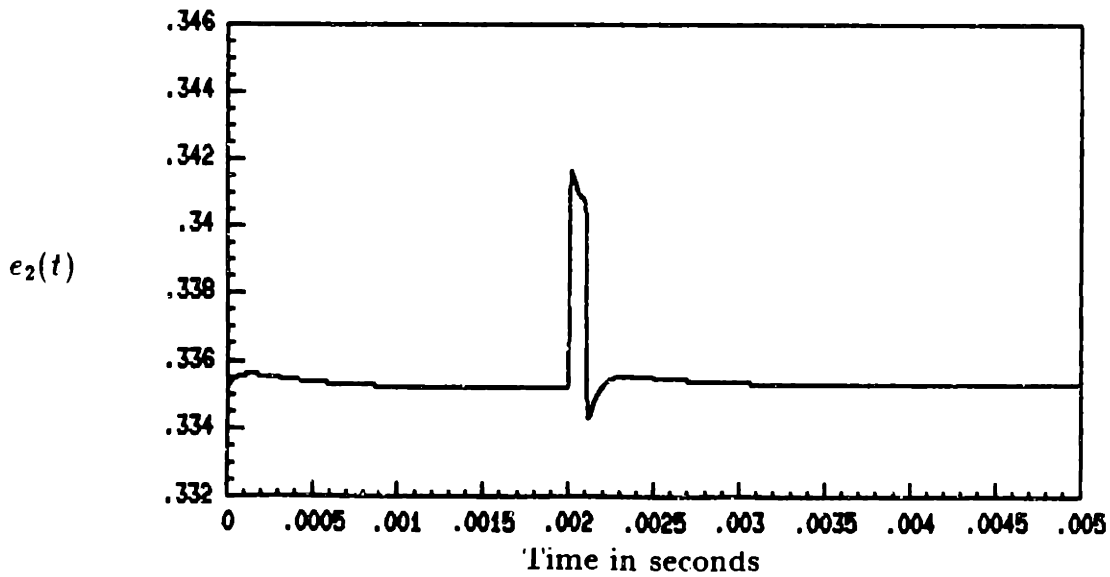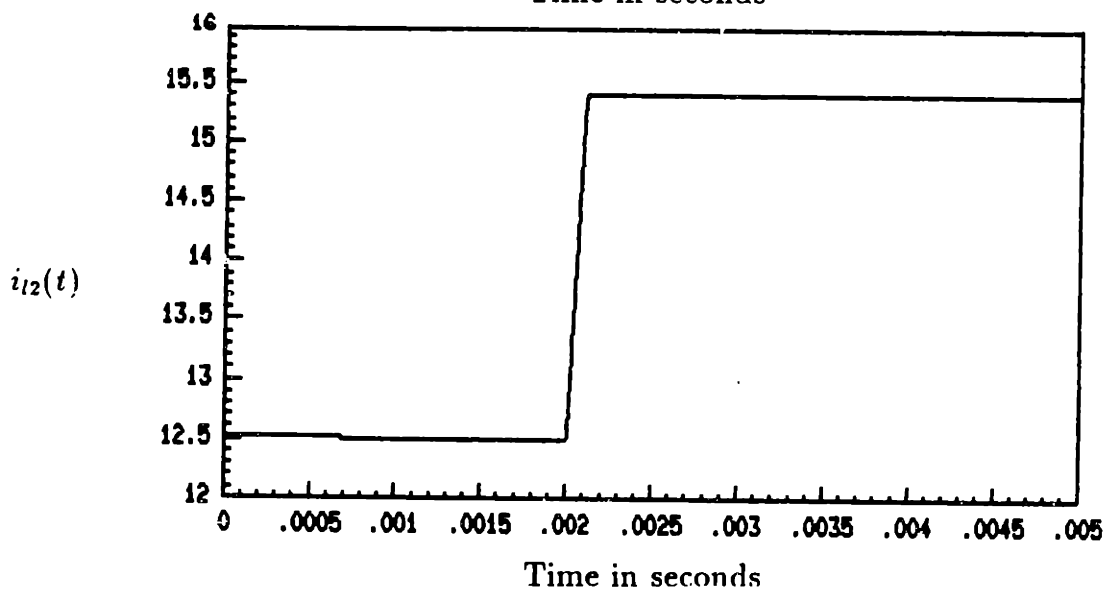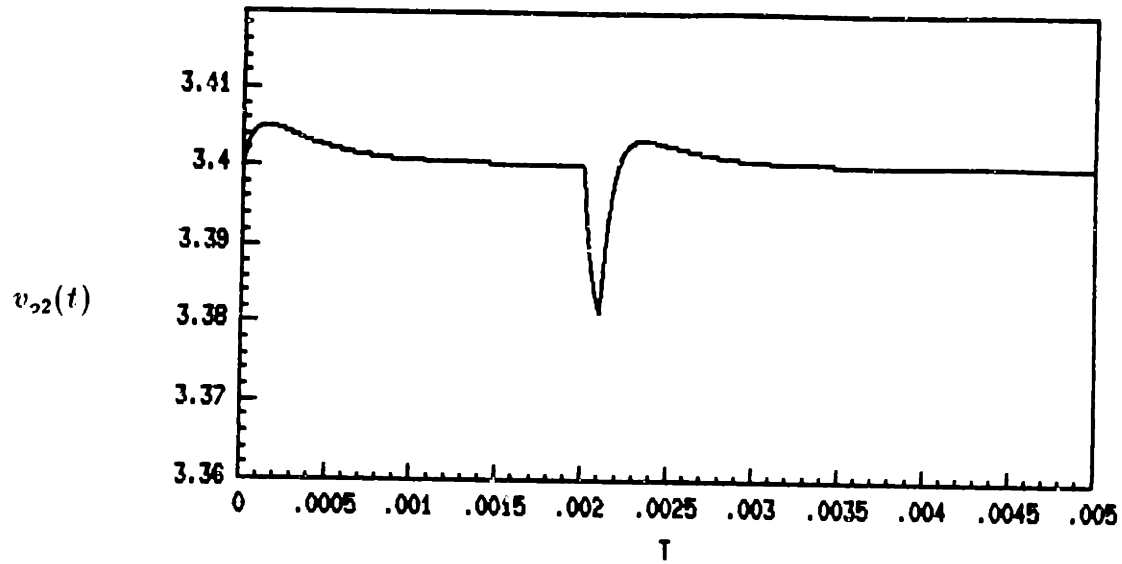Figure 6.3: Test 1 transients for $v_{o1}(t)$, $i_{l1}(t)$ and $e_1(t)$.

Figure 6.4: Test 2 transients for $v_{o2}(t)$, $i_{l2}(t)$ and $e_2(t)$.

plots show bandwidths comparable to the full state feedback controllers presented in Chapter 5. However, the gain margins for both outputs here are seen to be about 60 degrees, which represent a reduction of about 20 degrees in phase robustness. The corresponding sensitivity transfer functions for both outputs are shown in Figure 6.6. This corresponds to the transfer function between a disturbance at the input of the small-signal plant and the output voltage. These plots only show a disturbance attenuation of more than 20 dB for frequencies below 1000 rad/sec. Thus, by analyzing the frequency domain, we can conclude that a small penalty in robustness is paid by the use of observers to eliminate the need of measuring the inductors currents. The closed loop transfer functions were again verified not to cross the stability robustness boundaries of Chapter 3.
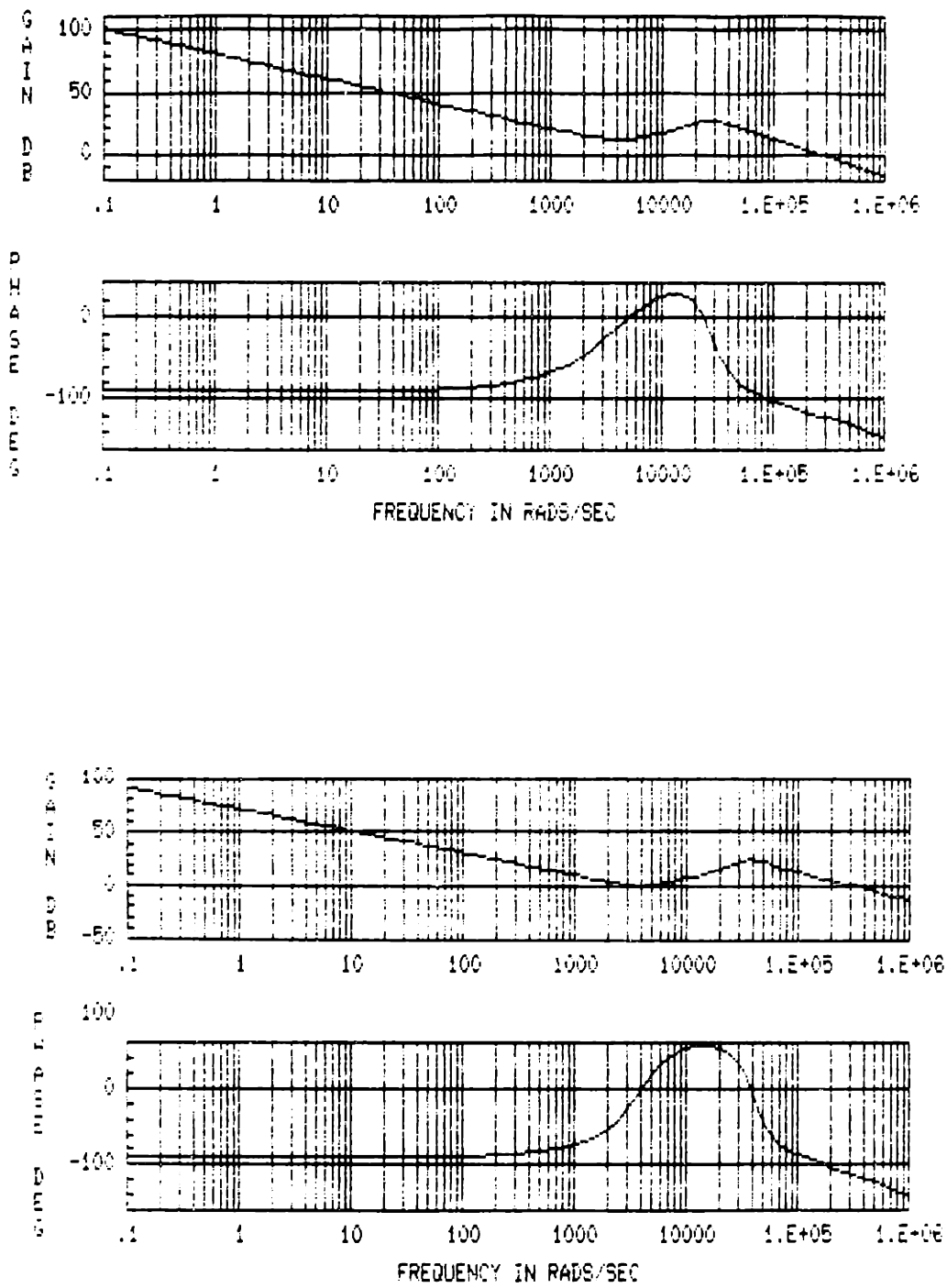
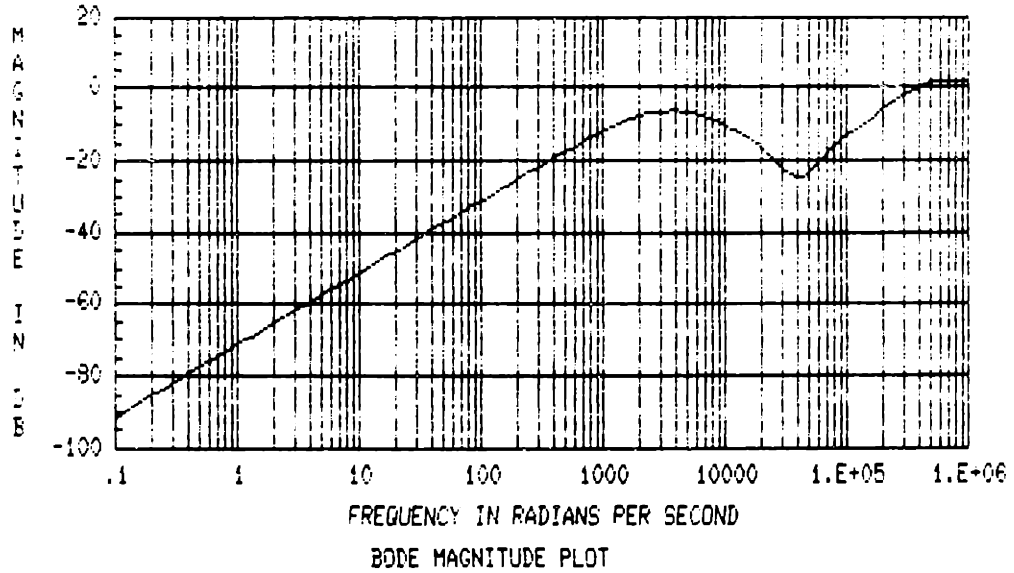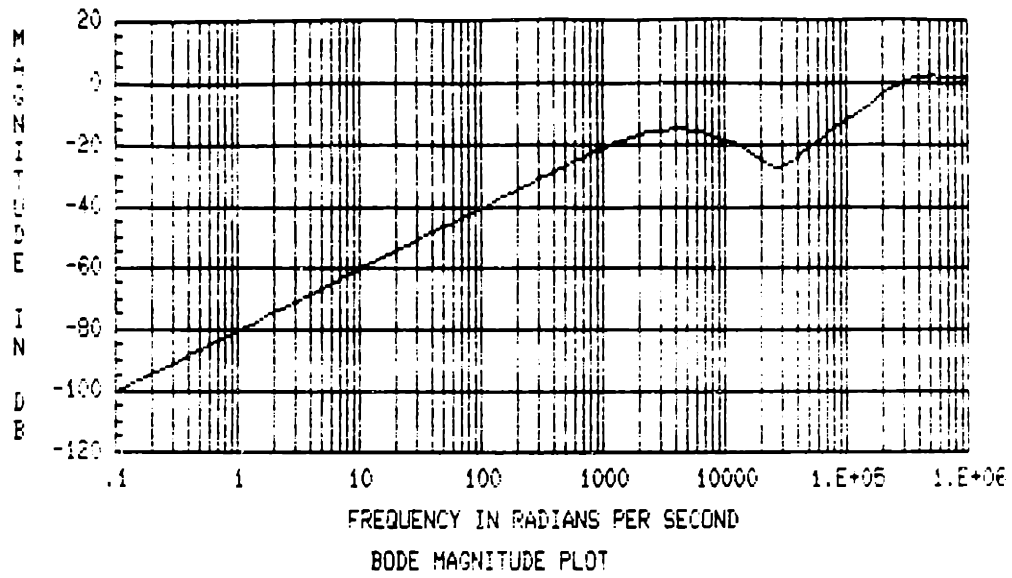**Figure 6.5:** Bode plots of loop transfer functions for output 1, top, and for output 2, bottom.

Figure 6.6: Sensitivity transfer functions for output 1, top, and for output 2, bottom.

Chapter 7

Conclusions and Further Research

7.1 Conclusions

This thesis has investigated issues concerning the modeling and control of high frequency switching converters.

A correction to the usual derivation of state-space averaged models for constant frequency, current mode controlled converters was given and new results were shown and compared with the literature. Approximate sampled-data models, which are as easily obtained as continuous time averaged models, were shown to be more accurate than the latter because they properly represent the cyclic operation of switched converters. The two-output two-switch half-bridge converter was modeled, and it was found that the multivariable models of this converter can be decoupled into two single-input single-output systems. The stability robustness of the closed-loop half-bridge converter was examined and the guaranteed stability tests obtained were shown not to be overly limiting on the bandwidth.

The Linear Quadratic Regulator feedback design method was presented and systematically applied via $MATRIX_X$ to each output of the decoupled half-bridge converter model. The regulation of the full closed loop was evaluated through simulated performance tests, and was found to meet stringent closed-loop power supply specifications.

Assuming unavailability of measurements of the converter inductor current, observer based compensator designs for each output were obtained and analyzed in the same manner. Results for the observer based designs were found to be satisfactory. A simple hardware implementation for the above mentioned observer based compensators was proposed.

7.2 Further Work

Work in this thesis shows that a modern state feedback control approach can yield a systematic procedure for obtaining robust controllers for switching power converters. The results shown here should be compared with a current mode control design for a similar half-bridge converter and the trade-offs should be examined.

Our results should be tested in hardware, especially if the latter comparison is favorable, as we expect it to be. The state space control methods presented here can be easily extended to obtain genuine multivariable controllers for non-decoupable converters. A clear motivation for research is to extend the approaches presented here to a genuine multivariable converter and to compare this with results from classical control methods.

Appendix A

Sampled-Data Model Matrices for the Half-Bridge Converter Decoupled System

Using the definitions for each output $(i = 1, 2)$:

$$a_i = \frac{\rho_i L_i + r_{ei} C_i R_i}{2 L_i C_i R_i}$$

$$b_i = \frac{1}{2} \left[\frac{4\rho_i(r_{ei} + \rho_i R_i)}{L_i C_i R_i} - \left(\frac{\rho_i L_i + r_{ei} C_i R_i}{L_i C_i R_i} \right)^2 \right]^{1/2}$$

$$\Lambda_i = \left[\left(\frac{a_i - \rho_i / C_i R_i}{b_i} \right)^2 + 1 \right]^{1/2}$$

$$\Sigma_i = \left[\left(\frac{a_i - r_{ei} / L_i}{b_i} \right)^2 + 1 \right]^{1/2}$$

$$\theta_i = tan^{-1} \left(\frac{a_i - \rho_i / C_i R_i}{b_i} \right)$$

$$\phi_i = tan^{-1} \left(\frac{a_i - r_{ei} / L_i}{b_i} \right)$$

$$\lambda_i = -a_i(1 - e_1(k))T$$

$$\omega_i = b_i(1 - e_1(k))T$$

and

$$\mu = -a_1 e_1(k)T$$

$$\xi = -a_2 e_2(k)T$$

$$\beta = b_1 e_1(k)T$$

$$\alpha = b_2 e_2(k)T$$

Large Signal Matrices

$$A_{si} = \begin{bmatrix} \Sigma_i e^{-a_i T}\cos(b_i T + \phi_i) & \frac{\rho_i}{C_i b_i}e^{-a_i T}\sin b_i T \\ -\frac{\rho_i}{L_i b_i}e^{-a_i T}\sin b_i T & \Lambda_i e^{-a_i T}\cos(b_i T + \theta_i) \end{bmatrix}$$

$$B_{s1} = \frac{N_s e^{\lambda_1}}{2N_p L_1(a_1^2+b_1^2)} \left\{ \begin{bmatrix} \frac{\rho_1 \Sigma_1}{C_1}[1 - e^{\mu}(\frac{a_1}{b_1}\sin\beta + \cos\beta)]\cos(\omega_1 + \phi_1) \\ -\frac{\rho_1^2}{L_1 C_1 b_1}[1 - e^{\mu}(\frac{a_1}{b_1}\sin\beta + \cos\beta)]\sin\omega_1 \end{bmatrix} \right.$$

$$\left. + \begin{bmatrix} \frac{\rho_1 \Lambda_1}{C_1 b_1}[e^{\mu}(-a_1\cos(\beta + \theta_1) + b_1\sin(\beta + \theta_1)) + a_1\cos\theta_1 + b_1\sin\theta_1]\sin\omega_1 \\ \Lambda_1^2[e^{\mu}(-a_1\cos(\beta + \theta_1) + b_1\sin(\beta + \theta_1)) + a_1\cos\theta_1 + b_1\sin\theta_1]\cos(\omega_1 + \theta_1) \end{bmatrix} \right\}$$

$$B_{s2} = \frac{N_s e^{\lambda_2}}{2N_p L_2(a_2^2+b_2^2)} \left\{ \begin{bmatrix} \frac{\rho_2 \Sigma_2}{C_2}[1 - e^{\xi}(\frac{a_2}{b_2}\sin\alpha + \cos\alpha)]\cos(\omega_2 + \phi_2) \\ -\frac{\rho_2^2}{L_2 C_2 b_2}[1 - e^{\xi}(\frac{a_2}{b_2}\sin\alpha + \cos\alpha)]\sin\omega_2 \end{bmatrix} \right.$$

$$\left. + \begin{bmatrix} \frac{\rho_2 \Lambda_2}{C_2 b_2}[e^{\xi}(-a_2\cos(\alpha + \theta_2) + b_2\sin(\alpha + \theta_2)) + a_2\cos\theta_2 - b_2\sin\theta_2]\sin\omega_2 \\ \Lambda_2^2[e^{\xi}(-a_2\cos(\alpha + \theta_2) + b_2\sin(\alpha + \theta_2)) + a_2\cos\theta_2 - b_2\sin\theta_2]\cos(\omega_2 + \theta_2) \end{bmatrix} \right\}$$

Small Signal Matrices

$$\left(\frac{\partial f_i}{\partial x_i(k)}\right)_Q = A_{si}$$

$$\left(\frac{\partial f_i}{\partial e_i(k)}\right)_Q = \begin{pmatrix} fe_{i1} \\ fe_{i2} \end{pmatrix}$$

119

$$
\begin{aligned}
fe_{11} \;=\; & \frac{\rho_1 \Sigma_1 TV_I N_s}{2C_1 L_1 (a_1^2 + b_1^2) N_p} e^{-a_1 T} \left\{ \cos(\omega_1 + \phi_1)[a_1 e^{-\mu} - a_1 \cos\beta + b_1 \sin\beta] \right. \\
& + \; \sin(\omega_1 + \phi_1)[b_1 e^{-\mu} - a_1 \sin\beta - b_1 \cos\beta] \} \\
& + \; \frac{\rho_1 \Lambda_1 TV_I N_s}{2C_1 L_1 b_1 (a_1^2 + b_1^2) N_p} e^{-a_1 T} \left\{ \cos\omega_1[-b_1 e^{-\mu}(a_1 \cos\theta_1 + b_1 \sin\theta_1) + a_1 b_1 \cos(\beta + \theta_1)] \right. \\
& + \; \sin\omega_1[a_1 e^{-\mu}(a_1 \cos\theta_1 + b_1 \sin\theta_1) + a_1 b_1 \sin(\beta + \theta_1) + b_1^2 \cos(\beta + \theta_1)] \}
\end{aligned}
$$

$$
\begin{aligned}
fe_{12} \;=\; & -\frac{\rho_1^2 TV_I N_s}{2L_1^2 C_1 b_1 (a_1^2 + b_1^2) N_p} e^{-a_1 T} \left\{ \cos\omega_1[-b_1 e^{-\mu} + a_1 \sin\beta + b_1 \cos\beta] \right. \\
& + \; \sin\omega_1[a_1 e^{-\mu} - a_1 \cos\beta + b_1 \sin\beta] \} \\
& + \; \frac{\Lambda_1^2 TV_I N_s}{2L_1 (a_1^2 + b_1^2) N_p} e^{-a_1 T} \left\{ \cos(\omega_1 + \theta_1)[a_1 e^{-\mu}(a_1 \cos\theta_1 + b_1 \sin\theta_1) + a_1 b_1 \sin(\beta + \theta_1)] \right. \\
& + \; \sin(\omega_1 + \theta_1)[b_1 e^{-\mu}(a_1 \cos\theta_1 + b_1 \sin\theta_1) - a_1 b_1 \cos(\beta + \theta_1) + b_1^2 \sin(\beta + \theta_1)] \}
\end{aligned}
$$

$$
fe_{21} \;=\; \frac{\rho_2 TV_I N_s}{2C_2 L_2 b_2 N_p} e^{\lambda_2} e^{\xi} \{ \Lambda_2 \cos(\alpha + \theta_2)\sin\omega_2 + \Sigma_2 \cos(\omega_2 + \phi_2)\sin\alpha \}
$$

$$
fe_{22} \;=\; \frac{TV_I N_s}{2N_p} e^{\lambda_2} e^{\xi} \left\{ \frac{\Lambda_2^2}{L_2} \cos(\alpha + \theta_2)\cos(\omega_2 + \theta_2) - \frac{\rho_2^2}{C_2 L_2^2 b_2^2} \sin\alpha \sin\omega_2 \right\}
$$

Bibliography

[1] S.P. Hsu, A. Brown, L.Rensink and R.D. Middlebrook, "Modeling and analysis of switching dc-to-dc converters in constant-frequency current-programmed mode," *IEEE PESC* 1979.

[2] R.D. Middlebrook, "Topics in multiple-loop regulators and current-mode programming," *IEEE Trans. Power Electronics*, April 1987.

[3] D.M. Mitchell. *DC-DC Switching Regulator Analysis*, McGraw-Hill, 1988.

[4] R.D. Middlebrook and S. Cuk. "A general unified approach to modeling switching converter power stages," *IEEE PESC* 1976.

[5] L.S. Alvarez. *Control of Multiple-Switch Multi-Output Power Converters*, Master's thesis, M.I.T. 1988.

[6] A. Capel. "Charge controlled conversion principle in dc/dc regulators combine dynamic performances and high output power," *IEEE PESC* 1979.

[7] G.C. Verghese, M.E. Elbuluk and J.G. Kassakian. "A general approach to sampled-data modeling for power electronic circuits," *IEEE Trans. Power Electronics*, April 1986.

[8] G.C. Verghese, J.G. Kassakian and M.F. Schlect. *Principles of Power Electronics course lecture notes*, Course 6.334, M.I.T.

[9] G.C. Verghese, J.H. Lang and M. Ilic-Spong. "Modeling and control challenges in power electronics," *25th IEEE Conference on Decision and Control*, 1986.

[10] B.E. Andersen, C.W. Boettcher, B.H. Hamilton, D.D. Retotar and R.E. Schroeder. "Analysis of the static characteristic and dynamic response of push-pull switching converters operating in the current programmed mode," *IEEE PESC*, 1981.

[11] F.C. Lee and R.A. Carter. "Investigations of stability and dynamic performances of switching regulators employing current-injected control," *IEEE PESC*, 1981.

[12] A.R. Brown and R.D. Middlebrook. "Sampled-data modeling of switching regulators," *IEEE PESC*, 1981.

[13] K. Mahabir. *Digital Control of Large Signal Behavior in Switched DC-DC Converters*, Engineer's thesis, M.I.T. 1989.

[14] M. Athans. *Multivariable Control Systems II Lecture Notes*, Course 6.234J, M.I.T., Spring 1989.

[15] M. Athans. *Multivariable Control Systems II View Graphs*, Course 6.234J, M.I.T., Spring 1989.

[16] F. Lewis. *Optimal Control*, John Wiley & Sons, 1986.

[17] H. Kwakernaak and R. Sivan. *Linear Optimal Control Systems*, John Wiley & Sons, 1980.

[18] F.C. Lee, Z.D. Zang and T.H. Lee. "Optimal design strategy of switching converters employing current injected control," *IEEE Transactions on Aerospace and Electronic Systems*, January 1985.

[19] R.D. Middlebrook. "Modeling current-programmed buck and boost regulators," *IEEE Transactions on Power Electronics*, January 1989.

[20] D.G. Luenberger. *Introduction to Dynamic Systems*, John Wiley & Sons, 1979.

[21] C.T. Chen. *Linear System Theory and Design*, CBS College Publishing, 1984.

[22] G.C. Verghese, J.G. Kassakian, and M.F. Schlecht, *Principles of Power Electronics*, Addison-Wesley, 1989.

[23] C.A. Bruzos, *Modeling And Control For Multi-Output Switched Converters Part II, Program Documentation*, MIT lab. for Electromagnetic and Electronic Systems Report, May 1989.

[24] G.C. Verghese, C.A. Bruzos, and K.N. Mahabir. "Averaged and sampled-data models for current mode control: a reexamination," *IEEE PESC*, 1989.

[25] G.C. Verghese and S.R. Sanders. "Observers for flux estimation in induction machines," *IEEE Trans. on Industrial Electronics*, 1988.